Temperature Dependence of Gas Physisorption Energy: Experimental and Computational Studies of Krypton on Porous Carbon

Thesis by

Ziyi Wang

In Partial Fulfillment of the Requirements for the
Degree of
Doctor of Philosophy

CALIFORNIA INSTITUTE OF TECHNOLOGY
Pasadena, California

2023
Defended April 3, 2023

ACKNOWLEDGEMENTS

I want to express my deepest appreciation to my advisor, Prof. Brent Fultz, for his unwavering support, guidance, and invaluable feedback throughout my PhD journey. His extensive reviews and cutting-edge ideas, coupled with his encouragement for me to think critically and independently, have been instrumental in shaping my research and personal growth.

I am immensely grateful to the other members of my thesis committee for their invaluable contributions. Prof. William Andrew Goddard's warm welcome to Caltech during my prospective student visit set the tone for my PhD academic experience. Prof. Zhen-Gang Wang's thermodynamics and thermostatistics courses provided me with valuable knowledge and a solid background in these fields, while Prof. Nicholas P. Stadie's pioneering work on physical adsorption has been a precious resource.

I would also like to express my gratitude to my candidacy exam committee members: Prof. Katherine Faber for her administrative support, Prof. Keith Schwab for his outstanding introduction to solid-state physics, and Prof. Marco Bernardi for introducing me to the ideas of density functional theories.

This work also relies on collaborations with many individuals. Cullen Quine, an expert in the field, introduced me to the adsorption experiment. Dr. Claire N. Saunders and Camille Bernal-Choban warmly helped me in various fields, particularly in computational studies. Dr. Channing Ahn, an encyclopedia of experiments, also provided valuable insights.

I would also like to thank Dr. David Boyd, Vladimir Ladygin, and Joel Chacko for consistently bringing me new ideas. Dr. Shen Yang, Stefan Lohaus, Pedro Guzman, and Elizabeth Zhou have created a friendly and supportive environment in our group, which has been critical to me.

I want to express my appreciation to my family and friends for their constant encouragement throughout these years, particularly my parents: Mr. Daqing Wang and Mrs. Haoyun Yin, for their rock-solid support. Without them, I would not have been able to overcome obstacles and challenges.

Finally, I am grateful to Caltech, especially the Department of Applied Physics and Materials Science, for providing me with a peaceful studying environment and

numerous opportunities for my future. I am honored to have been a part of this community and will cherish these experiences for the rest of my life.

ABSTRACT

This thesis investigates the temperature dependence of physical adsorption or physisorption energy using theoretical, computational, and experimental approaches.

Chapter 1 provides an overview of the van der Waals potential as the driving energy for physical adsorption and reviews various methods for calculating this potential, from the Lennard-Jones potential to recent DFT algorithms.

Chapter 2 reviews the thermodynamics of physical adsorption and emphasizes the importance of considering the motions of adsorbed gas molecules, which are determined by the potentials. Henry's law and variants of the Langmuir model are derived based on different potentials, and different forms of adsorption energy are presented.

Chapter 3 focuses on experiments and reports a significant weakening of the adsorption energy by 13% and 15% for two different materials with the temperature increase, as obtained from adsorption isotherms collected for krypton adsorption on active carbon materials over a temperature range of 250 K to 330 K and analyzed using Henry's law.

Chapter 4 is the central part of the work, where density functional theory calculations with the many-body dispersion energy method are used to calculate the adsorption potentials and derive corresponding adsorption energies for different sizes of pores. The study demonstrates that the structures of the pores significantly influence the surface dynamics and the internal energies of the adsorbates at different temperatures. Gas molecules adsorbed in pores of different sizes have different heat capacities larger than the gas phase. The computations use the slit-pore model with the 2-dimensional ideal gas assumption in the classical limit, and comparisons are made with quantum analysis, non-ideal slit-pore model, and slit-pores with multiple layers in the latter three subsections of the second section. The third section simulates the thermal displacements of the adsorbent at different temperatures with the stochastic Temperature Dependent Effective Potential method and reveals that thermal displacement has a small impact on the van der Waals potential but cannot change the adsorption energy.

Chapter 5 combines the experimental and computational results and shows 5% and 15% of adsorption energy weakening for two different materials. The reasons for this temperature dependence are proposed, including the larger heat capacities in the adsorbed phase mentioned in Chapter 3 and the fact that pores with higher energies become more accessible at high temperatures due to Boltzmann statistics, which weakens the statistically averaged internal energy. Other possible reasons are also discussed, and further research projects are proposed.

TABLE OF CONTENTS

LIST OF ILLUSTRATIONS

LIST OF TABLES

NOMENCLATURE

Δh.	phase change enthalpy per molecule	eV
Δh_{st}.	isosteric adsorption enthalpy per molecule	eV
Δu.	phase change energy per molecule	eV
Δu_{st}.	isosteric adsorption energy per molecule	eV
ϵ_{DFT}.	DFT system energy	eV
ϵ_{t}.	DFT system energy with van der Waals potential	eV
γ.	prefactor	Pa^{-1}
Λ.	thermal de broglie wavelength	$\mathrm{Å}^{-1}$
μ.	chemical potential per molecule	eV
μ_{ads}.	chemical potential per molecule of adsorbed phase	eV
μ_{gas}.	chemical potential per molecule of gas phase	eV
ω.	angular frequency	$\mathrm{rad}\cdot\mathrm{s}^{-1}$
$\Omega(\rho_D)$.	NLDFT grand canonical partition function	$\mathrm{Å}^{-3}$
$\phi(\vec{r})$.	DFT wave function	$\mathrm{Å}^{-1.5}$
$\rho(\vec{r})$.	DFT electron density	$e\cdot\mathrm{Å}^{-3}$
ρ_D.	NLDFT density of adsorbed molecule	$\mathrm{Å}^{-3}$
σ.	distance constant in Lennard-Jones potential	Å
θ.	rate of coverage	-
ε_{00}.	bottom energy of van der Waals potential wells	eV
ε_0.	energy constant in Lennard-Jones potential	eV
$\varepsilon_{\mathrm{LJ}}$.	Lennard-Jones potential	eV
$\varepsilon_{\mathrm{vdW}}$.	van der Waals potential energy	eV
ε_z.	van der Waals potential energy perpendicular to the surface	eV
A.	size of surface	$\mathrm{Å}^2$
c_{ads}.	heat capacity of adsorbed phase	$\mathrm{eV}\cdot\mathrm{K}^{-1}$

c_{QHO}.	heat capacity of quantum harmonic oscillator	$\text{eV}\cdot\text{K}^{-1}$
c_z.	heat capacity perpendicular to the surface	$\text{eV}\cdot\text{K}^{-1}$
D.	distance between two slit-pore surfaces	Å
D_{b}.	distance between bulk layers in slit-pore model	Å
F.	Helmholtz free energy of adsorbed phase	eV
$f(\varepsilon_{\text{vdW}})$.	distribution function of van der Waals potential energy	eV^{-1}
H.	Hamiltonian	eV
h.	enthalpy per molecule	eV
h_{ads}.	enthalpy per molecule in adsorbed phase	eV
h_{gas}.	enthalpy per molecule in gas phase	eV
k_{B}.	Boltzmann constant	$\text{eV}\cdot\text{K}^{-1}$
k_{e}.	electric charge	$\text{eV}\cdot\text{Å}\cdot e^{-2}$
K_{H}.	Henry's constant	Pa^{-1}
K_{L}.	Langmuir constant	Pa^{-1}
m.	mass	kg
N.	number of Langmuir sites for adsorption	-
n.	number of adsorbed molecules	-
P.	pressure	Pa
p.	momentum	$\text{kg}\cdot\text{m}\cdot\text{s}^{-1}$
Q.	canonical particle partition function of adsorbed phase	-
q_{ads}.	single particle partition function of adsorbed phase	-
q_{DF}.	single particle partition function of delta function potential	-
q_{e}.	electric charge	e
q_{QF}.	single particle partition function of quadratic potential	-
q_{QHO}.	partition function of quantum harmonic oscillator	-
q_{SP}.	single particle partition function of square potential	-
q_z.	single particle partition function perpendicular to the surface	-

R.	distance	Å
s.	entropy per molecule	$\mathrm{eV{\cdot}K^{-1}}$
T.	temperature	K
$T[n(\vec{r})]$.	DFT kinetic energy functional	eV
u.	internal energy per molecule	eV
$U[n(\vec{r})]$.	DFT electron–electron interaction energy functional	eV
u_{ads}.	internal energy per molecule in adsorbed phase	eV
u_{gas}.	internal energy per molecule in gas phase	eV
u_{QHO}.	internal energy of quantum harmonic oscillator	eV
u_z.	internal energy perpendicular to the surface	eV
v.	volume per molecule	eV
$V(\vec{r})$.	DFT potential energy	eV
$V_{\mathrm{ext}}(\vec{r})$.	NLDFT external potential energy	eV
$V_{\mathrm{s}}(\vec{r})$.	DFT Kohn-Sham potential energy	eV

Chapter 1

ENERGY OF PHYSICAL ADSORPTION

Physical adsorption, also known as physisorption, occurs when a fluid comes into contact with a surface. The fluid that adheres to the surface is called the adsorbate, while the surface substrate is called the adsorbent. Unlike absorption, the adsorbate does not penetrate the adsorbent. Instead, the adsorbate generates a thin layer on the surface of the adsorbent, referred to as the adsorbed phase (Nicholson and Parsonage, 1982; Toth, 2002; Ruthven, 2006).

Physisorption is used widely in our daily lives. With physisorption, activated carbons in air purifiers can separate odorous chemicals. Physisorption is also critical in the industry. Heterogeneous catalysis is an example. In the Haber–Bosch process, nitrogen (N_2) and hydrogen (H_2) are physically adsorbed on the catalyst and react to form ammonia (NH_3) (Haber and Le Rossignol, 1913). There are many new developing fields using physisorption principles, including gas storage (Chen et al., 1997; Menon and Komarneni, 1998; Poirier, Chahine, and Bose, 2001; Panella, Hirscher, and Roth, 2005; Jorda-Beneyto et al., 2007) and energy storage (Lefebvre and Tezel, 2017).

As its name implies, physisorption is primarily driven by physical interactions, such as van der Waals forces, hydrogen bonding, and electrostatic interactions, without forming chemical bonds. Among the physical forces, one of the most significant interactions for physisorption is the van der Waals (vdW) interaction, named after the Dutch physicist Johannes Diderik van der Waals.

1.1 vdW Force

The origin of the vdW force is illustrated in Fig. 1.1. Starting from Fig. 1.1(a), the left part shows two non-polarized particles without vdW interaction. Assume these two particles are two single-atom molecules, and the red parts are nuclei while the blue parts are electron clouds. When these two molecules are put together, according to the Born–Oppenheimer approximation, their nuclei positions are almost fixed while their electron clouds quickly reach a new equilibrium position. To minimize the potential energy, the electron clouds will move further from each other, creating two "instantaneous induced dipoles." In this case, the vdW interaction is the interaction

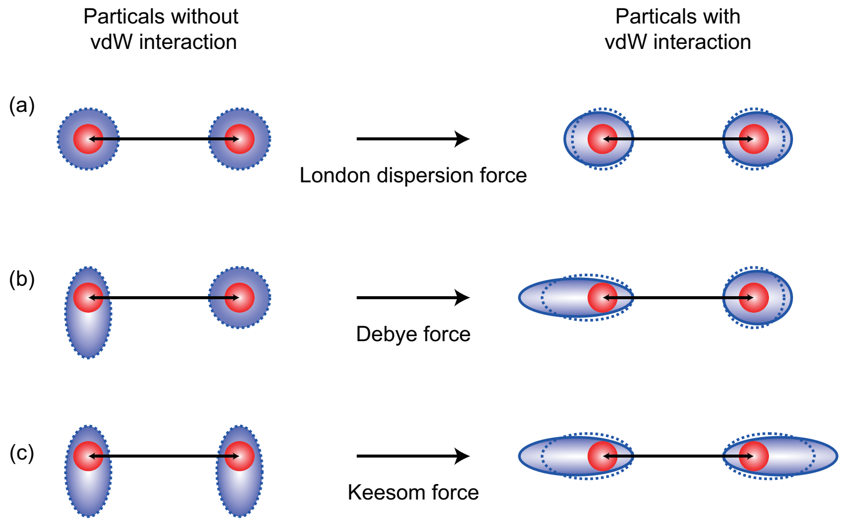

Figure 1.1: Illustration of the vdW interaction on different types of molecules. The red parts represent the positive charges, mostly given by the nuclei of the atoms. The blue parts represent the negative charges, mostly given by the electrons of the atoms. On the left are the particles without vdW interactions, and on the right are the particles under vdW interactions. The dashed blue lines are the positions of negative electrons without vdW forces, and the solid blue lines are with vdW forces. (a) London dispersion force: the vdW interaction between non-polarized particles (London, 1937; Leite et al., 2012). (b) Debye force: the vdW interaction between non-polarized and polarized particles (Leite et al., 2012). (c) Keesom force: the vdW interaction between polarized particles (Keesom, 1915; Leite et al., 2012)

.

between these two induced dipoles, named the "London dispersion force." Fig. 1.1(b) and (c), show the molecules with initial polarizations. These dipoles change both the orientations and the magnitudes (Kittel, 2004; Leite et al., 2012).

1.2 LJ Expression of vdW Potential

In 1924, John Lennard-Jones proposed a potential to characterize the London dispersion interaction, which was later called the "Lennard-Jones (LJ) potential":

$$\varepsilon_{\mathrm{LJ}}(R) = -4\varepsilon_0 \left[\left(\frac{\sigma}{R}\right)^{12} - \left(\frac{\sigma}{R}\right)^{6} \right], \tag{1.1}$$

where R is the distance between the adsorbent and adsorbate. ε_0 is a negative constant describing the magnitude of the potential. σ is a constant with the unit of distance. When $R < \sigma$, the repulsive potential dominates, and when $R > \sigma$, this potential turns attractive. This energy reaches extrema ε_0 when $R = 2^{1/6} \cdot \sigma$ (Lennard-Jones, 1931; Kittel, 2004).

In Eq. (1.1), the $-4\varepsilon_0\sigma^6/R^6$ part shows the dipole-dipole interaction. Meanwhile, the $-4\varepsilon_0\sigma^{12}/R^{12}$ part represents the repulsion by Pauli exclusion theory. although different forms of repulsion potentials are also proposed, Eq. (1.1) is precise enough to describe the interaction between inert gas molecules.

Although LJ potential is an empirical-based model, the $-4\varepsilon_0\sigma^6/R^6$ term can be given by simple analysis with the harmonic oscillator model, shown below and in Fig. (1.2).

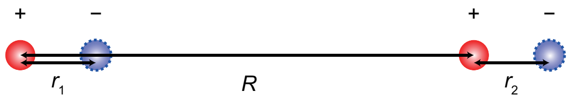

Figure 1.2: Illustration of the interaction between two harmonic oscillators. The red parts are positive charges, and the blue parts are negative charges. R is the distance between the positive charges, which is fixed according to the Born–Oppenheimer approximation. r_1 and r_2 are the distance between the positive and negative charges. R is much larger than r_1 and r_2.

Assuming the electron cloud in the atom behaves like a harmonic oscillator around the nucleus, and the frequency is ω. The initial Hamiltonian without the vdW force is given by:

$$H_0 = \frac{p_1^2}{2m} + \frac{m\omega^2 r_1^2}{2} + \frac{p_2^2}{2m} + \frac{m\omega^2 r_2^2}{2}. \tag{1.2}$$

With the Coulombic potential, the additional inter-molecule Hamiltonian is:

$$H_1 = \frac{k_\mathrm{e} q_\mathrm{e}^2}{R} + \frac{k_\mathrm{e} q_\mathrm{e}^2}{R - r_1 + r_2} - \frac{k_\mathrm{e} q_\mathrm{e}^2}{R - r_1} - \frac{k_\mathrm{e} q_\mathrm{e}^2}{R + r_2}, \tag{1.3}$$

where q_e is the quantity of electric charge and k_e is the Coulomb constant. By doing a second-order Taylor expansion on Eq. 1.3, it becomes:

$$H_1 = -\frac{2k_\mathrm{e} q_\mathrm{e}^2 r_1 r_2}{R^3}. \tag{1.4}$$

By defining:

$$r_{\mathrm{s}} \equiv \frac{r_1 + r_2}{\sqrt{2}},\ r_{\mathrm{a}} \equiv \frac{r_1 - r_2}{\sqrt{2}}; \tag{1.5}$$

and

$$p_{\mathrm{s}} \equiv \frac{p_1 + p_2}{\sqrt{2}},\ p_{\mathrm{a}} \equiv \frac{p_1 - p_2}{\sqrt{2}}; \tag{1.6}$$

where the subscript s means symmetric while a means anti-symmetric. Taking H_0 and H_1 together, the total Hamiltonian H_t is:

$$H_{\mathrm{t}} = \left[\frac{p_s^2}{2m} + \frac{mr_{\mathrm{s}}^2}{2}\left(\omega^2 - \frac{2k_{\mathrm{e}}q_{\mathrm{e}}^2}{mR^3}\right)\right] + \left[\frac{p_a^2}{2m} + \frac{mr_{\mathrm{a}}^2}{2}\left(\omega^2 + \frac{2k_{\mathrm{e}}q_{\mathrm{e}}^2}{mR^3}\right)\right]. \tag{1.7}$$

Eq. (1.7) shows the Hamiltonian of two harmonic oscillators with the frequency of $\omega_{\mathrm{s}} = (\omega^2 - 2k_{\mathrm{e}}q_{\mathrm{e}}^2/mR^3)^{1/2}$ and $\omega_{\mathrm{a}} = (\omega^2 + 2k_{\mathrm{e}}q_{\mathrm{e}}^2/mR^3)^{1/2}$. The ground state energy is then: $1/2\,\hbar(\omega_{\mathrm{a}} + \omega_{\mathrm{s}})$. Compared with the initial harmonic oscillators without Coulombic interaction with a ground state energy of $2 \cdot 1/2\,\hbar\omega = \hbar\omega$, the difference in energy is $k_{\mathrm{e}}^2 q_{\mathrm{e}}^4/\,2m^2R^6$, which is in proportion to $1/\,R^6$ (Kittel, 2004).

1.3 DFT Algorithms for vdW Potential

Density functional theory (DFT) is a popular method for calculating the energies of electrons and nuclei. Before DFT, the Hartree–Fock (HF) method was used for solving the Schrödinger equation and getting the energy. The system wave function was a Slater determinant containing the wave functions of all electrons. Assuming the system contains N electrons, the HF method has to solve N independent wave functions, which is difficult for complex systems (D. R. Hartree and W. Hartree, 1935; Echenique and Alonso, 2007; Sholl and Steckel, 2009).

DFT emerged after Pierre Hohenberg and Walter Kohn proved the Hohenberg-Kohn theorems in 1964. They proved that the properties of a system in its ground state, including the system wave function, could be determined from only the density of electrons (Hohenberg and Kohn, 1964; Gilbert, 1975). Based on this, the DFT method only needs to solve the density of the electrons rather than to solve the individual electron wave functions, which significantly reduces the complexity of analyzing many-electron systems.

With the density functional and the Schrödinger equation, the system energy turns into:

$$\epsilon_{\mathrm{DFT}}[\rho(\vec{r})] = T[\rho(\vec{r})] + U[\rho(\vec{r})] + \int V(\vec{r})\rho(\vec{r})d\vec{r^3}. \tag{1.8}$$

where ϵ_{DFT} is the energy of the system, T is the kinetic energy, U is the electron–electron interaction energy and V is the potential energy. ρ is the electron density and r is the spatial vector.

To solve Eq. (1.8), Walter Kohn and Lu Jeu Sham proposed a method in 1965 (Kohn and Sham, 1965; Sholl and Steckel, 2009). They regard the electron-electron interaction as part of the potential, so the total potential is given by:

$$V_{\text{s}}(\vec{r}) = V(\vec{r}) + U(\vec{r}), \tag{1.9}$$

and the Schrödinger equation becomes:

$$\left[-\frac{\hbar^2}{2m}\nabla^2 + V_{\text{s}}(\vec{r})\right]\phi(\vec{r}) = \epsilon_{\text{DFT}}\phi(\vec{r}). \tag{1.10}$$

This equation is known as the Kohn–Sham equation. In practice, an initial guess for $\rho(\vec{r})$ is used for the $U(\vec{r})$ in Eq. (1.9). Taking that into Eq. (1.10), the system wave function $\phi(\vec{r})$ can be solved. This wave function $\phi(\vec{r})$ is used for generating electron density $\rho(\vec{r})$ for the next iteration. With the new $\rho(\vec{r})$ and Eq. (1.10), a new $\phi(\vec{r})$ is achieved. By repeating this process for multiple iterations, the $\phi(\vec{r})$ and ϵ should converge.

DFT is good for analyzing system energies. However, it becomes less accurate when it comes to the vdW interaction. An intuitive idea would be that the vdW energy is too small, and the algorithm cannot distinguish this energy with possible error. However, there are other more important reasons. First, standard DFT functionals focus on short-range interactions, where the electron clouds of two atoms overlap. Second, DFT only gives a time-averaged electron density, and the time-dependent waves of each electron are unclear. Reviewing the derivation of the R^{-6} potential in the last section, the Coulombic potential impacts harmonic oscillators, and two different vibrational modes emerge. The correlation between the two harmonic oscillators is time-dependent, and the electron clouds do not overlap. Therefore, standard DFT functionals can not unveil these long-range correlated two modes (Klimes and Michaelides, 2012; Stohr, Voorhis, and Tkatchenko, 2019).

In principle, analyzing the individual electron wave functions with the HF method can give the vdW interaction accurately. Methods like the coupled cluster (CC) follow this track. The results given by CCSD(T), a certain type of CC method, are usually used as the benchmarks for computation (Stohr, Voorhis, and Tkatchenko, 2019). However, these methods are resource-consuming, and therefore, corrections for DFT are needed. Here, three different types of corrections will be discussed.

1.3.1 DFT-D and DFT-D2

The simplest idea of correction is adding the R^{-6} potential on the total DFT energy:

$$\epsilon_{\mathrm{t}} = \epsilon_{\mathrm{DFT}} + \sum_{i,j,i\neq j} C_{ij}/R_{ij}^{6}, \tag{1.11}$$

where i and j are the indexes of the atoms. $C_{ij} = \sqrt{C_{ii} \cdot C_{jj}}$ is the potential constant, where C_{ii} and C_{jj} are the constant of the same species. R_{ij} is the distance between the i^{th} and j^{th} atom.

As the initial attempt of adding vdW potential, DFT-D is cheap in computational cost but obviously inaccurate. Compared with the LJ potential, DFT-D ignores the Pauli exclusion repulsion and is only suitable for very long-range interactions. To improve accuracy in the short-range interaction, Stefan Grimme developed the DFT-D2 algorithm in 2006 (Grimme, 2006). Compared with DFT-D, DFT-D2 adds a damping function to the correction:

$$\epsilon_{\mathrm{t}} = \epsilon_{\mathrm{DFT}} + \sum_{i,j,i\neq j} f_6(i,j,R_{ij}) \cdot C_{ij}/R_{ij}^{6}, \tag{1.12}$$

and the damping function is:

$$f_6(i,j,R_{ij}) = \frac{s_6}{1 + \exp\left[-d \cdot \left(R_{ij} \,/\, s_R \cdot \sigma_{ij} - 1\right)\right]}, \tag{1.13}$$

where s_6 is a global scaling factor determined by the DFT functional. s_R is the scaling factor usually set as 1. d is the damping factor, usually set as 20. $\sigma_{ij} = 0.5\,(\sigma_{ii} + \sigma_{jj})$ is the constant similar to the σ in Eq. (1.1). This damping function has the following features. When R_{ij} is small and close to 0, the damping function is $s_6/[1 + \exp(d)] \approx 0$. When $R_{ij} = s_R \cdot \sigma_{ij}$, the damping function is $s_6/2$. When R_{ij} is large, the damping function is s_6.

1.3.2 DFT-D3 and Tkachenco-Scheffler (TS)

With the damping function, the DFT-D2 method successfully generates the LJ-like potential. However, the upcoming problem is that the factors in DFT-D2 only depend on the type of the atoms but not their environments. For example, the carbon atoms in methane, ethylene, acetylene, and benzene have the same factors. However, that is physically not true, as their electrons are in completely different orbits. To get more precise results, algorithms at the next level are developed.

Grimme et al. improved the DFT-D2 to DFT-D3 in 2010 (Grimme et al., 2010; Grimme, 2011). Compared with DFT-D2, DFT-D3 adds an extra R^{-8} potential and corresponding damping function. This potential arises from higher order Taylor expansion in Eq. (1.3) and Eq. (1.4). More importantly, the C_{ij} in Eq. (1.12) is adjusted according to the coordinates of the atoms. Atoms are squeezed by their nearby neighbors, and the electrons are less polarizable. The vdW potentials are then smaller.

Meanwhile, Alexandre Tkatchenko and Matthias Scheffler developed another improved algorithm, the Tkatchenko-Scheffler (TS) method (Tkatchenko and Scheffler, 2009). The form of the TS potential is the same as Eq. (1.12). However, The combination rules of C_{ij} and R_{ij} are no longer quadratic and arithmetic mean values of the single-type molecule parameters. They modified the combination rules by considering the electron density near the atoms calculated by DFT.

1.3.3 Many-Body Dispersion (MBD)

Beyond the environmental-dependent vdW potential, the many-body interactions become important, as the corrections mentioned before consider only pair-by-pair interactions. The difference between the pairwise and many-body interactions is clearly shown in Fig. (1.3) adopted from Tkatchenko and co-workers' paper. Without the many-body effects, the interaction between the A and B atoms can not feel the electron from the C atom. However, as Fig. (1.3) shows, this assumption cannot show the coupling interaction among the three atoms, for example, the out-of-plane fluctuation.

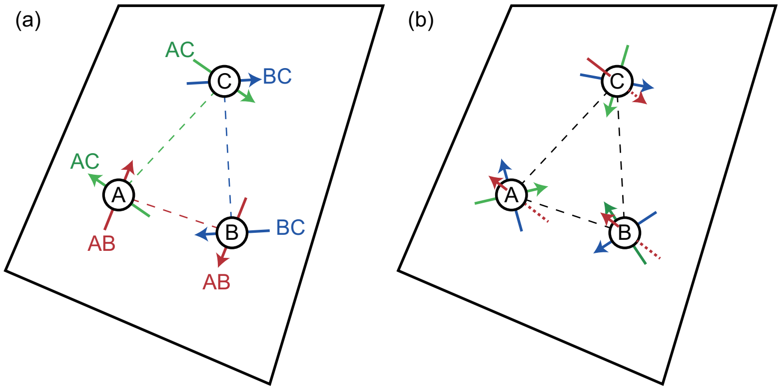

Figure 1.3: Illustration of the difference between the pairwise and the many-atom vdW interaction. The three spheres are inert gas molecules. The arrows are the alignment of fluctuating, instantaneous dipoles, which show the "eigenmodes" of the electron density fluctuations. The red arrows in (b) are perpendicular to the plane. Figure inspired by the citation (Stohr, Voorhis, and Tkatchenko, 2019).

To include the many-body effects, Tkatchenko and co-workers developed the Many-Body Dispersion (MBD) algorithm (Tkatchenko, Distasio, et al., 2012; Ambrosetti et al., 2014). It starts from the adiabatic-connection fluctuation-dissipation (ACFD) theorem, analyzing the Coulomb-coupled system energy. Then it uses the random phase approximation (RPA) to simplify the expression for the energy. For the atoms, the coupled fluctuating dipole model (CFDM) is employed, and the atoms are regarded as three-dimensional (3D) quantum harmonic oscillators (QHOs). The MBD algorithm shows a better correspondence with the Benchmark data (Gould et al., 2016; Kim et al., 2016; Stohr, Voorhis, and Tkatchenko, 2019).

Chapter 2

THERMODYNAMIC ANALYSIS OF PHYSISORPTION

The previous chapter described the origin of the physisorption on the molecular scale. However, physisorption is generally observed on a much larger scale. For working with experimental investigations, thermodynamic analysis of physisorption is important. This section summarizes several well-established thermodynamic theories that explore the relationship between adsorption energy and the vdW potential energy.

2.1 Clausius-Clapeyron Equation

The Clapeyron equation is one of the most important equations in phase change (Sandler, 2017). It derives the enthalpy of phase change with the following equation:

$$\frac{\Delta h}{T \cdot \Delta v} = \frac{h_\alpha - h_\beta}{T \cdot (v_\alpha - v_\beta)} = \left(\frac{\partial P}{\partial T}\right)_n, \tag{2.1}$$

where h is the enthalpy and v is the volume. P and T are pressure and temperature. n represents the number of molecules already changed from the α phase to the β phase. The derivation of this equation is not complicated. In the phase change process, the chemical potentials of different phases are equivalent:

$$\mu_\alpha = \mu_\beta. \tag{2.2}$$

In the $P - T - \mu$ space, the condition in Eq. (2.2) corresponds to a surface called the binodal surface or the coexistence surface. On this surface,

$$\mathrm{d}\mu_\alpha = \mathrm{d}\mu_\beta. \tag{2.3}$$

Taking the Gibbs-Duhem equation:

$$\mathrm{d}\mu = -s\mathrm{d}T + v\mathrm{d}P \tag{2.4}$$

into Eq. (2.3), it becomes:

$$(s_\alpha - s_\beta)\,\mathrm{d}T = (v_\alpha - v_\beta)\,\mathrm{d}P \tag{2.5}$$

which is equivalent to:

$$\frac{(s_\alpha - s_\beta)}{(v_\alpha - v_\beta)} = \frac{\mathrm{d}P}{\mathrm{d}T}. \tag{2.6}$$

At a phase transition, the difference between the Gibbs free energy of the two phases is zero. That means:

$$0 = g_\alpha - g_\beta = (h_\alpha - h_\beta) - T\,(s_\alpha - s_\beta). \tag{2.7}$$

Taking Eq. (2.7) in Eq. (2.6), the Clapeyron equation shown in Eq. (2.1) is derived. The Clapeyron equation gives the enthalpy for phase change by several parameters, including temperature, pressure, and volume, and these parameters are observable in experiments. For the phase transition between the gas and a condensed phase, the adsorbed phase, for example, the volume is considered very small compared with the gas phase. By implementing the ideal gas condition, Eq. (2.1) turns into:

$$\Delta h_{\mathrm{st}} = h_{\mathrm{ads}} - h_{\mathrm{gas}} = -\frac{k_{\mathrm{B}}T^2}{P}\left(\frac{\partial P}{\partial T}\right)_n, \tag{2.8}$$

which is a form of the Clausius-Clapeyron equation. Here, h_{st} is the isosteric enthalpy of adsorption of one molecule, and isosteric means the same amount of adsorption (Huang, 1972; Shen et al., 2000; Farrusseng et al., 2009; Helmy, Ferreiro, and Bussetti, 1996; Son et al., 2018; Yu et al., 2021). For the ideal gas, its internal energy is:

$$u_{\mathrm{gas}} = h_{\mathrm{gas}} - Pv_{\mathrm{gas}} = h_{\mathrm{gas}} - k_{\mathrm{B}}T. \tag{2.9}$$

Assuming the volume is negligible for the adsorbed phase, its internal energy equals its enthalpy. Taking these in Eq. (2.8), the isosteric energy is given by:

$$\Delta u_{\mathrm{st}} = u_{\mathrm{ads}} - u_{\mathrm{gas}} = -\frac{k_{\mathrm{B}}T^2}{P}\left(\frac{\partial P}{\partial T}\right)_n + k_{\mathrm{B}}T. \tag{2.10}$$

Note that both Δu_{st} and Δh_{st} are negative values. Because of the $k_{\mathrm{B}}T$ term in Eq. (2.10), the magnitude of Δu_{st} is smaller than Δh_{st}.

2.2 Henry's Law

The previous section described fixed adsorption amount cases, also called isosteric cases. However, the isosteric condition is not easy to maintain in experiments, while the isothermal condition is used more often. The amount of adsorption versus pressure at the same temperature is named the "isotherm", and Henry's law is the most straightforward method to fit the isotherms:

$$n = K_{\mathrm{H}} \cdot P, \tag{2.11}$$

where K_H is Henry's constant, which changes with the temperature $K_\mathrm{H}(T)$ (Hill, 1994; Sandler, 2017). In this thesis, n is the number of molecules.

Henry's law was proposed by William Henry over two hundred years ago. The limitation of Henry's law is that it is only valid for low-pressure and small amounts of adsorption. However, it is still a good method to evaluate the isosteric adsorption energy. For the same adsorption amount, taking this relationship in Eq. (2.10), the isosteric energy is:

$$\Delta u_\mathrm{st} = u_\mathrm{ads} - u_\mathrm{gas} = \frac{k_\mathrm{B}T^2}{K_\mathrm{H}} \left(\frac{\partial K_\mathrm{H}}{\partial T}\right)_n + k_\mathrm{B}T. \tag{2.12}$$

2.3 Langmuir Model

In 1916, Irving Langmuir proposed the following law of adsorption, named the Langmuir adsorption model:

$$\theta = \frac{n}{N} = \frac{K_\mathrm{L} \cdot P}{1 + K_\mathrm{L} \cdot P}, \tag{2.13}$$

where N is the total number of sites allowed for adsorption, and θ is the fraction of coverage. K_L is a constant. This Langmuir model describes the single layer of adsorption, and it turns into Henry's law at low pressure or low coverage (Langmuir, 1916).

The statistical-mechanical derivation of the Langmuir model starts from the two-state model (Hill, 1994; Swenson and Stadie, 2019). For the N sites, there are the occupied and vacancy states. Each occupied site acquires an additional energy of ε. Here, ε is a negative value generally considered constant with temperature.

The canonical partition function of the system, Q, contains two parts. First is the configurational entropy of picking n adsorbed sites from N sites. Second is the partition function of the single particle, corresponding to the energy of the adsorbed phase. Therefore, it goes by:

$$Q(n, N, T) = \frac{N!}{n!(N-n)!} q_\mathrm{ads}^n = \frac{N!}{n!(N-n)!} \exp(-\frac{n\epsilon}{k_\mathrm{B}T}). \tag{2.14}$$

Here, q_ads is the partition function of a single adsorbed molecule. N is similar to the V in the classical $n - V - T$ ensemble. The Helmholtz free energy is then given by:

$$\begin{aligned} F = U_\mathrm{ads} - TS_\mathrm{ads} = -k_\mathrm{B}T \ln Q = n\epsilon - k_\mathrm{B}T \ln \frac{N!}{n!(N-n)!}, \\ \approx n\epsilon - k_\mathrm{B}T[N \ln N - (N-n)\ln(N-n) - n \ln n], \end{aligned} \tag{2.15}$$

where Stirling's approximation $\ln n! \approx n \ln n - n$ is used. The chemical potential of the adsorbed phase is then:

$$\mu_{\mathrm{ads}} = \left(\frac{\partial F}{\partial n}\right)_{N,T} = \epsilon + k_{\mathrm{B}} T \ln \frac{n}{N-n}. \tag{2.16}$$

Meanwhile, the ideal gas chemical potential is:

$$\mu_{\mathrm{gas}} = k_{\mathrm{B}} T \ln \frac{P\Lambda^3}{k_{\mathrm{B}} T}, \tag{2.17}$$

where Λ is the thermal de Broglie wavelength:

$$\Lambda \equiv \sqrt{\frac{2\pi\hbar^2}{m k_{\mathrm{B}} T}}, \tag{2.18}$$

where m is the mass of the adsorbed molecule (Hill, 1994). During the adsorption, the two chemical potentials should be equal:

$$\mu_{\mathrm{ads}} = \mu_{\mathrm{gas}}. \tag{2.19}$$

Taking Eq (2.16) and Eq (2.17) in Eq (2.19), the Langmuir model is:

$$\theta = \frac{n}{N} = \frac{P\Lambda^3 \exp(-\epsilon/k_{\mathrm{B}}T)/k_{\mathrm{B}}T}{1 + P\Lambda^3 \exp(-\epsilon/k_{\mathrm{B}}T)/k_{\mathrm{B}}T}. \tag{2.20}$$

Compared with Eq (2.13), with this derivation, $K_{\mathrm{L}} = \Lambda^3 \exp(-\epsilon/k_{\mathrm{B}}T)/k_{\mathrm{B}}T$. Here, K_{L} is in proportion to $T^{-5/2}$ if ϵ is temperature-independent.

Another equivalent derivation uses the grand canonical ensemble:

$$\begin{aligned} \Omega(\mu, N, T) &= \sum_{n=0}^{N} \frac{N!}{n!(N-n)!} q_{\mathrm{ads}}^{n} \exp(\frac{n\mu}{k_{\mathrm{B}}T}), \\ &= \sum_{n=0}^{N} \frac{N!}{n!(N-n)!} \exp(-\frac{n\epsilon}{k_{\mathrm{B}}T}) \exp(\frac{n\mu}{k_{\mathrm{B}}T}), \\ &= \left[1 + \exp\left(\frac{\mu-\epsilon}{k_{\mathrm{B}}T}\right)\right]^{N}. \end{aligned} \tag{2.21}$$

The expected number of adsorbed molecules is:

$$\langle n \rangle = \left[\frac{\partial \ln \Omega}{\partial(\mu/k_{\mathrm{B}}T)}\right]_{N,T} = \frac{N \exp[(\mu-\epsilon)/k_{\mathrm{B}}T]}{1 + \exp[(\mu-\epsilon)/k_{\mathrm{B}}T]}. \tag{2.22}$$

During the adsorption, the chemical potential μ equals the gas phase chemical potential shown in Eq. (2.17). Taking this condition in Eq. (2.22), Eq. (2.20) then follows.

Taking Eq. (2.13) in the Clausius-Clapeyron equation, Eq. (2.10), the isosteric energy is:

$$\Delta u_{\mathrm{st}} = u_{\mathrm{ads}} - u_{\mathrm{gas}} = \frac{k_{\mathrm{B}}T^2}{K_{\mathrm{L}}} \left(\frac{\partial K_{\mathrm{L}}}{\partial T} \right)_n + k_{\mathrm{B}}T, \tag{2.23}$$

which is similar to Eq. (2.12). Using the K_{L} derived in Eq. (2.20), Eq. (2.23) becomes:

$$\Delta u_{\mathrm{st}} = \epsilon - 2.5k_{\mathrm{B}}T + k_{\mathrm{B}}T = \epsilon - 1.5k_{\mathrm{B}}T. \tag{2.24}$$

2.4 Surface Dynamics

Although the Langmuir model fits the experimental results well for many studies, it has several limitations in thermodynamics. First, it ignores the interaction between adsorbate molecules. This issue can be addressed by working in the low coverage limit at low pressure. Second, compared with Henry's law, the Langmuir model Eq. (2.13) has two fitting parameters. When fitting a series of isotherms of the same type of material, a uniform N and several different K_{L} are required. However, the selection of the N and K_{L} can create uncertainty, as different groups of parameters can show similar small errors. Third, the statistical-mechanical derivation shown in the previous section completely ignores the dynamics of adsorbate molecules on the surface and simply uses an undefined ϵ as the energy. However, the adsorbed phase is generally regarded as a supercritical phase, and the dynamic is not neglectable (Nicholson and Parsonage, 1982; Hill, 1994; Sprowl, Campbell, and Arnadottir, 2016; Maiga and Gatica, 2018).

To make corrections to the surface dynamics of adsorbates, a good method is considering the single particle partition function. Here, to simplify the discussion, the adsorbed molecules are considered noble gases, which have no internal vibration or rotation. The single particle partition function of the ideal gas atom is then:

$$q_{\mathrm{ads}} = \sum \exp(-\epsilon_j / k_{\mathrm{B}}T), \tag{2.25}$$

where ϵ corresponds to the energy of all the possible quantum states and can be given by the Schrödinger equation:

$$\left[-\frac{\hbar^2}{2m}\nabla^2 + \varepsilon_{\mathrm{vdW}}(x, y, z) \right] \phi(x, y, z) = \epsilon\phi(x, y, z), \tag{2.26}$$

where m is the mass of gas molecule and ϕ is the wave function. The $\varepsilon_{\mathrm{vdW}}$ is the vdW potential in the 3D space. However, solving the 3D Schrödinger equation with an arbitrary potential is not a simple task. Considering the mass of gas is large, and quantum effects are not big for adsorption, the non-quantum classical limit can be applied. The total energy is the sum of kinetic energy and potential energy:

$$\epsilon = \varepsilon_{\mathrm{vdW}}(x, y, z) + \frac{p_x^2}{2m} + \frac{p_y^2}{2m} + \frac{p_z^2}{2m}, \tag{2.27}$$

where p_x, p_y, and p_z are the momentum in the x, y, and z directions. As the momentum has no correlation with the vdW potential, by changing the sum into the integral in the momentum space and the position space, the single particle partition function is:

$$\begin{aligned} q_{\mathrm{ads}} =& \frac{8\pi^3}{\hbar^3} \int \exp(-\frac{p_x^2}{2mk_{\mathrm{B}}T})\mathrm{d}p_x \cdot \int \exp(-\frac{p_y^2}{2mk_{\mathrm{B}}T})\mathrm{d}p_y \\ & \cdot \int \exp(-\frac{p_z^2}{2mk_{\mathrm{B}}T})\mathrm{d}p_z \cdot \iiint \exp\left(-\frac{\varepsilon_{\mathrm{vdW}}}{k_{\mathrm{B}}T}\right)\mathrm{d}x\mathrm{d}y\mathrm{d}z. \end{aligned} \tag{2.28}$$

By using the results of Gaussian integrals for the momentum integrals, Eq. (2.28) becomes:

$$q_{\mathrm{ads}} = \frac{1}{\Lambda^3} \iiint \exp\left(-\frac{\varepsilon_{\mathrm{vdW}}}{k_{\mathrm{B}}T}\right)\mathrm{d}x\mathrm{d}y\mathrm{d}z. \tag{2.29}$$

The quantum volume Λ^3 is defined as Eq. (2.18). For the $\varepsilon_{\mathrm{vdW}}$, if there is no correlation in the x, y and z directions, then $\varepsilon_{\mathrm{vdW}} = \varepsilon_{\mathrm{x}} + \varepsilon_{\mathrm{y}} + \varepsilon_{\mathrm{z}}$, and Eq. (2.29) can be rewritten in the following form:

$$q_{\mathrm{ads}} = q_x q_y q_z \exp(-\varepsilon_{00}/k_{\mathrm{B}}T), \tag{2.30}$$

where ε_{00} is the minimum of the vdW potential in 3D space. The ε_x, ε_y, and ε_z are single variable potentials determined only by the coordinates x, y, and z. q_x, q_y, and q_z are partition functions in different directions. For example, q_z is:

$$q_{\mathrm{z}} = \frac{1}{\Lambda} \int \exp\left(-\frac{\varepsilon_{\mathrm{z}} - \varepsilon_{00}}{k_{\mathrm{B}}T}\right)\mathrm{d}z. \tag{2.31}$$

With the expression of the single particle partition function determined, the next step is choosing a suitable 3D vdW potential and relating this potential to the isotherms. The statistical mechanical analysis of several isotherm fitting methods is discussed below.

2.4.1 Variants of Langmuir Model

As previously discussed, the initial statistical mechanical derivation of the Langmuir Model ignores the dynamics of the adsorbed phase. However, it is not impossible to add the dynamics and keep the form of the Langmuir model shown in Eq. (2.13) at the same time. Going back to the statistical mechanics of the Langmuir model in the previous section, a configurational entropy can be included:

$$S_{\mathrm{ads}} = \left(\frac{\partial F}{\partial T}\right)_{n,N} = k_{\mathrm{B}} \ln \frac{N!}{n!(N-n)!}, \tag{2.32}$$

which comes from the different methods of choosing n occupied sites from N sites (Hill, 1994). However, the premise of this configuration is that the adsorbed molecules and sites are all identical. That means although the adsorbed molecules are still moving, they are trapped in the sites, and the process of jumping between sites is ignored. Then to characterize these trapping sites, the next step is creating the potentials for Eq. (2.29). It is much easier to assume $\varepsilon_{\mathrm{vdW}}$ has no correlation in the x, y, and z directions, and the simplification in Eq. (2.31) can be implemented. Fig. 2.1 shows three elementary potentials to characterize the adsorbate molecule on a site.

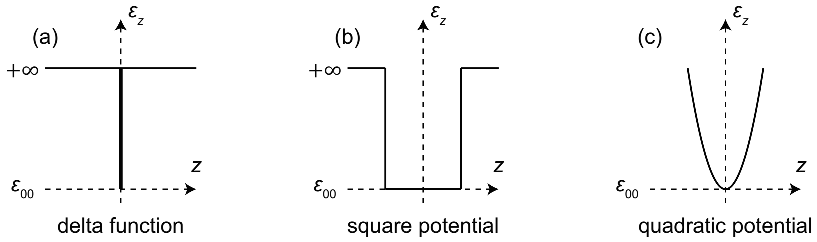

Figure 2.1: Illustration of three different 1D potentials to characterize the potential near the sites for adsorption. The origin of the axis is set at the position where the lowest potential energy ε_{00} lies.

In Fig. (2.1a), the delta function potential is infinitely large along most of the axis. The origin point is the only possible state where its energy equals ε_{00} and has no momentum. In this case, the classical limit shown from Eq. (2.27) to Eq. (2.29) is not applicable, and the partition function q_z is then:

$$q_{z\mathrm{DF}} = \exp\left(-\frac{\varepsilon_{00} - \varepsilon_{00}}{k_{\mathrm{B}}T}\right) = 1, \tag{2.33}$$

where "DF" means delta function.

In Fig. (2.1b), the square potential well is ε_{00} for the length between $-D_z/2$ to $D_z/2$, where D_z is the width of the potential well. The other part of the axis has an infinitely large potential. Taking this potential in Eq. (2.31), the partition function q_z is:

$$q_{z\mathrm{SP}} = \frac{1}{\Lambda}\int_{-D_z/2}^{D_z/2} \exp\left(-\frac{\varepsilon_{00}-\varepsilon_{00}}{k_\mathrm{B}T}\right)\mathrm{d}z = \frac{D_z}{\Lambda}, \tag{2.34}$$

where "SP" means square potential.

The quadratic potential has the following form:

$$\varepsilon_z = \varepsilon_{00} + \frac{1}{2}m\omega^2 z^2, \tag{2.35}$$

where ω is the angular frequency. Substituting into Eq. (2.31), the partition function q_z is:

$$q_{z\mathrm{QP}} = \frac{1}{\Lambda}\int_{-\infty}^{+\infty} \exp\left(-\frac{m\omega^2 z^2}{2k_\mathrm{B}T}\right)\mathrm{d}z = \frac{k_\mathrm{B}T}{\hbar\omega}, \tag{2.36}$$

where "QP" means quadratic potential.

The 3D partition function q_ads is the combination of the 1D partition functions according to Eq. (2.30). Then according to the similar steps shown in Eq (2.14) to Eq (2.16), the chemical potential of the adsorbed phase is:

$$\mu_\mathrm{ads} = \left(\frac{\partial F}{\partial n}\right)_{N,T} = -k_\mathrm{B}T\ln q_\mathrm{ads} + k_\mathrm{B}T\ln\frac{n}{N-n}. \tag{2.37}$$

Then according to Eq (2.17) and Eq (2.19), the generalized Langmuir model is:

$$\theta = \frac{n}{N} = \frac{P\Lambda^3 q_\mathrm{ads}/k_\mathrm{B}T}{1 + P\Lambda^3 q_\mathrm{ads}/k_\mathrm{B}T}. \tag{2.38}$$

and $K_\mathrm{L} = \Lambda^3 q_\mathrm{ads}/k_\mathrm{B}T$ for this Langmuir model. Substituting into Eq (2.23), the isosteric adsorption energy is then:

$$\Delta u_\mathrm{st} = \frac{k_\mathrm{B}T^2}{q_\mathrm{ads}}\cdot\frac{\partial q_\mathrm{ads}}{\partial T} - 2.5k_\mathrm{B}T + k_\mathrm{B}T = \frac{k_\mathrm{B}T^2}{q_\mathrm{ads}}\cdot\frac{\partial q_\mathrm{ads}}{\partial T} - 1.5k_\mathrm{B}T. \tag{2.39}$$

Considering the expression in Eq (2.30), the isosteric adsorption energy becomes:

$$\Delta u_\mathrm{st} = \frac{k_\mathrm{B}T^2}{q_x}\cdot\frac{\partial q_x}{\partial T} + \frac{k_\mathrm{B}T^2}{q_y}\cdot\frac{\partial q_y}{\partial T} + \frac{k_\mathrm{B}T^2}{q_z}\cdot\frac{\partial q_z}{\partial T} + \varepsilon_{00} - 1.5k_\mathrm{B}T. \tag{2.40}$$

For the three different partition functions corresponding to the potential shown in Fig. (2.1), the partial derivatives with the temperature are:

$$\frac{\partial q_\mathrm{DF}}{\partial T} = 0;\ \frac{\partial q_\mathrm{SP}}{\partial T} = \frac{q_\mathrm{SP}}{2T};\ \frac{\partial q_\mathrm{QP}}{\partial T} = \frac{q_\mathrm{QP}}{T}. \tag{2.41}$$

Assigning q_{DF}, q_{SP} and q_{QP} to q_x, q_y and q_z, 10 different combinations are shown in Table (2.1). Among all these combinations, several situations deserve further discussion.

The models with three potentials of the same type indicate symmetry along the three directions. However, the model with spherical symmetry might be a better choice to describe the symmetry along the x, y, and z axes. By using the spherical coordinate system, the gradient in the Schrödinger equation has a different form. In the classical limit, taking the spherical symmetry in Eq. (2.29), it turns into:

$$\begin{aligned} q_{\mathrm{ads}} &= \frac{1}{\Lambda^3} \iiint \exp\left(-\frac{\varepsilon_{\mathrm{vdW}}(r)}{k_{\mathrm{B}}T}\right) r^2 \mathrm{d}r\mathrm{d}\theta\mathrm{d}\varphi, \\ &= \frac{4\pi}{\Lambda^3} \int \exp\left(-\frac{\varepsilon_{\mathrm{vdW}}(r)}{k_{\mathrm{B}}T}\right) r^2 \mathrm{d}r. \end{aligned} \tag{2.42}$$

Table 2.1: The combination of partition functions of typical potentials. The K_{L} for the Langmuir model and the corresponding isosteric adsorption energy are both shown. The subscript 1, 2, and 3 can be any of x, y, and z. Meanwhile, D_x, D_y, and D_z are the lengths of the square potentials.

q_x, q_y, and q_z	K_{L}	Δu_{st}
3 q_{DF}	$\Lambda^3 \exp(-\varepsilon_{00}/k_{\mathrm{B}}T)/k_{\mathrm{B}}T$	$\varepsilon_{00} - 1.5k_{\mathrm{B}}T$
3 q_{SP}	$D_1D_2D_3 \exp(-\varepsilon_{00}/k_{\mathrm{B}}T)/k_{\mathrm{B}}T$	ε_{00}
3 q_{QP}	$\Lambda^3 k_{\mathrm{B}}^2T^2 \exp(-\varepsilon_{00}/k_{\mathrm{B}}T)/\hbar^3\omega^3$	$\varepsilon_{00} + 1.5k_{\mathrm{B}}T$
2 q_{DF} and 1 q_{SP}	$\Lambda^2 D_1 \exp(-\varepsilon_{00}/k_{\mathrm{B}}T)/k_{\mathrm{B}}T$	$\varepsilon_{00} - k_{\mathrm{B}}T$
2 q_{DF} and 1 q_{QP}	$\Lambda^3 \exp(-\varepsilon_{00}/k_{\mathrm{B}}T)/\hbar\omega$	$\varepsilon_{00} - 0.5k_{\mathrm{B}}T$
2 q_{SP} and 1 q_{DF}	$\Lambda D_1D_2 \exp(-\varepsilon_{00}/k_{\mathrm{B}}T)/k_{\mathrm{B}}T$	$\varepsilon_{00} - 0.5k_{\mathrm{B}}T$
2 q_{SP} and 1 q_{QP}	$\Lambda D_1D_2 \exp(-\varepsilon_{00}/k_{\mathrm{B}}T)/\hbar\omega$	$\varepsilon_{00} + 0.5k_{\mathrm{B}}T$
2 q_{QP} and 1 q_{DF}	$\Lambda^3 k_{\mathrm{B}}T \exp(-\varepsilon_{00}/k_{\mathrm{B}}T)/\hbar^2\omega^2$	$\varepsilon_{00} + 0.5k_{\mathrm{B}}T$
2 q_{QP} and 1 q_{SP}	$\Lambda^2 D_1 k_{\mathrm{B}}T \exp(-\varepsilon_{00}/k_{\mathrm{B}}T)/\hbar^2\omega^2$	$\varepsilon_{00} + 1k_{\mathrm{B}}T$
1 q_{DF}, 1 q_{SP} and 1 q_{QP}	$\Lambda^2 D_1 \exp(-\varepsilon_{00}/k_{\mathrm{B}}T)/\hbar\omega$	ε_{00}

For the square potential where $\varepsilon_{\mathrm{vdW}}(r) = \varepsilon_{00}$ when $r \leq R_0$ while $\varepsilon_{\mathrm{vdW}}(r) = +\infty$ when $r > R_0$, the single particle partition function is:

$$q_{\mathrm{ads}} = \frac{4\pi}{\Lambda^3} \exp\left(-\frac{\varepsilon_{00}}{k_{\mathrm{B}}T}\right) \int_0^{R_0} r^2 \mathrm{d}r = \frac{4\pi R_0^3}{3\Lambda^3} \exp\left(-\frac{\varepsilon_{00}}{k_{\mathrm{B}}T}\right). \tag{2.43}$$

With Eq. (2.38) and (2.39), the corresponding Langmuir constant K_{L} and adsorption energy Δu_{st} are: $4\pi R_0^3 \exp(-\varepsilon_{00}/k_{\mathrm{B}}T)/3k_{\mathrm{B}}T$ and ε_{00}. Compared with the Cartesian coordinate system results, it has a similar form, as R_0 and $D_1 D_2 D_3$ are both fitting parameters.

For the spherical quadratic potential where $\varepsilon_{\mathrm{vdW}}(r) = \varepsilon_{00} + 0.5m\omega^2 r^2$, the single particle partition function is:

$$q_{\mathrm{ads}} = \frac{4\pi}{\Lambda^3} \exp\left(-\frac{\varepsilon_{00}}{k_{\mathrm{B}}T}\right) \int_0^{+\infty} \exp\left(-\frac{m\omega^2 r^2}{2k_{\mathrm{B}}T}\right) r^2 \mathrm{d}r = \left(\frac{k_{\mathrm{B}}T}{\hbar\omega}\right)^3 \exp\left(-\frac{\varepsilon_{00}}{k_{\mathrm{B}}T}\right). \quad (2.44)$$

The corresponding K_{L} and Δu_{st} are: $\Lambda^3 k_{\mathrm{B}}^2 T^2 \exp(-\varepsilon_{00}/k_{\mathrm{B}}T)/\hbar^3\omega^3$ and $\varepsilon_{00} + 1.5k_{\mathrm{B}}T$. These results are exactly the same as the results of the Cartesian coordinate system, as the quadratic potential $\varepsilon_{\mathrm{vdW}} = \varepsilon_{00} + 0.5m\omega^2 r^2 = \varepsilon_{00} + 0.5m\omega^2 x^2 + 0.5m\omega^2 y^2 + +0.5m\omega^2 z^2$, and there is no correlation between the three directions.

Considering that the surfaces of materials are generally 2D, the models with two same types of potential indicate the symmetry parallel to the surface. Similar to the discussion above, the analysis with the Cartesian coordinate system shown in Table (2.1) also shows a universality. These results show that choosing different potentials leads to different K_{L} and Δu_{st}. The temperature dependence of Δu_{st} is determined once a model is chosen.

Considering the K_{L} in the Langmuir model has the following generalized form:

$$K_{\mathrm{L}} = \frac{\Lambda^3 q_{\mathrm{ads}}}{k_{\mathrm{B}}T} = \gamma \cdot \exp\left(-\frac{\varepsilon_{00}}{k_{\mathrm{B}}T}\right), \quad (2.45)$$

where this γ is a prefactor term, which is a power of temperature. The ε_{00} is invariant with temperature. Taking into Eq (2.23), the adsorption energy is given by:

$$\Delta u_{\mathrm{st}} = \frac{\partial\, \gamma}{\gamma} \cdot \frac{k_{\mathrm{B}}T^2}{\partial T} + \varepsilon_{00} + k_{\mathrm{B}}T. \quad (2.46)$$

2.4.2 2D Ideal Gas Model

A fundamental piece of the Langmuir model is configurational entropy in Eq. (2.32), and it assumes the adsorbed particles and sites are identical. However, once the particles are able to move out from the trap sites, the identical site model fails. This is highly possible at high temperatures like room temperature, as the mobility of the molecules in the supercritical phase at high temperatures is large. Therefore, a different model is required.

Again, as the surfaces are considered 2D, the intuitive idea is to treat the adsorbed molecule as free translational gas parallel to the surface and trapped horizontally to the surface. This is known as the "2D ideal gas model." (Hill, 1994; Campbell and Sellers, 2012; Campbell, Sprowl, and Arnadottir, 2016) Regarding the x and y directions are parallel to the surface and the z direction is horizontal to the surface, then q_x and q_y are both $1/\Lambda$, while q_z follows the discussion of the previous subsection. In this case, Eq (2.29) turns into:

$$q_{\text{ads}} = \frac{q_z}{\Lambda^2} \exp\left(-\frac{\varepsilon_{00}}{k_{\text{B}}T}\right) \iint \mathrm{d}x\mathrm{d}y = \frac{Aq_z}{\Lambda^2} \exp\left(-\frac{\varepsilon_{00}}{k_{\text{B}}T}\right), \tag{2.47}$$

where A is the size of the surface, and A/n is the average area taken by one molecule. The entropy of molecules replaces the configurational entropy of sites, and the canonical partition function is:

$$Q = \frac{1}{n!} q_{\text{ads}}^n = \frac{1}{n!} \left(\frac{Aq_z}{\Lambda^2}\right)^n \exp\left(-\frac{n\varepsilon_{00}}{k_{\text{B}}T}\right). \tag{2.48}$$

The Helmholtz free energy and the chemical potential of the adsorbed phase are:

$$F_{\text{ads}} = -k_{\text{B}}T \ln Q = nk_{\text{B}}T \ln n - nk_{\text{B}}T - nk_{\text{B}}T \ln\left(\frac{Aq_z}{\Lambda^2}\right) + n\varepsilon_{00}; \tag{2.49}$$

$$\mu_{\text{ads}} = \left(\frac{\partial F_{\text{ads}}}{\partial n}\right)_T = k_{\text{B}}T \ln n - k_{\text{B}}T \ln\left(\frac{Aq_z}{\Lambda^2}\right) + \varepsilon_{00}. \tag{2.50}$$

According to Eq (2.17) and Eq (2.19), this model gives the following isotherm:

$$n = \frac{P\Lambda Aq_z}{k_{\text{B}}T} \exp\left(-\frac{\varepsilon_{00}}{k_{\text{B}}T}\right), \tag{2.51}$$

which has the same expression as Henry's law shown in Eq (2.11). The Henry's constant is $K_{\text{H}} = \Lambda Aq_z \exp(\varepsilon_{00}/k_{\text{B}}T)/k_{\text{B}}T$. Substituting into Eq (2.12), the isosteric adsorption energy is:

$$\Delta u_{\text{st}} = \varepsilon_{00} + \frac{k_{\text{B}}T^2}{q_z}\frac{\partial q_z}{\partial T} - 0.5k_{\text{B}}T. \tag{2.52}$$

If q_z corresponds to one of the potentials shown in Fig. (2.1), the K_{H} and Δu_{st} of the 2D ideal gas model is shown in Table (2.2).

Compared with the results in Table (2.1), some fitting parameters have exactly the same form. For example, the 3 q_{SP} in Table (2.1) and the q_{SP} in Table (2.2). However, physically, they are not equivalent. At low pressure, the Langmuir model turns into Henry's law, and Henry's constant is: $N \cdot K_{\text{L}} = ND_1D_2D_3 \exp(-\varepsilon_{00}/k_{\text{B}}T)/k_{\text{B}}T$. Here, $D_1D_2D_3$ corresponds to the $D_xD_yD_z$, and D_xD_y is the area of the site.

Table 2.2: Several typical partition functions possible for the direction horizontal to the surface. The Henry's law constants K_H and the corresponding isosteric adsorption energies are both shown.

q_z	K_H	Δu_st
q_DF	$\Lambda A \exp(-\varepsilon_{00}/k_\mathrm{B}T)/k_\mathrm{B}T$	$\varepsilon_{00} - 0.5k_\mathrm{B}T$
q_SP	$DA \exp(-\varepsilon_{00}/k_\mathrm{B}T)/k_\mathrm{B}T$	ε_{00}
q_QP	$\Lambda A \exp(-\varepsilon_{00}/k_\mathrm{B}T)/\hbar\omega$	$\varepsilon_{00} + 0.5k_\mathrm{B}T$

Compared with the total surface area A, ND_xD_y is the total area of the sites, which is smaller.

Similar methods discussed in this subsection can be used for all the mobile gas molecules. The difference is that the calculation of the single particle partition function should follow Eq. (2.29) rather than Eq. (2.47).

2.5 Multi-Site Adsorption

The discussion in the previous sections is based on a single type of site. However, for real materials, there are multiple types of sites with different single particle partition functions q_1, q_2 ... q_i .... This section focuses on the generalization of both Henry's law and the Langmuir model. The basis is that, at equilibrium, the chemical potentials of these different sites are all equal to the chemical potential of the gas phase.

Using the 2D ideal gas model, assuming the total surface area is A, and the fractions of each type of surface are α_1, α_2, ...α_i ..., the numbers of adsorbed molecules on i^th type of surface are:

$$n_i = \frac{P\Lambda\alpha_i A q_{z,i}}{k_\mathrm{B}T} \exp\left(-\frac{\varepsilon_{00,i}}{k_\mathrm{B}T}\right). \tag{2.53}$$

The total amount of adsorption is the sum of n_i, and the total Henry's constant is:

$$K_\mathrm{H} = \sum_i \frac{\Lambda\alpha_i A q_{z,i}}{k_\mathrm{B}T} \exp\left(-\frac{\varepsilon_{00,i}}{k_\mathrm{B}T}\right). \tag{2.54}$$

Substituting Eq. (2.54) into the Clausius-Clapeyron equation, the adsorption energy is given by:

$$\begin{aligned}\Delta u_\mathrm{st} = -0.5k_\mathrm{B}T &+ \frac{\sum \alpha_i q_{z,i}\varepsilon_{00,i} \exp\left(-\varepsilon_{00,i}/k_\mathrm{B}T\right)}{\sum \alpha_i q_{z,i} \exp\left(-\varepsilon_{00,i}/k_\mathrm{B}T\right)} \\ &+ k_\mathrm{B}T^2 \frac{\sum \alpha_i \exp\left(-\varepsilon_{00,i}/k_\mathrm{B}T\right)\left(\partial q_{z,i}/\partial T\right)}{\sum \alpha_i q_{z,i} \exp\left(-\varepsilon_{00,i}/k_\mathrm{B}T\right)}.\end{aligned} \tag{2.55}$$

Another equivalent method of getting the isosteric adsorption energy is calculating the partition function from Eq. (2.30). Similar to Eq. (2.47), for multiple sites, the partition function is:

$$q_{\mathrm{ads}} = \frac{1}{\Lambda^2} \sum q_{z,i} \exp\left(-\frac{\varepsilon_{00,i}}{k_{\mathrm{B}}T}\right) \iint_i \mathrm{d}x\mathrm{d}y = \frac{A}{\Lambda^2} \sum \alpha_i q_{z,i} \exp\left(-\frac{\varepsilon_{00,i}}{k_{\mathrm{B}}T}\right). \tag{2.56}$$

The adsorbed phase internal energy is then:

$$\begin{aligned} u_{\mathrm{ads}} = \frac{k_{\mathrm{B}}T^2}{q_{\mathrm{ads}}} \cdot \frac{\partial q_{\mathrm{ads}}}{\partial T} &= \frac{\sum \alpha_i q_{z,i} \varepsilon_{00,i} \exp\left(-\varepsilon_{00,i}/k_{\mathrm{B}}T\right)}{\sum \alpha_i q_{z,i} \exp\left(-\varepsilon_{00,i}/k_{\mathrm{B}}T\right)} \\ &+ k_{\mathrm{B}}T^2 \frac{\sum \alpha_i \exp\left(-\varepsilon_{00,i}/k_{\mathrm{B}}T\right) \left(\partial q_{z,i}/\partial T\right)}{\sum \alpha_i q_{z,i} \exp\left(-\varepsilon_{00,i}/k_{\mathrm{B}}T\right)} + k_{\mathrm{B}}T. \end{aligned} \tag{2.57}$$

Substituting Eq. (2.57) into Eq. (2.10), Eq. (2.55) is also obtained.

For the multi-site Langmuir model, assuming the total number of sites is N, and the fractions of each type of site are $\alpha_1,\ \alpha_2,\ ...\alpha_i\ ...$, then according to Eq (2.37), the chemical potential of the i^{th} type of site is:

$$\mu_{\mathrm{ads},i} = -k_{\mathrm{B}}T \ln q_{\mathrm{ads},i} + k_{\mathrm{B}}T \ln \frac{n_i}{\alpha_i N - n_i}. \tag{2.58}$$

Then, according to Eq (2.19) there is:

$$n_i = \alpha_i N \frac{P\Lambda^3 q_{\mathrm{ads},i}/k_{\mathrm{B}}T}{1 + P\Lambda^3 q_{\mathrm{ads},i}/k_{\mathrm{B}}T}, \tag{2.59}$$

and the total adsorption amount is the sum of n_i (Stadie, 2013). At low pressure, the adsorption energy is similar to Eq. (2.55). At higher temperatures, however, it is easier to calculate the energy numerically.

2.6 Slit-Pore Model and NLDFT Method

The slit-pore model, illustrated in Fig. (2.2), is widely used to simulate porous materials. It regards the pore as a slit between two flat surfaces with a distance of D. Beyond the surfaces, there exist several extra layers of adsorbent. The spacing between these outer layers is D_{b}, which means the bulk distance. Similar to the 2D ideal gas model, the potential energy contribution from the adsorbent is homogeneous potential along the $x - y$ plane and is only a function of the position in the z direction (Lastoskie, Gubbins, and Quirke, 1993).

Based on the slit-pore model, a non-local density functional theory (NLDFT) shows an approach to characterize the pore size distribution (Olivier, 1995; Olivier, 1998;

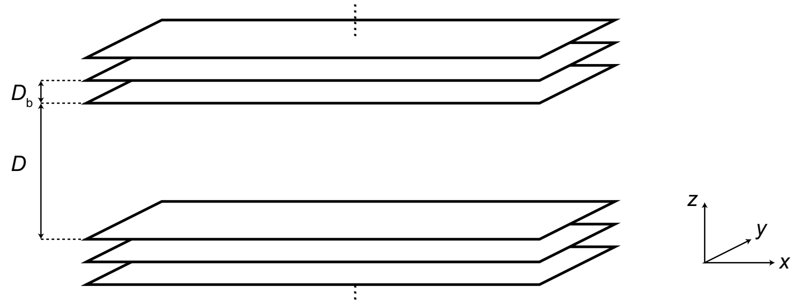

Figure 2.2: An illustration of the slit-pore model.

Kupgan, Liyana-Arachchi, and Colina, 2017; Jagiello and Kenvin, 2019). Compared with the multi-site adsorption discussed above, the NLDFT method still regards the pores with different surface distances as individual and equilibrium to the gas phase. However, the NLDFT method expands the discussion to the higher-pressure region. At a fixed temperature T, the total adsorption amount is given by:

$$n(P,T) = \int_D n_D(P,T) f(D) \mathrm{d}D = \int_D \int_{\vec{r^3}} \rho_D(P,T,\vec{r}) \mathrm{d}\vec{r^3} f(D) \mathrm{d}D, \tag{2.60}$$

where n_D is the adsorption amount by the pores with the width of D. $f(D)$ is the pore size distribution fraction, and ρ_D is the density of gas.

To calculate the ρ, compared with the DFT, NLDFT only uses the non-local vdW potential and follows the thermodynamic idea of minimizing the grand potential functional:

$$\Omega\left[\rho_D(\vec{r})\right] = F\left[\rho_D(\vec{r})\right] - \int \rho_D(\vec{r})\left[\mu - V_{\text{ext}}(\vec{r})\right] \mathrm{d}\vec{r^3}, \tag{2.61}$$

where F is the intrinsic Helmholtz free energy, μ is the chemical potential and V_{ext} is the external potential. Here, the adsorbate-adsorbate interactions are included in the F, while the adsorbate-adsorbent interactions are included in the V_{ext}. Different NLDFT models have different expressions of F and V_{ext}. As one of the earliest models, the 2D carbon-nitrogen model used the LJ potential and the mean-field theory (Jagiello, 1994). Recently, the Heterogeneous Surface model was proposed, which used curve surfaces rather than flat surfaces to describe the pores (Jagiello and Kenvin, 2019). The gas density can be calculated when the model is decided and when D and $\mu(P,T)$ are given. Then $n_D(P,T)$ is calculated by integral, as shown in Eq. (2.60). The series of n_D functions are named "kernels."

Chapter 3

EXPERIMENTAL OBSERVATION OF THE TEMPERATURE DEPENDENCE OF PHYSISORPTION ENERGY

3.1 Experimental Setup

This study chooses porous carbon materials and krypton as the adsorbent and adsorbate. Porous carbon materials have high surface areas and suitable pore sizes for adsorbent materials. These materials are also widely used and easily accessible. For the adsorbate, krypton has large polarizability (2.498 Å^3) (Olney et al., 1997), which means the adsorption of krypton is easily observable. This polarizability is also close to methane's polarizability (2.448 Å^3) (Olney et al., 1997), and the study of methane adsorption is an important topic in environmental and energy sciences. Compared with methane, krypton is isotropic and has no internal degrees of freedom, which is easier for thermodynamic theory study and vdW potential calculation.

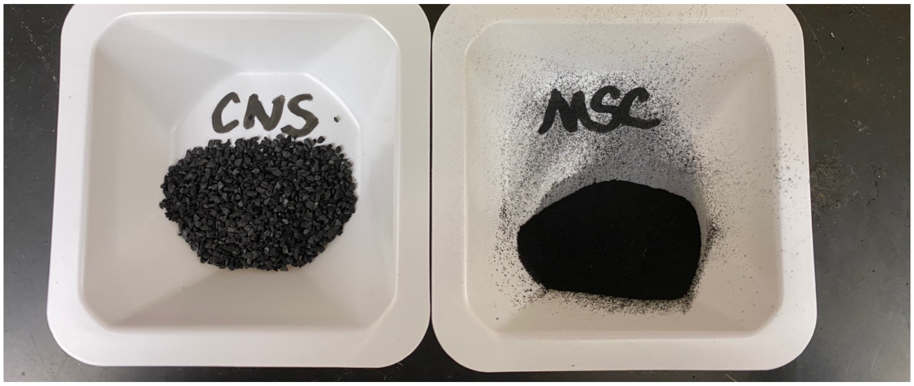

Figure 3.1: Picture of the two types of porous carbon materials. Left: CNS-201. Right: MSC-30. CNS-201 is made from the coconut shell and has the shape of small grain. MSC-30 is a powder material. The size of the plastic plates is 10 cm × 10 cm.

Two types of porous carbon were used as the adsorbent: MSC-30 from Kansai Coke & Chemicals Company Ltd. (Japan) and CNS-201 from A. C. Carbone Inc. (Canada), shown in Fig. 3.1. The ultra-high purity argon gas with a purity of 99.999% was from Airgas company. The research-grade krypton gas with a purity of 99.998% was from Air Liquide Corp.

Generally speaking, there are two major methods to study isosteric adsorption energy or enthalpy. The direct method uses calorimetry to measure the heat evolved during adsorption (Fang et al., 2012; Rubes et al., 2018; Hyla et al., 2019; Shen et al., 2000). The indirect method is fitting isotherms at different temperatures and calculating the adsorption enthalpy from the Clausius-Clapeyron equation (Huang, 1972; Helmy, Ferreiro, and Bussetti, 1996; Shen et al., 2000; Farrusseng et al., 2009; M. Murialdo et al., 2015; Son et al., 2018; Yu et al., 2021). This work uses the indirect method. The TriStar II 3020 system from Micromeritics was used to collect argon adsorption isotherms for the measurement of the pore size and surface area distribution and was used to collect krypton adsorption isotherms for the adsorption energy analysis.

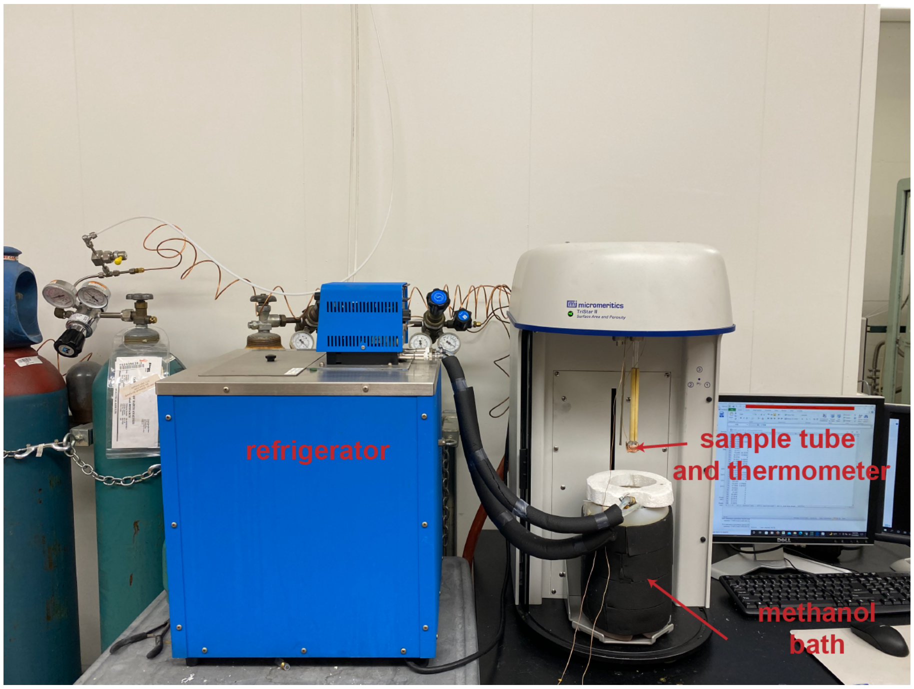

Figure 3.2: The setup of the krypton adsorption measurement at different temperatures. The refrigerator cycles methanol at different temperatures. The methanol in the refrigerator goes through the condensing coil in the bath bottle and delivers heat to the methanol in the bath. After waiting for enough time and when the two types of methanol reach equilibrium, the methanol bath bottle is raised up and the sample tube is sunk inside the bath. One thermometer sensor is attached to the sample tube, and another sensor is sunk inside the bath. Temperature is measured every second during the experiment.

Argon adsorption isotherms were measured at 87 K. Liquid argon in the dewar was used to stabilize the temperature. Pore-size distributions were given by the NLDFT analysis in the Micromeritics system with the "Carbon-Ar-87 K, 2D-NLDFT

Heterogeneous Surface" model (Jagiello and Kenvin, 2019). The densities of the materials are set as 2.1 g/cm^3 according to previous research(Stadie, 2013; M. Murialdo et al., 2015).

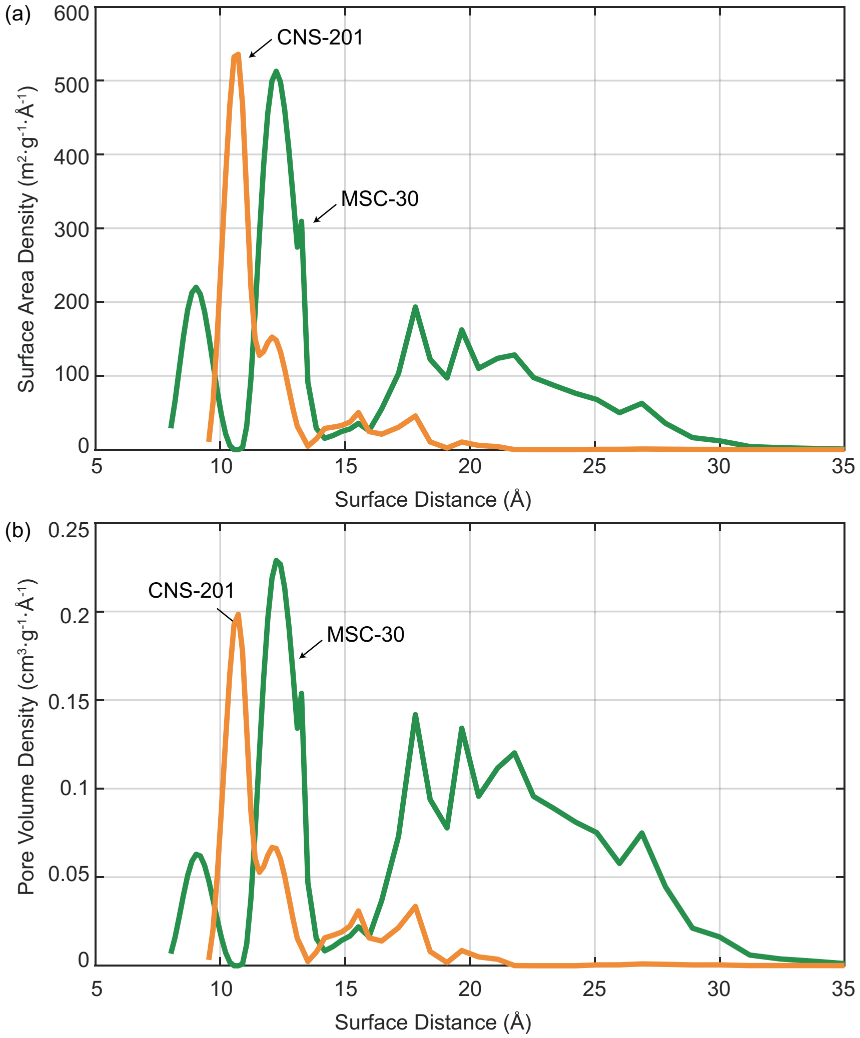

Figure 3.3: NLDFT analysis results of CNS-201 (orange) and MSC-30 (green). (a) Surface area distributions. (b) Pore volume distributions. Results are given by NLDFT analysis of argon adsorption measurements at 87 K. The surface distance is the absolute pore width rather than the effective pore width.

Krypton equilibrium adsorption isotherms were measured from 250 K to 330 K. The quantities of adsorbed krypton were recorded at different pressure values set in advance. A methanol bath kept the temperature stable during the data collection process, and the temperature fluctuations were within 0.5 K. The setup of these measurements is shown in Fig. (3.2). The temperature range is decided by the melting point and flash point of methanol.

3.2 Pore-Size Measurement and Isotherms

The NLDFT surface area distributions and pore volume distribution of CNS-201 and MSC-30 are shown in Fig. (3.3). The prominent surface distance for CNS-201 are 10.7 Å and 12.1 Å. For MSC-30, there are two peaks at 9.0 Å and 12.2 Å, containing around 13% and 35% of the surface area. The cumulative NLDFT pore volumes are 0.419 cm^3/g and 1.593 cm^3/g, and the cumulative NLDFT surface areas for the two materials are 960 m^2/g and 2371 m^2/g. As a reference, the BET surface area for CNS-201 and MSC-30 are 977 m^2/g and 3359 m^2/g.

The equilibrium excess adsorption at different temperatures and pressures of krypton on CNS-201 and MSC-30 are shown in Fig. (3.4a) and (3.4b). At the same pressure and temperature, the adsorption amounts on these two materials are similar. However, the isotherm curvatures of CNS-201 are more obvious than MSC-30.

For a typical adsorption amount of 0.5 mmol in Fig. (3.4), the average NLDFT surface areas taken by one molecule are 318 Å^2 for CNS-201 and 787 Å^2 for MSC-30, and the average BET surface areas for one molecule on CNS-201 and MSC-30 are 324 Å^2 and 1116 Å^2. These values are not small, as the average distance between the gas atoms is more than 18 Å for CNS-201 and 28 Å for MSC-30. As a comparison, for the ideal gas at 300 K and under 5×10^4 Pa, the average distance between molecules is 43 Å.

3.3 Data Analysis

3.3.1 Henry's Law Analysis

The experimental results are first analyzed with Henry's law. To fulfill the applicability of Henry's law, only the data points with adsorption below 0.3 mmol are adopted for calculating Henry's constant at low temperatures. At high temperatures, only the first 15 data points are adopted. The results of Henry's constants and the linear fitting results are shown in Fig. (3.5).

The zero-adsorption Henry's constants at different temperatures are acquired from the intercepts at the vertical axes. Taking these zero-adsorption Henry's constants into Eq. (2.12) and using $\delta K/\delta T$ as $\partial K/\partial T$, the adsorption energies at different temperatures are shown in Fig. (3.6). The circles are the changes in the internal energies during adsorption, and the trend is that, with the temperature increase, the adsorption energies for both materials turn weaker. The dash lines in Fig. (3.6) are linear fittings, and the slopes of these lines are $4.35k_\text{B}$ and $3.65k_\text{B}$ for CNS-201 and MSC-30. From 250 K to 330 K, the adsorption energy changes from -0.221 eV to

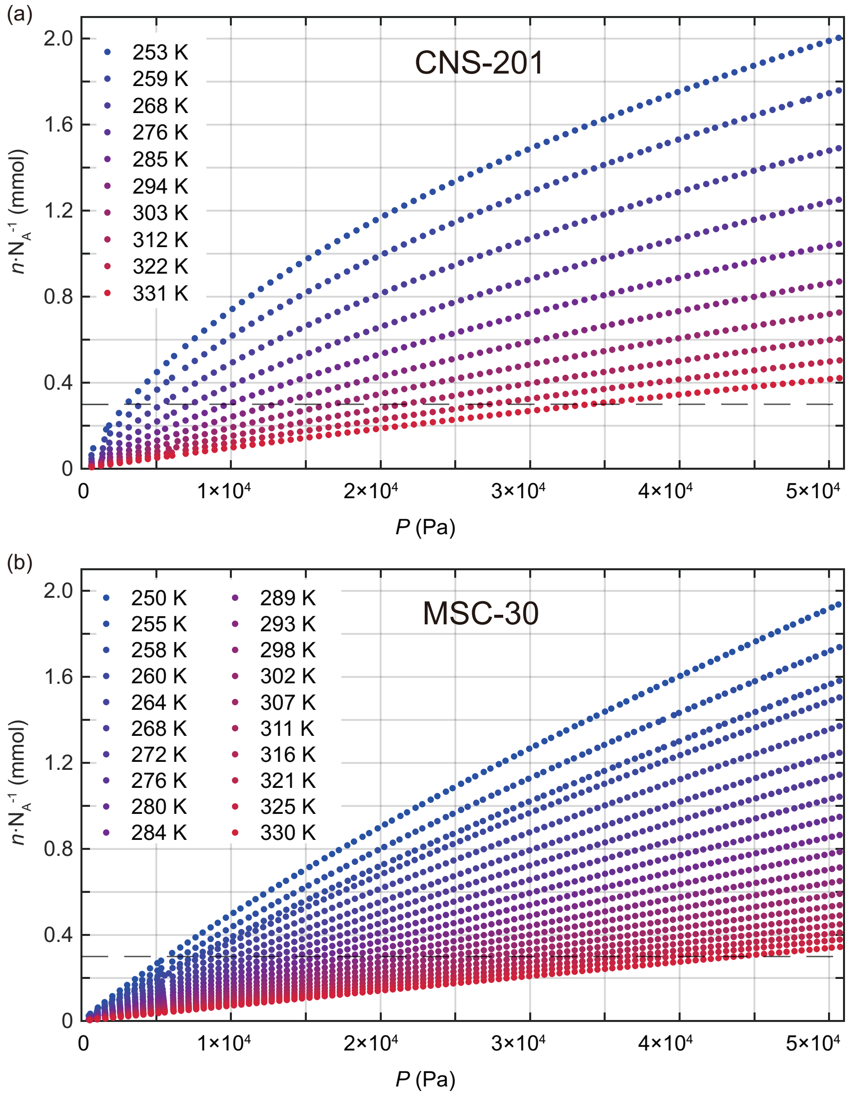

Figure 3.4: Equilibrium excess adsorption of krypton on (a) CNS-201 and (b) MSC-30 at different temperatures. The dots show the experiment numbers of adsorbed molecules per gram of adsorbent. Henry's constants are obtained according to the data below the dash line threshold to ensure the coverage is dilute.

-0.194 eV for CNS and from -0.173 eV to -0.148 eV for MSC. The changing rates are 13% and 15%.

Assuming the gas is ideal, and considering the volume of the adsorbed phase is ignorable, the adsorbed phase heat capacity is:

$$c_{\mathrm{ads}} = \frac{\partial h_{\mathrm{ads}}}{\partial T} = \frac{\partial u_{\mathrm{ads}}}{\partial T} = \frac{\partial(\Delta u_{\mathrm{st}} + u_{\mathrm{gas}})}{\partial T} = \frac{\partial \Delta u_{\mathrm{st}}}{\partial T} + 1.5 k_{\mathrm{B}} T. \tag{3.1}$$

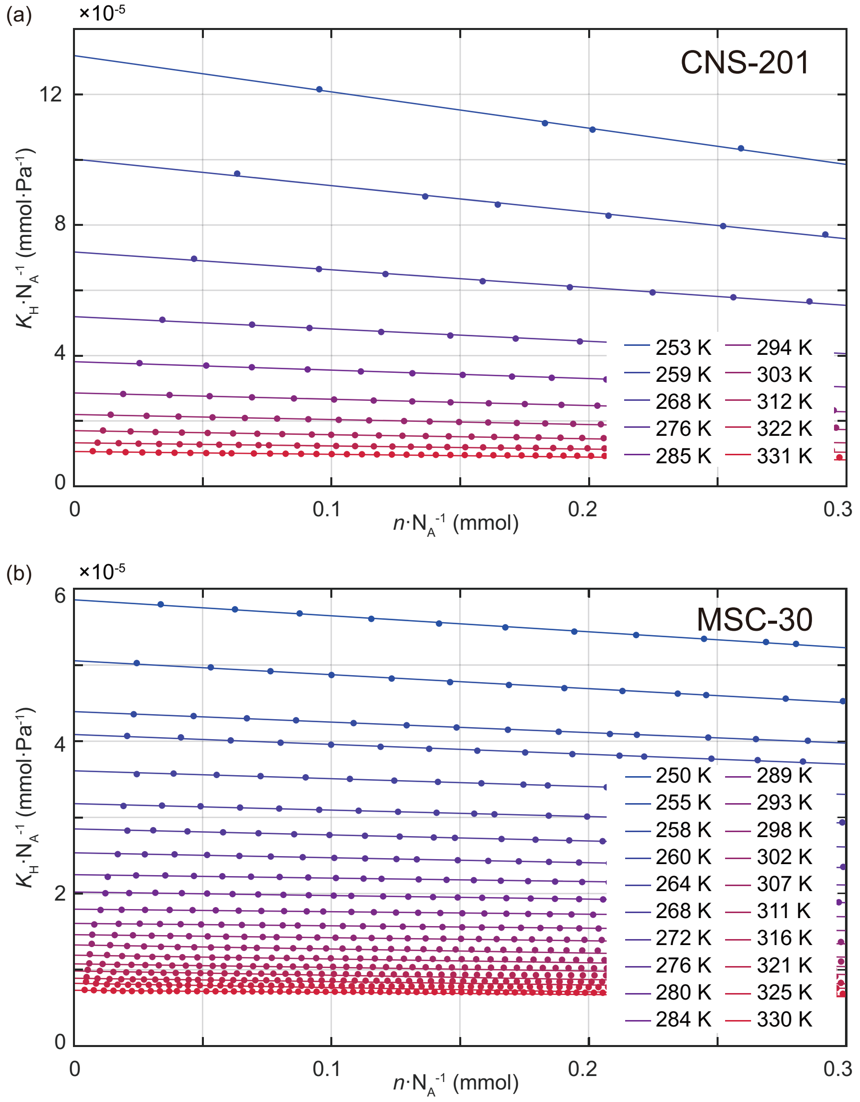

Figure 3.5: Henry's constants of krypton adsorption on (a) CNS-201 and (b) MSC-30 at different temperatures. For high temperatures, the linear fitting lines are acquired by the initial 15 data points. The results are based on the adsorbent per gram.

Taking the slopes into Eq. (3.1), the adsorbed phase heat capacities for CNS-201 and MSC-30 are $5.85k_\mathrm{B}$ and $5.16k_\mathrm{B}$. This adsorbed phase heat capacity is much larger than the 3D ideal krypton constant volume heat capacity, which is $1.5k_\mathrm{B}$.

3.3.2 Langmuir Model Analysis

The experimental results are also analyzed with the Langmuir model. Universal N values are picked to minimize the total square errors. The fitting isotherms are shown

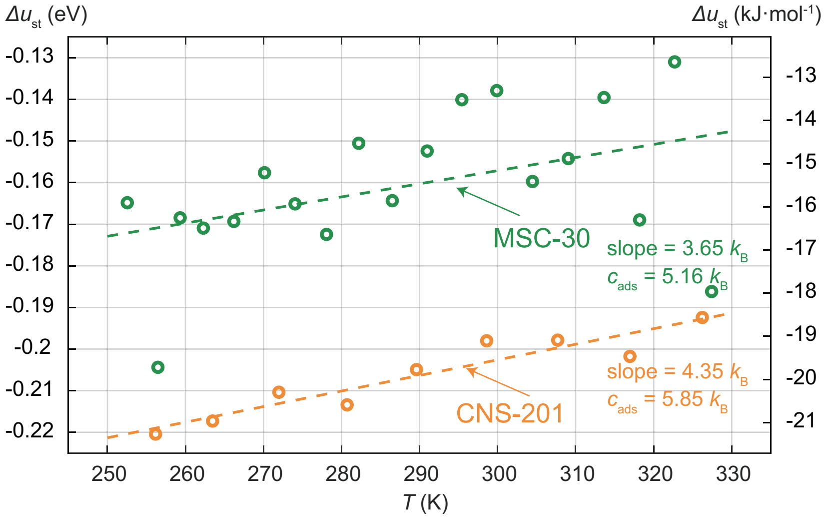

Figure 3.6: Isosteric adsorption energies Δu_{st} at zero adsorption of krypton adsorption on CNS-201 (orange) and MSC-30 (green) given by Henry's law.

in Fig. (3.7). The N values for a gram of CNS-201 and MSC-30 are 2.10 mmol and 5.57 mmol, and the K_L values are shown in Fig. (3.8).

By taking the K_L in Eq. (2.23) and using $\delta K/\delta T$ as $\partial K/\partial T$, the adsorption energies are given in Fig. (3.9). Similar to Henry's law analysis, the slopes and corresponding adsorbed phase heat capacities are also shown. The slopes of these lines are $2.10k_{\mathrm{B}}$ and $1.21k_{\mathrm{B}}$ for CNS-201 and MSC-30. From 250 K to 330 K, the adsorption energy changes from -0.204 eV to -0.189 eV for CNS and from -0.159 eV to -0.151 eV for MSC. The changing rates are 8‰ and 5‰.

According to the Langmuir model analysis, the adsorbed phase heat capacities are smaller than the results from Henry's law analysis. However, they are still much larger than the 3D ideal krypton constant volume heat capacity. Comparing Fig (3.9) and Table. (2.1), the slope of Δu_{st} of CNS-201 is even larger than the "$3q_{\mathrm{QP}}$," while the slope of Δu_{st} of MSC-30 is between the "$3q_{\mathrm{QP}}$" and "$2q_{\mathrm{QP}}$ & $1q_{\mathrm{SP}}$" situations.

Using the temperature depend slopes shown in Fig (3.9) and Eq. (2.46), the prefactors of K_{L} for CNS-201 and MSC-30 are in proportion to $T^{2.10}$ and $T^{1.21}$. The fittings of K_{L} based on these prefactors are shown with dash lines in Fig (3.8). The ε_{00} for CNS-201 and MSC-30 are -0.273 eV and -0.208 eV.

Although the prefactor forms given by Fig (3.9) show a good fitting with the results in Fig (3.8), the fitting with other forms of prefactors are also practiced, and the results are shown in Fig. (3.10). These fittings are based on the prefactor in proportion to

$T^{1.0}$, $T^{1.5}$, $T^{2.0}$, and $T^{2.5}$. The R-square values of these fittings are all more than 0.9999, and the total square errors are all smaller than 0.002. These parameters mean that all these models are reasonable for fitting the isotherms.

However, when considering the values of the thermodynamic terms, these models show completely different results. The ε_{00} for CNS-201 of these models are -0.248 eV, -0.260 eV, -0.271 eV, and -0.282 eV. The ε_{00} for MSC-30 of these models are -0.204 eV, -0.214 eV, -0.227 eV, and -0.239 eV. Meanwhile, as men-

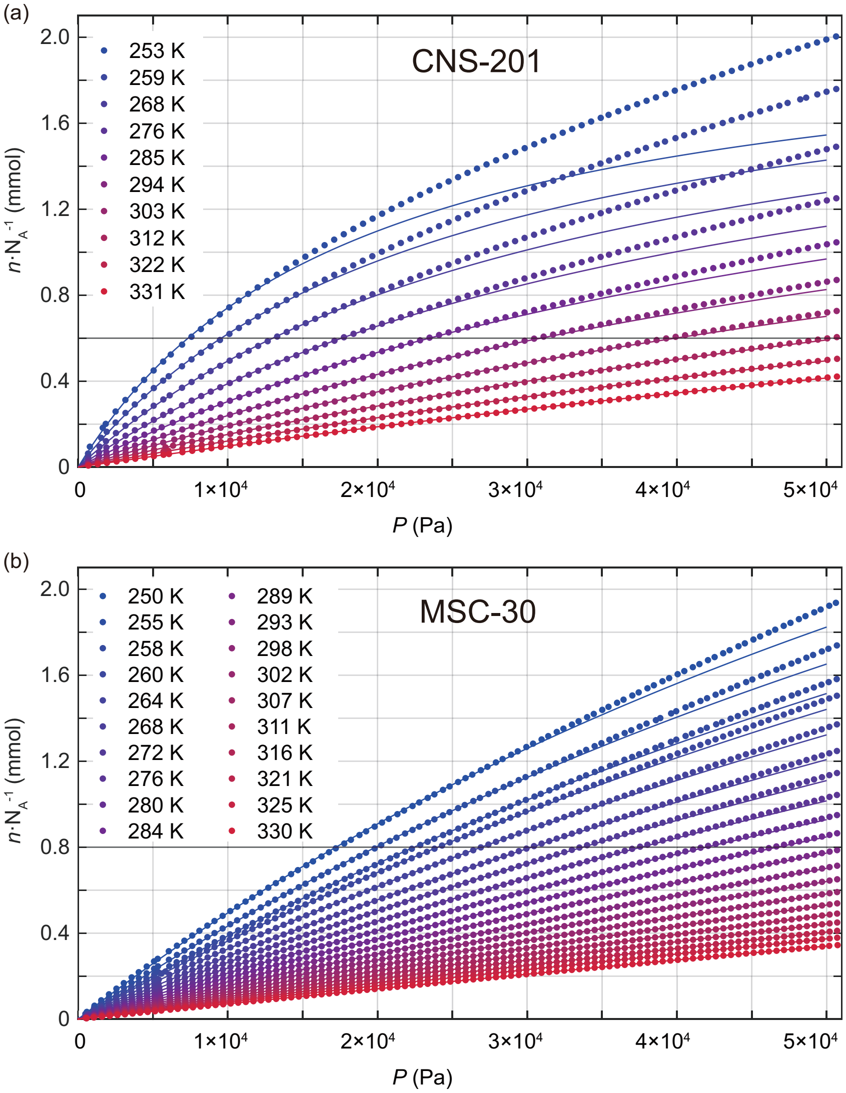

Figure 3.7: The dots are the experimental results shown in Fig. (3.4). The lines are the Langmuir fitting isotherms of CNS-201 and MSC-30 at different temperatures. Fittings are based on the results below the black lines.

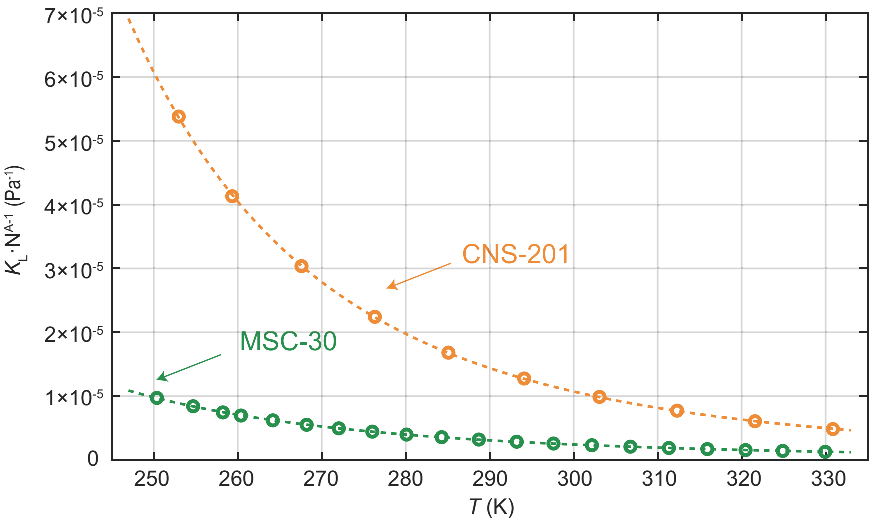

Figure 3.8: Langmuir fitting parameter K_L for CNS-201 (orange) and MSC-30 (green) at different temperatures. The fittings with Eq. (2.45) are shown with dash lines.

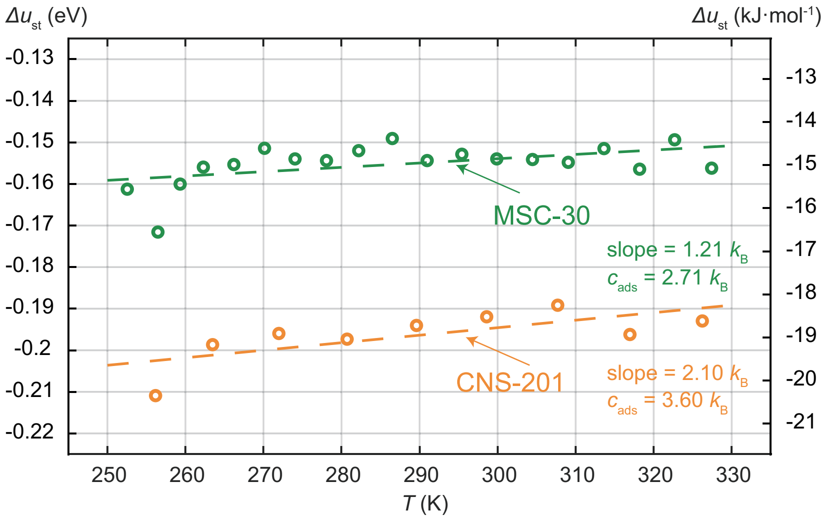

Figure 3.9: Isosteric adsorption energies Δu_{st} at zero adsorption of krypton adsorption on CNS-201 (orange) and MSC-30 (green) given by Langmuir model.

tioned before, the changing rates of Δu_{st} with temperature are 1.0 k_{B}, 1.5 k_{B}, 2.0 k_{B}, and 2.5 k_{B}, which may not be suitable for fitting the results in Fig (3.9). Therefore, the prefactor's exact form should not be assigned before fitting to study the adsorption energy's temperature dependence.

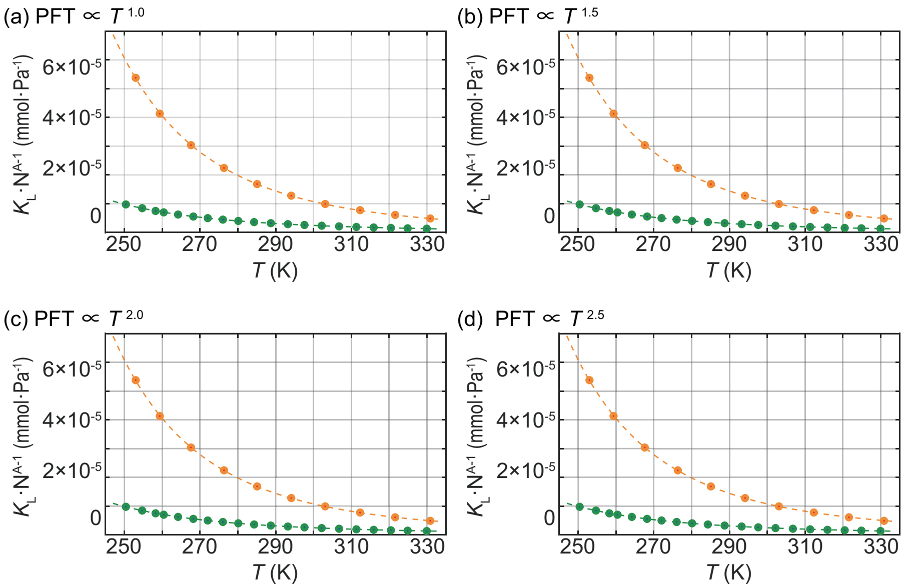

Figure 3.10: Langmuir fitting parameter K_L for CNS-201 (orange) and MSC-30 (green) at different temperatures. The fittings with different forms of prefactors are shown with dash lines.

Chapter 4

COMPUTATIONAL CALCULATION OF ADSORBED PHASE INTERNAL ENERGIES

In this chapter, DFT calculations give the adsorbed phase internal energies of pores with different sizes. The first section will compare different DFT vdW algorithms mentioned in the first chapter based on the model of krypton adsorption on carbon layers. The MBD algorithm is chosen among all the models due to its ability to capture many-body effects. The second section will use DFT-calculated vdW potentials and slit-pore thermodynamic analysis to calculate the adsorbed phase internal energies. The first two subsections show the results obtained from a simplified model, while the other subsections validate the simplification. The third section investigates the impact of atom displacements caused by thermal vibration on the adsorbed phase internal energy. It demonstrates that the effects of thermal displacements can be ignored in adsorption.

4.1 Comparison Between Different DFT Algorithms

In the first chapter, several different DFT algorithms for the vdW potential were proposed, including DFT-D2, DFT-D3, TS, and MBD (Grimme, 2006; Grimme et al., 2010; Grimme, 2011; Tkatchenko and Scheffler, 2009; Tkatchenko, Distasio, et al., 2012). These methods are all good for simple pairwise interactions. However, the many-body effect is not neglectable for surfaces with multiple atoms. In this section, the surface adsorption potentials given by these algorithms are compared.

The Vienna Ab Initio Simulation Package (VASP) was used for all *ab initio* DFT calculations (Kresse and Hafner, 1993; Kresse and Furthmuller, 1996a; Kresse and Furthmuller, 1996b) with plane wave basis sets, projector augmented wave (PAW) pseudopotentials, and the Perdew-Burke-Ernzerhof (PBE) functional (Kresse and Hafner, 1994; Kresse and Joubert, 1999). All calculations used a 3×3×1 k-grid and a default kinetic energy cutoff.

The first model is shown in Fig. (4.1), where a krypton atom is placed above a graphene layer. The cell in this model contains 3×3 graphene unit cells with 18 carbon atoms. In the vertical direction, the cell is 50 Å long, which has enough vacuum space to avoid the impact from adjacent cells. The krypton is moved along the dash lines shown in Fig. (4.1a) and (4.1c) from 2 Å to 18 Å away from the graphene with the step of 0.1 Å. A smooth fitting of the potential is applied to increase the resolution to 0.025Å. The vdW adsorption potential was calculated with the following equation:

$$\varepsilon_{\mathrm{vdW}} = \epsilon_{\mathrm{sys}} - \epsilon_{\mathrm{C}} - \epsilon_{\mathrm{Kr}} \tag{4.1}$$

where the ϵ_{sys}, ϵ_{C}, and ϵ_{Kr} are the DFT calculated energy of the system, the carbon adsorbent, and the krypton adsorbate. Due to the limitation on VASP, the direct calculated ϵ_{Kr} is inaccurate for Eq (4.1). To get the ϵ_{Kr}, an indirect method with the model in Fig. (4.1a) is used. When the krypton atom is 18 Å away from the carbon layer, $\varepsilon_{\mathrm{vdW}}$ is assumed to be 0. The difference between the system energy and the carbon energy in this situation is regarded as the energy of the krypton. The results of the vdW potentials are shown in Fig. (4.1b) and (4.1d). The locations and the energies of the potential wells are presented in Table. (4.1).

Table 4.1: The positions and energies of the potential wells shown in Fig. (4.1).

		DFT-D2	DFT-D3	TS	MBD
center site	position (Å)	3.425	3.575	3.575	3.600
	energy (eV)	-0.131	-0.120	-0.134	-0.101
corner site	position (Å)	3.475	3.625	3.625	3.650
	energy (eV)	-0.123	-0.117	-0.127	-0.097

In Fig. (4.1b) and (4.1d), all the potentials have a similar shape, where with the increase of distance, the potentials first quickly go to the bottom well and then gradually go back to 0. The results of DFT-D2 can be regarded as a reference where the most straightforward LJ potential is used, and no electronic structure is considered.

It is widely known, however, that graphene electrons form two large pi bonds on the two sides of the graphene. The vdW potential is then the interaction between krypton and two dipoles formed by the carbon nucleus and the pi bonds, and each dipole has a similar form of vdW potential with the DFT-D2 result. By considering the electronic structure of these dipoles, there are several effects. First, the position of the potential well should be further to the carbon layer. It is due to the repulsion from the pi bond above the graphene layer. When moving the krypton atom further to the graphene, the weakening in the vdW potential with the pi bond below the graphene layer is less significant than the enhancement in the vdW potential with

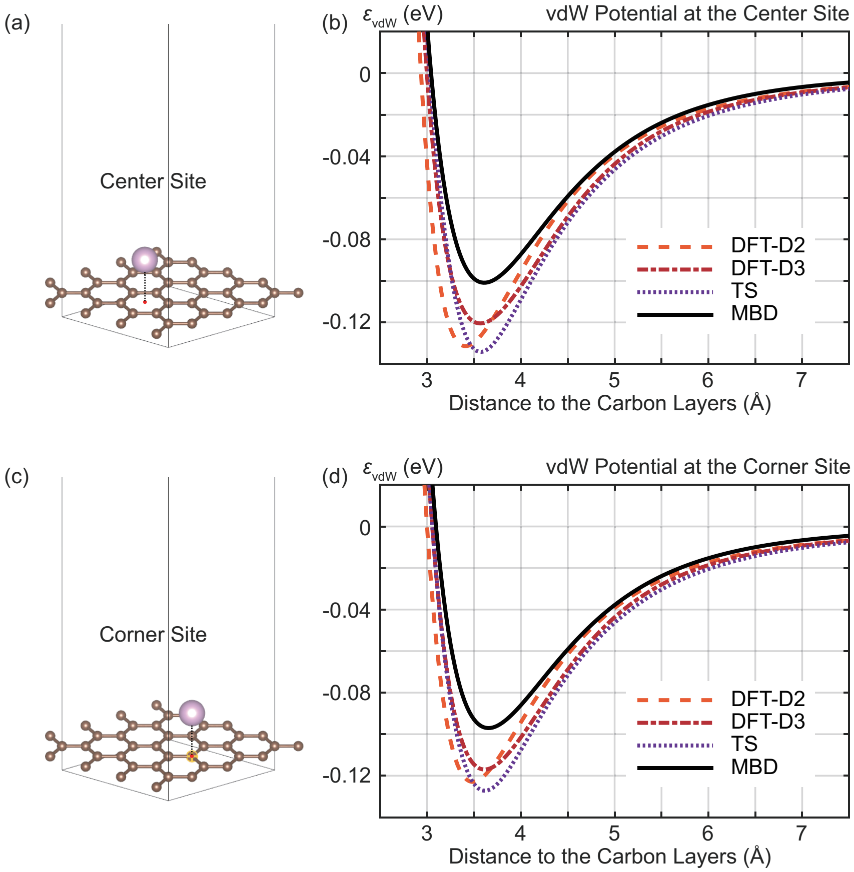

Figure 4.1: The model with a krypton atom above a single graphene layer and the corresponding vdW potentials. (a) shows a krypton above the center of the carbon hexagon. (c) shows a krypton above the corner of the carbon hexagon. (b) and (d) show the calculated vdW potential along the dash line in (a) and (c). Results with different algorithms are shown with different line styles and colors.

the pi bond above the graphene layer. The DFT-D3, TS, and MBD algorithms all show this change in position. Second, the vdW potential should be shallower, as the potential wells of these two dipoles are no longer at the same position. The DFT-D3 and MBD methods reproduce this effect.

Comparing the results of the center site and corner site, the center site potential wells are deeper (Maiga and Gatica, 2018). It is because the center sites have 6 nearest neighbors, and these carbon atoms all contribute the most substantial vdW potential. The corner sites have only 1 nearest and 3 second nearest neighbors, and the potential wells for these neighbors are not at the same position. However, due to the formation of the pi bonds, the electron distribution should be more even. That means the difference between the potential wells of the corner and center sites is smaller when considering electronic structure. The percentage differences between the energies of these two wells are 6.69% (DFT-D2), 2.87% (DFT-D3), 5.21% (TS), and 4.15% (MBD). The DFT-D3, TS, and MBD methods all show smaller energy changes compared with DFT-D2.

The second testing model is shown in Fig. (4.2), with two layers of carbon and one krypton above the carbon layers. The two carbon layers are extracted from the 3×3×1 graphite unit cells, and the distance between the two layers is 3.325 Å. The krypton atom above the corner site of the top layer is above the center site of the bottom layer, and vice versa. The potentials shown in Fig. (4.2b) and (4.2d) correspond to the structure in Fig. (4.2a) and (4.2c). The reference potential is given by a sum of the individual potentials from the two layers, and the individual potentials are given by Fig. (4.1).

Table 4.2: The positions and energies of the potential wells shown in Fig. (4.2). The sites are based on the top layer.

		DFT-D2	DFT-D3	TS	MBD
center site	position (Å)	3.400	3.550	3.550	3.600
	energy (eV)	-0.141	-0.129	-0.159	-0.112
corner site	position (Å)	3.475	3.600	3.600	3.625
	energy (eV)	-0.132	-0.125	-0.148	-0.107

The potentials are similar to those of the previous model. Compared with the reference potentials, the results of the DFT-D2 method are exactly the same. It is because DFT-D2 is based on the sum of pairwise LJ potentials. The results of DFT-D3 are also almost the same. The vdW potential given by the DFT-D3 method is still the sum of pairwise LJ potentials. The DFT-D3 method only modifies the parameters in the LJ potential by the coordinates of the nearby atoms, and it can not feel the non-local impact from another layer of carbon.

Compared with the reference, the potential wells of the TS method are 8.6% deeper at the center site and 8.9% deeper at the corner site. The potential wells of the MBD method are 4.3% deeper at the center site and 4.4% deeper at the center site.

Table 4.3: The positions and energies of the potential wells shown in Fig. (4.3).

	DFT-D2	DFT-D3	TS	MBD
position (Å)	+0.050	+0.025	+0.025	+0.025
potential (eV)	-0.240	-0.236	-0.254	-0.194

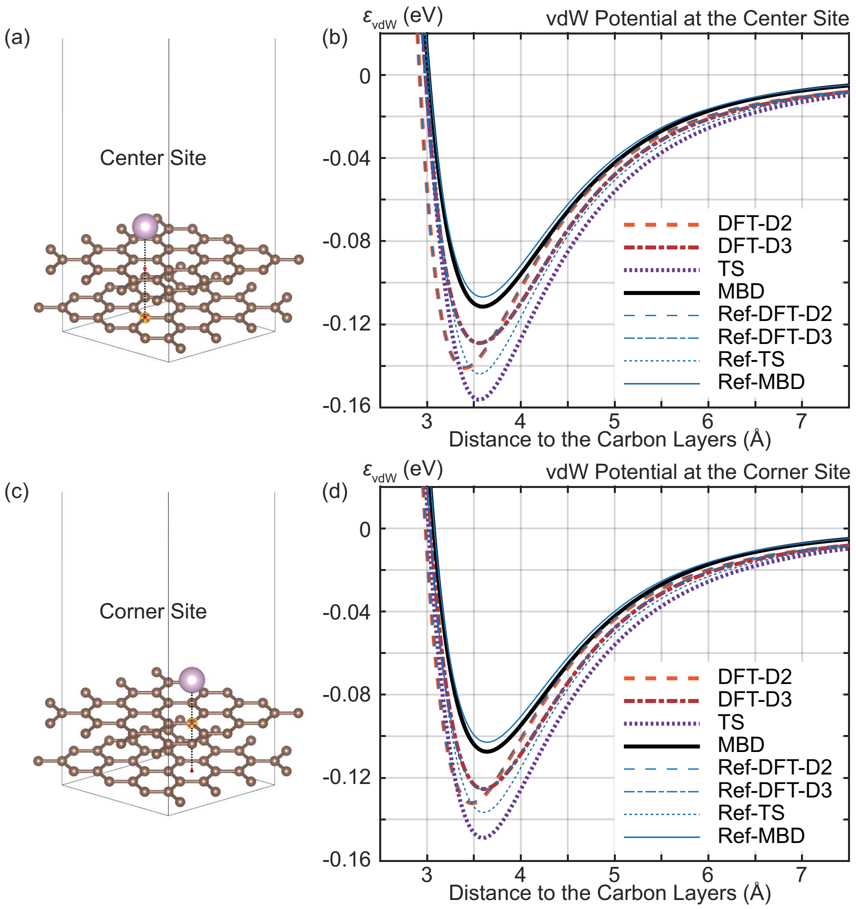

Figure 4.2: The model with a krypton atom above two graphene layers and the corresponding vdW potentials. (a) shows a krypton atom above the center of the carbon hexagon of the top layer. (c) shows a krypton atom above the corner of the carbon hexagon of the top layer. (b) and (d) show the calculated vdW potential along the dash line in (a) and (c). Results with different algorithms are shown with different line styles and colors. The reference lines are shown with thin blue lines. These reference lines are given by direct adding the vdW potential from the two carbon layers.

This can be illustrated as the two layers of carbon polarize the krypton electrons in the same direction. The krypton electrons are repulsed further to the carbon layers by the carbon pi bonds. The total polarization of the krypton is the sum effects of the two layers and is larger than the individual effect of any one layer. This larger polarized electron structure is then used for calculating the interactions with the two carbon layers, and the total vdW potential turns out to be larger. These observable deeper potential wells compared to the reference indicate that TS and MBD algorithms successfully show the non-local many-body effects.

The third testing model is shown in Fig. (4.3), with two layers of carbon and one krypton atom between the two layers. The two carbon layers are extracted from the 3×3×1 graphite unit cells and separated for 7.3 Å. The krypton atom above the corner site of the top layer is above the center site of the bottom layer, and vice versa. The potentials shown in Fig. (4.3b) correspond to the structure in Fig. (4.3a). The reference potential is still given by a sum of the individual potentials given by Fig. (4.1).

In this model, the DFT-D2 potential still overlaps with the reference potential and is clearly non-symmetry. That's due to the large difference between the corner site potential and center site potential, as shown in Fig. (4.1). The potentials are more symmetric for all the other potentials due to the pi bond. The DFT-D3 potential also overlaps with its reference, while the TS and MBD algorithms show the many-body effects. Compared with the results in Fig. (4.2), these potentials are smaller than the reference. That's because the polarization of the krypton atom by the two carbon layers is in opposite directions, and the total polarization of krypton is then smaller.

By comparison of the results by different vdW algorithms, the MBD model shows advantages over other algorithms. It can show the effects of the pi bonds in one

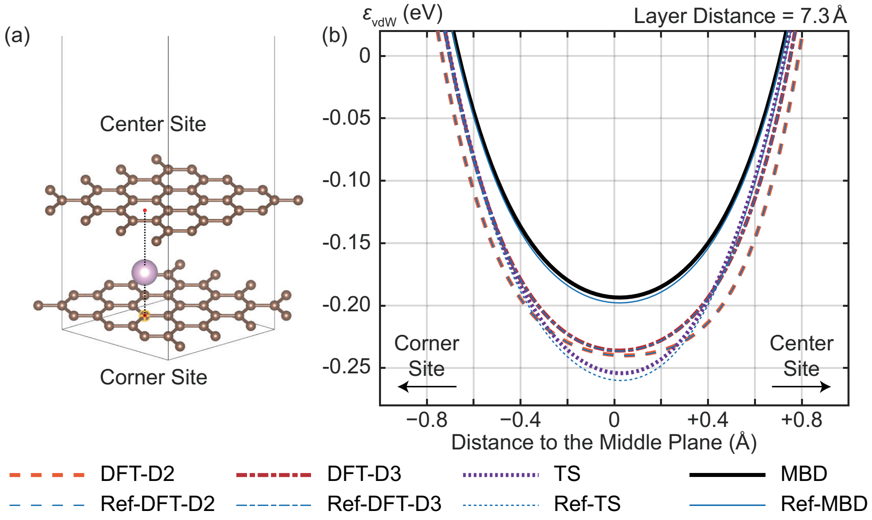

Figure 4.3: The model with a krypton atom between four layers of graphene. (a) The dash line shows a krypton atom above the carbon hexagon corner and below the carbon hexagon center. (b) The calculated vdW potential along the dash line in (a). Results with different algorithms are shown with different line styles and colors. The reference lines are shown with thin blue lines. These reference lines are given by direct adding the vdW potential from the two carbon layers.

graphene layer and the non-local effects of the two carbon layers in the graphite. Therefore, the MBD algorithm is chosen for later analysis.

4.2 Slit-Pore Model

4.2.1 Potentials of the Pores

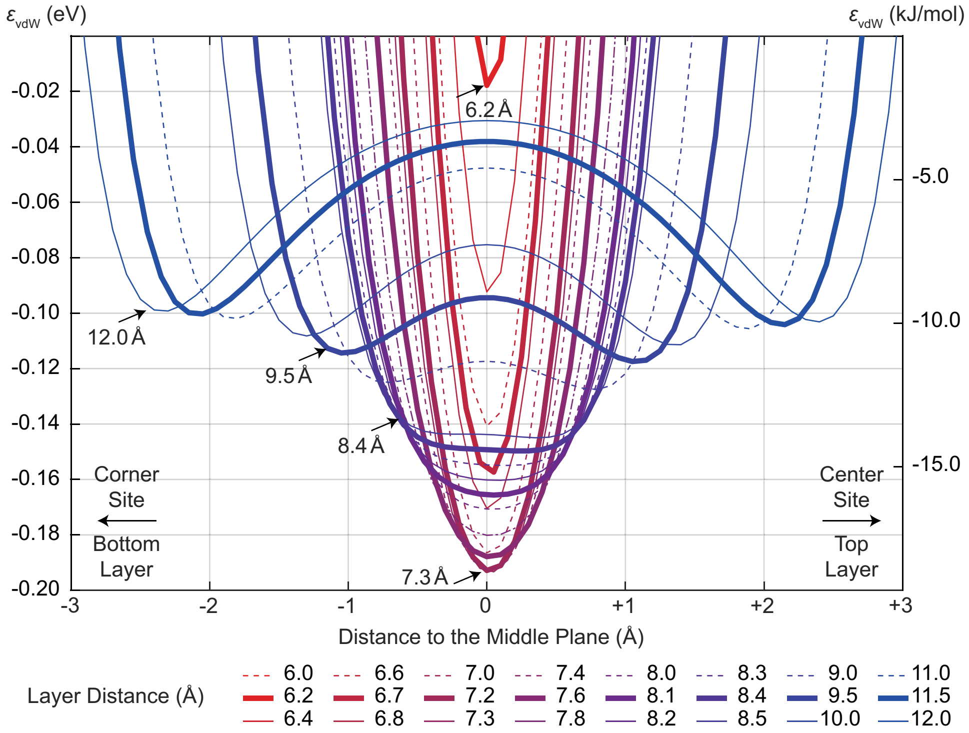

Figure 4.4: Computed vdW potential energies ε_{vdW} for selected layer distances along the dash line in Fig. (4.3). Different types of lines are used for distinguishing. The legend shows the color corresponding to different layer distances.

According to the results in Fig. (4.1), the energy change is small along the carbon surfaces. According to the results in Fig. (4.3), the energy change is large vertically to the carbon surfaces. Therefore, the structure shown in Fig. (4.3) is adapted for further slit-pore model analysis discussed in Chapter 2. The two layers of carbon are separated for various distances from 6.0 Å to 12.0 Å to simulate the potential of the pores with different sizes, and the results are given in Fig. (4.4).

In Fig. (4.4), when the layer distance is smaller than 6.2 Å, the vdW potential is almost positive, which means the carbon can hardly adsorbed the gas. The two layers are too close to each other, and the repulsive potentials from the two layers dominate. When the layer distance increases to around 7.3 Å, the potential wells from two different layers overlap, and the total adsorption energy reaches an extremum.

In the layer distance range from 6.2 Å to 7.3 Å, the potential well is similar to a quadratic function, while the curvature of this quadratic function is smaller with the layer distance increase. This trend can be seen by comparing the potential wells of 6.4 Å, 6.7 Å, and 7.3 Å shown in Fig. (4.5). For their fitting results, the coefficients of the quadratic terms for these potentials are 2.15, 2.03, and 1.82, and the unit is eV/Å^2. These results correspond to the harmonic oscillators with $\hbar\omega$ of 14.6 meV, 14.2 meV, and 13.5 meV. Also, with larger layer distances, the potential deviates more from the quadratic fitting. The quadratic functions increase slower than the real potential because the bottoms of the potential wells begin to flatter at a 7.3 Å layer distance.

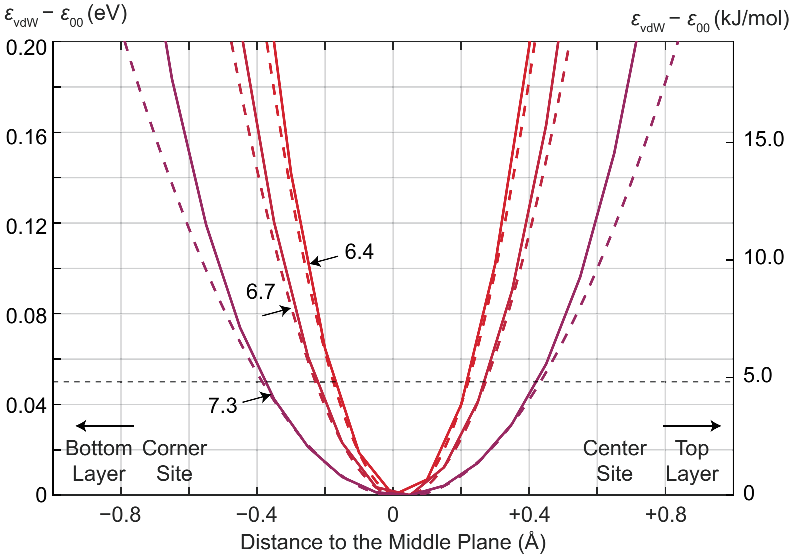

Figure 4.5: Computed van der Waals potential wells subtracting their bottoms $\varepsilon_{\text{vdW}} - \varepsilon_{00}$ for selected layer distances along the dash line in Fig. (4.3). The solid color lines are the results in Fig. (4.4), and the dash color lines are the corresponding fitting results with quadratic functions. The fitting only uses points below 0.05 eV, which are below the dash grey line.

When the layer distance further increases to around 8.4 Å, the bottoms of the potential wells turn obviously flat. Referring to Fig (4.6a), the potentials from two layers are almost linear when the distance to the middle plane ranges from −0.5 Å to +0.5 Å. The overlapping of the linear potentials results in a linear sum in that range. As the potential well of the center site is deeper than the corner site, the linear part slightly tilts toward the top layer direction. With a further increase in the layer distance, the potential turns into the shape of "W" with two energy extrema. These two points correspond to the potential extrema of the two individual layers, as shown in Fig (4.6b). Also, in Fig (4.6), by comparing the potentials with the direct sum of individual potentials, with the layer distance increase, the correlation between the two layers is smaller. At 9.5 Å layer distance, the difference is almost not observable.

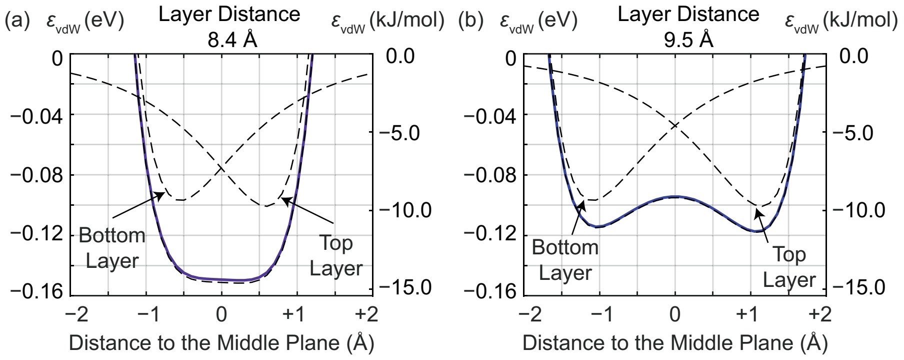

Figure 4.6: Computed vdW potential energies $\varepsilon_{\mathrm{vdW}}$ for (a) 8.4 Å layer distance width and (b) 9.5 Å layer distance. The color lines are from Fig. (4.4). The potentials from individual layers and the sum of the individual potentials are shown with dash black lines.

The minimum energies ε_{00} are given in Fig. (4.7). As the correlation between the two layers is negligible with separations larger than 9.5 Å, the potential is given by the direct sum of the single-layer potentials from Fig. (4.1) for distances larger than 12.0 Å. This ε_{00} has a similar shape to the results in Fig. (4.1). The value decreases quickly as the layer distance increases from 6.0 Å to 7.3 Å. In this region, the position of minimum potential is near the center between the two layers. Then the minimum potential slowly increases to a platform. At large layer separations, the spatial location of the minimum potential is around 3.6 Å to the top layer, corresponding to the potential bottom of the top layer. The final stabilized potential corresponds to the potential bottom in Fig. (4.1a).

4.2.2 Thermodynamic Analysis of Internal Energy of the Pores

Taking the adsorption energy curves in Eq. (2.31), the z direction partition functions from 251 K to 329 K, which is the temperature range of the experiments, are given in Fig. (4.7a). The internal energies corresponding to these partition functions are shown in Fig. (4.7b). These results are given by:

$$u_z = \frac{k_{\mathrm{B}}T^2}{q_z} \cdot \frac{\partial q_z}{\partial T} \approx \frac{k_{\mathrm{B}}T^2}{q_z} \cdot \frac{\delta q_z}{\delta T}. \tag{4.2}$$

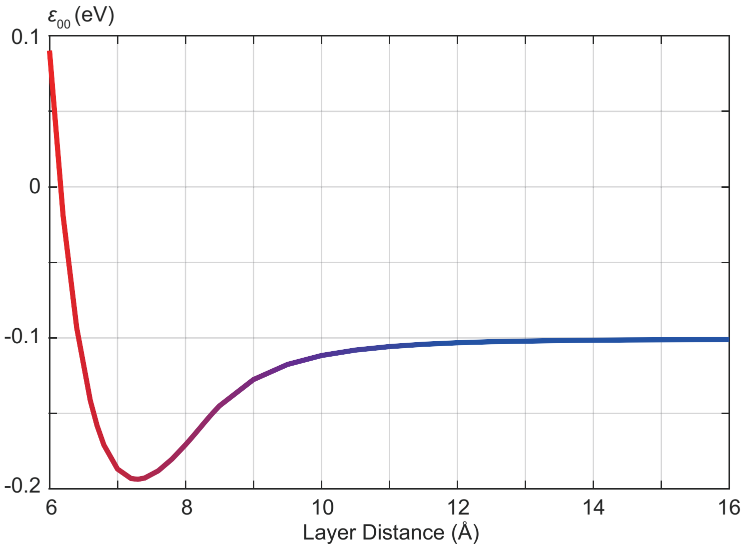

Figure 4.7: The minimum energies ε_{00} of the potentials in Fig. (4.4).

which is shown in Eq. (2.40). A 1 K temperature step is used for δT and δq_z. The corresponding heat capacities are given from the derivatives of the internal energies, and the results are shown in Fig. (4.7c).

In Fig. (4.8a), for small layer distances, the partition functions are small because the potentials increase quickly from the bottom, as the 6.4 Å potential shown in Fig. (4.5). The adsorbed gas molecules are highly likely to locate around the bottoms of the potentials in the temperature region studied in this work. With the increase in layer distance, the potentials increase much slower, and the partition functions increase. For example, for the potential of 8.4 Å shown in Fig. (4.6), the flat potential bottom significantly contributes to the partition function. For the layer distance increases from 8.4 Å, two major changes in the potentials affect the partition function. First, the length of the region between the two energy extrema increases. Second, the energy in the middle part of this region goes up. The former effect raises the partition function, while the latter effect reduces the partition function. From 8.4 Å to 9.0 Å, the former change dominates, and the partition functions continue to increase. From 9.0 Å to 9.5 Å, these two changes evenly compete with each other. In Eq. (2.31), at low temperatures, the partition function is more sensitive to the change in energy, and the partition function decreases as the middle part energy increases. At high temperatures, the partition function is less sensitive to the energy change, but the length of the interval where the integral has large values. Thus, the partition function increases at high temperatures. From 9.5 Å to 12.0 Å, the latter

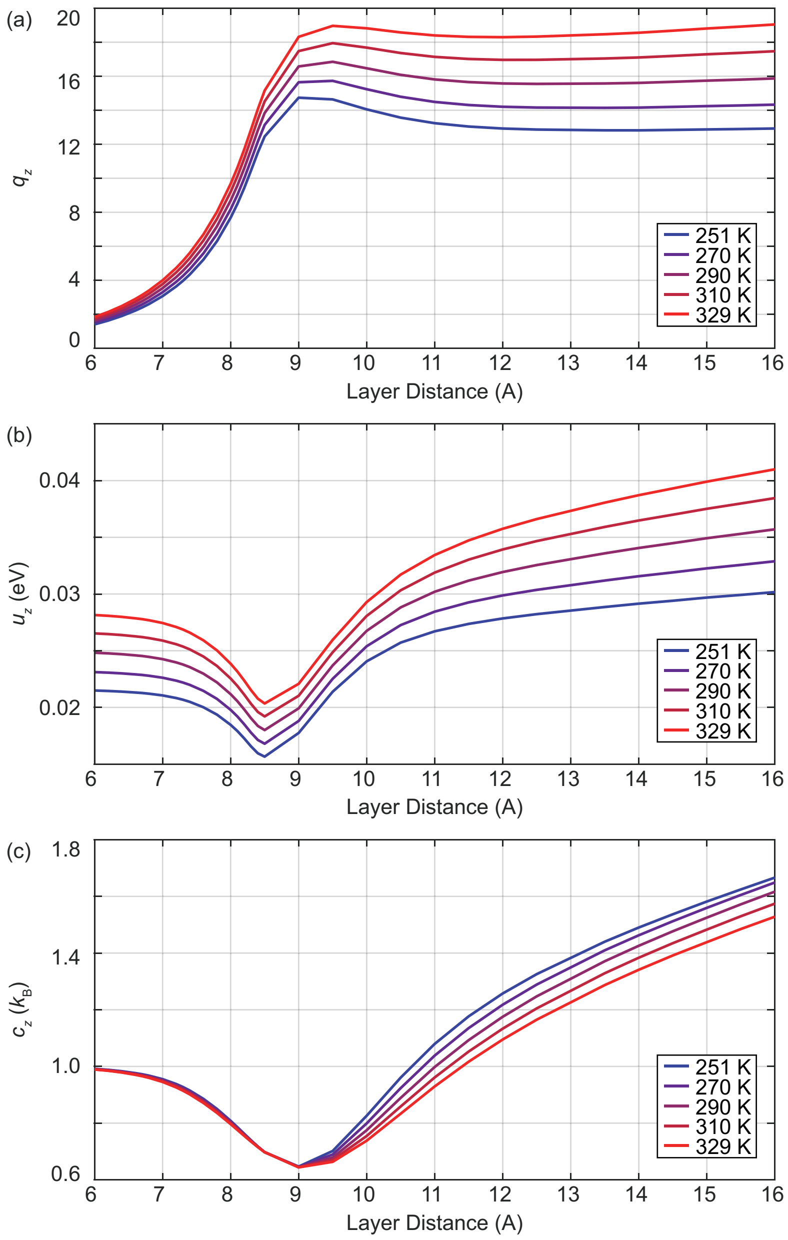

Figure 4.8: Thermodynamic quantities corresponding to the vdW potentials shown in Fig. (4.4) in the classical limit. (a) The partition functions given by the classical limit calculation with potentials subtracting their bottoms, which is shown in Eq. (2.31). (b) The corresponding internal energies of the partition functions given by Eq. (4.2) with $\delta T = 1\,K$. (c) The heat capacities given from the derivatives of the results in (b).

change dominates, and the partition function decreases. With a further increase in temperature, the energy between the energy extrema is close enough to 0, as the two layers are so far from each other. Then the impact of the latter change reaches its maximum, and the impact of the former change suppresses the latter again. But as the potential in this region is much higher than the bottom, the total impact is small and only observable at high temperatures.

For the internal energies, as discussed in Chapter 2, a $0.5k_\mathrm{B}T$ kinetic energy in the z direction comes from the classical limit approximation of the partition function. The rest of the energy comes from the Boltzmann distribution of the potential energy. As a reference, for 251 K, 270 K, 290 K, 310 K, and 329 K, the kinetic energies are 10.81 meV, 11.63 meV, 12.50 meV, 13.36 meV, and 14.18 meV. The internal energies are all much larger than the kinetic part. Typically, at around 6.0 Å, the internal energies are almost exactly double the kinetic energies. With the increase in layer distance to around 8.4 Å, the internal energies decrease to the minimum because the bottom of the potential turns flat. The flat bottom at 8.4 Å has high Boltzmann probabilities and low energies. With the further increase of the layer distance, two energy extrema and the middle potential barrier appear. The middle energy barrier contributes to the internal energy increase.

The $0.5k_\mathrm{B}T$ kinetic energy contribute $0.5k_\mathrm{B}$ to the heat capacity. The heat capacity beyond this comes from the change in potential energy. At 6.0 Å, the internal energy is almost $k_\mathrm{B}T$. Therefore, its heat capacity is k_B. The potential at this layer distance has almost exactly the quadratic form, which corresponds to the harmonic oscillator model. Compared with the results in Chapter 2, the internal energy and the heat capacity of a classical harmonic oscillator are respectively $k_\mathrm{B}T$ and k_B. At around 8.4 Å, the potential with the flat bottom is similar to the square potential, which has only $0.5k_\mathrm{B}$ heat capacity. However, the edges of the potential are less steep than the square potential, and the heat capacity becomes larger. For larger layer distances, with higher temperatures, the Boltzmann probability of the energy barrier between the two energy extrema increases. This increase is faster at lower temperatures due to the form of Boltzmann probability. Therefore, the lower temperature heat capacities are larger than the higher temperature heat capacities. With the increase in layer distance, the energies of the barriers increase, and the energy change for the gas molecule jumping from the bottom to the barrier increases, which also leads to the heat capacities increasing.

4.2.3 Classical Versus Quantum

The results in Fig. (4.8) are all based on the partition functions in the classical limit approximation. A more rigorous way is using the definition of the partition function in Eq. (2.25) and solving the ϵ from the Schrödinger equation Eq. (2.26). The slit-pore model only considers energy change in the z direction. Therefore, the 1D Schrödinger equation given by:

$$\left[-\frac{\hbar^2}{2m}\frac{\partial^2}{\partial z^2}+\varepsilon_{\mathrm{vdW}}(z)\right]\phi(z)=\epsilon\phi(z). \tag{4.3}$$

The z direction partition function is:

$$q_z=\sum\exp\left(-\frac{\epsilon-\varepsilon_{00}}{k_{\mathrm{B}}T}\right), \tag{4.4}$$

while the adsorbed phase partition function q_{ads} is given by Eq. (2.47). In 1D, the eigenstates and the eigenenergies can be numerically solved. For each potential shown in Fig. (4.4), the first 400 eigenenergies are calculated and used for the partition function calculation. The results and corresponding energies and heat capacities are shown in Fig. (4.9).

Compared with the results in Fig. (4.8), the partition functions and the internal energies are almost exactly the same in Fig. (4.9). That means the classical limit calculation of the partition functions is a suitable approximation in the experimental temperature region. For the heat capacity, however, there is a small difference around 6.0 Å. In the quantum case, the heat capacity changes from $0.954k_{\mathrm{B}}T$ to $0.969k_{\mathrm{B}}T$ with the temperature increase. In the classical case, however, the heat capacity is around $0.990k_{\mathrm{B}}T$. There are two reasons behind this effect. First, the heat capacity of the quantum harmonic oscillator is not exactly $k_{\mathrm{B}}T$. Second, the shape of the potential is not exactly a quadratic form.

For the quantum harmonic oscillator approximation, the energy states of the quantum harmonic oscillator are:

$$\epsilon_{\mathrm{QHO},j}=\hbar\omega\left(j+\frac{1}{2}\right), \tag{4.5}$$

where j is the number of states ranging starting from 0. The partition function is then:

$$q_{\mathrm{QHO}}=\sum\exp\left(-\epsilon_{\mathrm{QHO},j}/k_{\mathrm{B}}T\right)=\exp\left(-\frac{1}{2}\cdot\frac{\hbar\omega}{k_{\mathrm{B}}T}\right)/\left[1-\exp\left(-\frac{\hbar\omega}{k_{\mathrm{B}}T}\right)\right]. \tag{4.6}$$

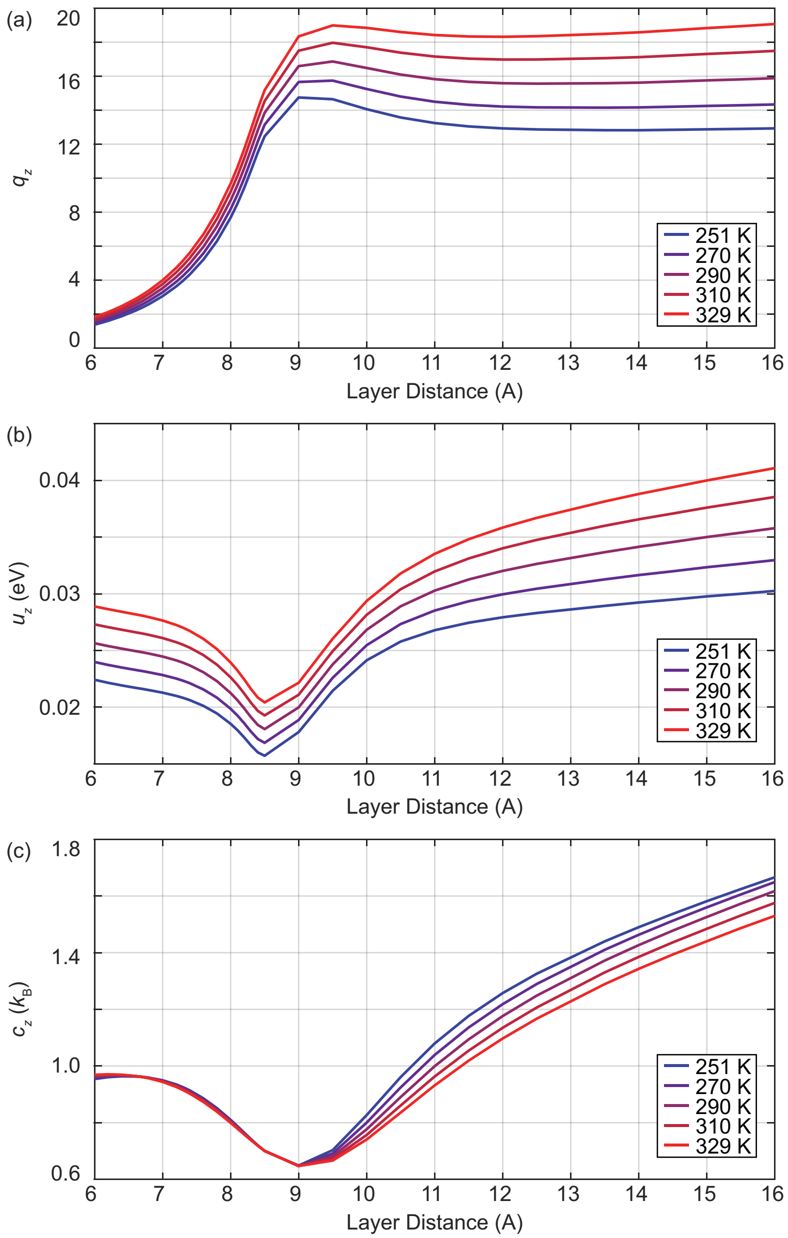

Figure 4.9: Thermodynamic quantities corresponding to the vdW potentials shown in Fig. (4.4) with quantum mechanics. (a) The partition functions given by the calculation with 1D Schrödinger equation, which is shown in Eq. (4.3) and Eq. (4.4). (b) The corresponding internal energies of the partition functions given by Eq. (4.2). The temperature step is 1 K. (c) The heat capacities given from the derivatives of the results in (b).

The internal energy is:

$$u_{\mathrm{QHO}} = \frac{k_{\mathrm{B}}T^2}{q_{\mathrm{QHO}}} \cdot \frac{\partial q_{\mathrm{QHO}}}{\partial T} = \frac{\hbar\omega}{2} + \frac{\hbar\omega}{\exp\left(\hbar\omega/k_{\mathrm{B}}T\right) - 1}. \tag{4.7}$$

The heat capacity is then:

$$c_{\mathrm{QHO}} = \frac{\partial u_{\mathrm{QHO}}}{\partial T} = \left[\frac{\hbar\omega}{\exp(\hbar\omega/k_{\mathrm{B}}T) - 1}\right]^2 \cdot \frac{\exp(\hbar\omega/k_{\mathrm{B}}T)}{k_{\mathrm{B}}T^2}. \tag{4.8}$$

For $k_{\mathrm{B}}T \gg \hbar\omega$, $c_{\mathrm{QHO}} \approx k_{\mathrm{B}}$. For the quadratic fitting of the 6.0 Å potential, the quadratic fitting coefficient is 2.35 eV/Å^2, which corresponds to $\hbar\omega = 15.3$ meV. Taking them into Eq (4.8), the heat capacity is $0.971k_{\mathrm{B}}$, for 251 K and 329 K, the heat capacities are $0.959k_{\mathrm{B}}$ and $0.976k_{\mathrm{B}}$, which corresponds to the heat capacity increase shown in Fig. (4.9c). This quantum effect can also illustrate the difference between Fig. (4.8b) and Fig. (4.9b), at 6.0 Å. In Fig. (4.8b), the internal energy changes from 21.5 meV to 28.2 meV. In Fig. (4.9b), the internal energy changes from 22.4 meV from 28.9 meV. For the quantum harmonic oscillator, the internal energy changes from 22.5 meV to 29.0 meV, which is close to the results in Fig. (4.9b).

For the non-ideal quadratic potential shape, Fig. (4.10a) shows the eigenenergy differences between the two adjacent levels $\epsilon_{j+1} - \epsilon_j$ of the 6.0 Å layer distance. For an ideal quantum harmonic oscillator, this value should be $\hbar\omega$. However, the value in Fig. (4.10a) obviously increases with the index of states. This can illustrate the small differences between the results of the quantum harmonic oscillator and the results in Fig. (4.9).

In quantum language, describing the adsorbed phase for large layer distances is easier. Take 12.0 Å layer distance as an example. Fig. (4.10b) shows its eigenenergies. For the energies less than 0.07 eV, the shape of the curve increases step by step. One step corresponds to two states with similar eigenenergies. This pair of states describe the gas molecule trapped like a harmonic oscillator near the two potential extrema, as shown by the blue curve in Fig. (4.10c). For example, the 2nd energy state belongs to the wave function within the left potential well and has an energy of 5.52 meV. The 3rd energy state belongs to the wave function within the right potential well and has an energy of 5.61 meV. The 4th energy state belongs to the wave function within the left potential well and has an energy of 9.11 meV. The energy difference between the 2nd and 3rd energy states is much lower than that of jumping from the 2nd to the 4th state. Therefore, the step-like increase in Fig. (4.10b) emerges.

When the energy is above 0.07 eV, in Fig. (4.10b), the energy increases more slowly. Therefore the density of energy states is larger, especially for energy states lower than 0.10 eV because the energy state is higher than the potential barrier and then

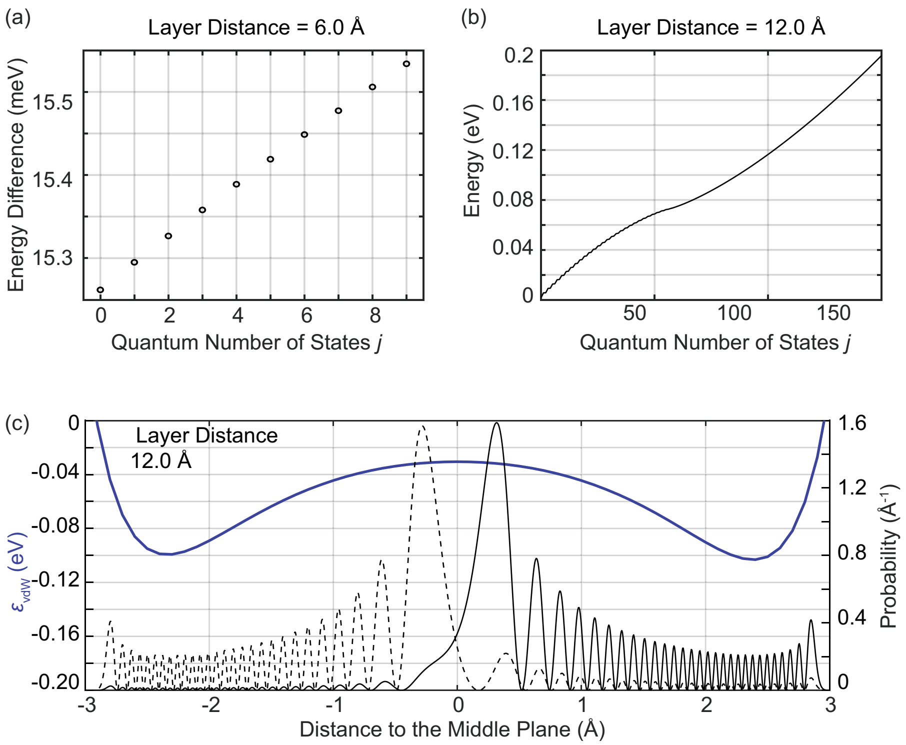

Figure 4.10: Quantum mechanics discussion of several typical layer distances. (a) The eigenenergy differences between the two adjacent levels $\epsilon_{j+1} - \epsilon_j$ of the 6.0 Å potential in Fig. (4.4). (b) The eigenenergies of the 12 Å layer distance. (c) The blue solid line is the 12 Å layer distance potential shown in Fig. (4.4). The black solid line and the black dash line are the probability functions of the 56th state and the 57th state. These states are the first states which overcome the energy barrier between the potential bottoms. These probability functions are given by the square of the wave functions.

the molecule can travel between the potential wells. The black lines show the probability functions of the first two states that can travel between the two wells. As the barrier on the left side is shallower than on the right side, the dashed probability function in the right potential well is higher than the solid probability function in the left potential well. With similar energy, this traveling between the wells provided more possible states for the molecule other than trapped inside the individual wells. Therefore, there are more states in this energy range.

At lower temperatures, the krypton molecule mostly occupies the lower energy states. At higher temperatures, the gas molecule can occupy the higher energy states, but the increase in state energies is smaller. Therefore, the heat capacity is smaller at higher temperatures.

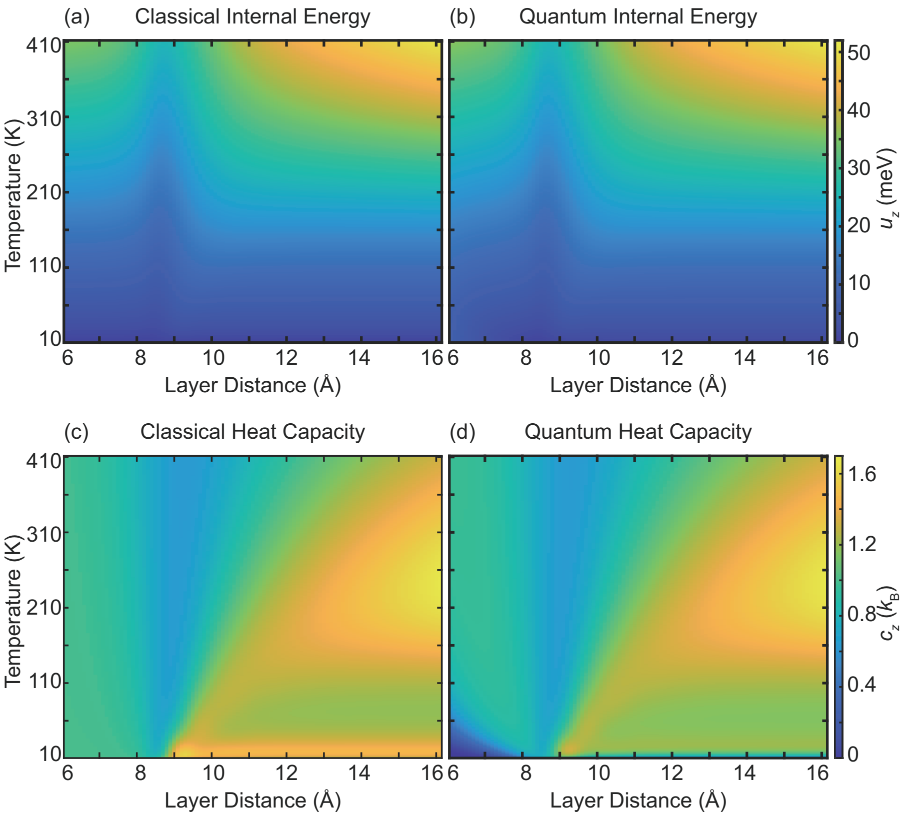

Figure 4.11: Comparison between quantum mechanics and classical limit approximation. (a)(b) The z direction internal energies. (c)(d) The z direction heat capacities. (a)(c) The results with the classical limit approximation. (b)(d) The results given by solving the Schrödinger equation.

For a further comparison between the classical and quantum theories, the calculations were performed with a larger temperature range from 10 K to 410 K. The results are shown in Fig. (4.11). The differences are only observable for small layer distances or low temperatures. For example, a near-zero heat capacity is observed at around 6.0 Å at 10 K. This can be illustrated by Eq. (4.8) where $\hbar\omega$ is much larger than $k_\mathrm{B}T$. Also at 10 K, the heat capacities are around k_B for larger layer distances like 12.0 Å, because the gas molecules get trapped in the potential wells shown in Fig. (4.11c), and act like quantum harmonic oscillators with a smaller $\hbar\omega$. As mentioned, the $\hbar\omega$ results for 6.0 Å and 12.0 Å are respectively 15.3 meV and 9.6 meV. However, for the temperature studied in this work, which ranges from 250 K to 330 K, it is proper to use the classical limit approximation.

4.2.4 2D Ideal Gas Versus Non-Ideal Gas

In the slit-pore model discussed above, the potential along the dashed line in Fig. (4.3) is considered homogeneous along the surface. However, it is also shown in Table (4.1) that the center sites and corner sites have a 0.05 eV energy difference. Compared with the $k_{\mathrm{B}}T$ at 300 K, which is around 0.025 eV, this energy difference is not small. Therefore, using the 2D ideal gas model and the potential shown in Fig. (4.4) needs further discussion.

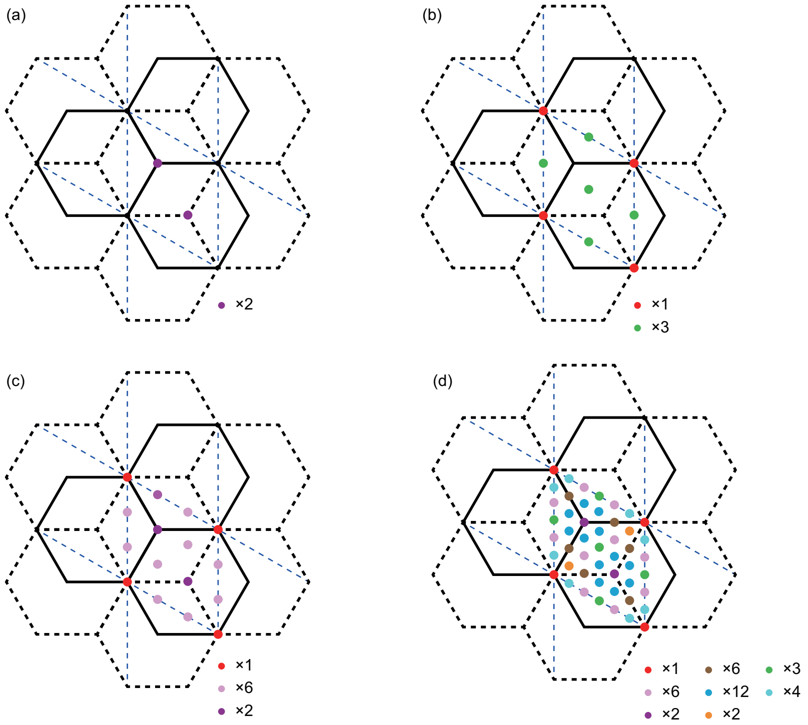

Figure 4.12: Top view illustration of the structure shown in Fig. (4.3). The color dots are the lines picked for the 2D non-ideal gas model. The solid black lines and dash black lines show the two different carbon planes. The blue dash lines show the edge of the unit cells along the $x - y$ plane. The dash line in Fig. (4.3) is shown in (a) with the purple dot, which connects one center site and one corner site. (b), (c) and (d) show different choices of lines. The color of dots in (d), from top to bottom and from left to right, are named red, pink, purple, brown, blue, orange, green, and cyan. The numbers of dots in one unit cell are also shown.

The previous subsection pointed out that even for the large potential change, like the potential for 6.4 Å layer distance, it is still proper to use classical limit approximation to calculate the partition function in the temperature range studied experimentally. The later discussion will continue from the classical partition function expression Eq. (2.30) and the multi-site calculation Eq. (2.56). When the total number of i is large enough, Eq. (2.56) can be considered the integral along the successive plane. Therefore, multiple lines similar to the dash line in Fig. (4.3) are picked to calculate the $\varepsilon_{\mathrm{vdW},i}$. The choice of lines are shown in Fig. (4.12), and the corresponding vdW potentials are shown in Fig. (4.13).

Evidently, the potentials in Fig. (4.13) have no significant differences. The most observable difference comes from the potential of 6.2 Å. For the purple one in Fig. (4.13c), this 6.2 Å potential goes deepest, while for the red and cyan lines in Fig. (4.13a) and (4.13h), the 6.2 Å potentials are almost above 0. Another difference is the potential of 12.0 Å. For the purple line potential in Fig. (4.13c), the depth of the two wells has a slight difference, as described before. For other potentials, however, the difference is almost indistinguishable.

For a certain layer distance D, with this series of $\varepsilon_{\mathrm{vdW},i,D}$ and the multi-site adsorption theory Eq. (2.56), the total partition function is:

$$q_{\mathrm{ads}} = \frac{A}{\Lambda^3} \sum \alpha_i \int_{-D/2}^{+D/2} \exp\left(-\frac{\varepsilon_{\mathrm{vdW},i,D}}{k_{\mathrm{B}}T}\right) \mathrm{d}z. \tag{4.9}$$

Here, the origin of the z direction is the middle between the planes. The internal energies and corresponding heat capacities of the adsorbed phase are calculated from this partition function. In Fig. (4.12b), (4.12b), and (4.12d), the cells are evenly divided into 4, 9, and 36 parts. The α_i terms are given by the geometry shown in these figures.

Fig. (4.14a) corresponds to the results in Fig. (4.8b) adding the ε_{00} in Fig.(4.7). As ε_{00} does not change with temperature, the corresponding heat capacity is the same as Fig. (4.8c). In Fig. (4.14c) to (4.14g), the biggest differences are around 6.2 Å, as the potential has the biggest differences with this layer distance. For most of the results in Fig. (4.13), the potentials around 6.2 Å are higher than Fig. (4.13c). Therefore, the thermally averaged potentials become larger. Also, the ε_{00} terms are no longer unique. Along the $x-y$ plane, the potential changes from a delta function to periodic functions. As discussed, the delta function has the smallest heat capacity. Thus, the heat capacities around 6.2 Å become larger. With increasing temperature, the thermally average effect is more important, and therefore the changes in heat capacities are smaller. For large layer distances, most of the potentials in Fig. (4.14) have shallower potential wells than the right one in Fig. (4.14c), but these potential wells are deeper than the left one in Fig. (4.14c). However, as the differences are small, the changes in internal energies and heat capacities are also small.

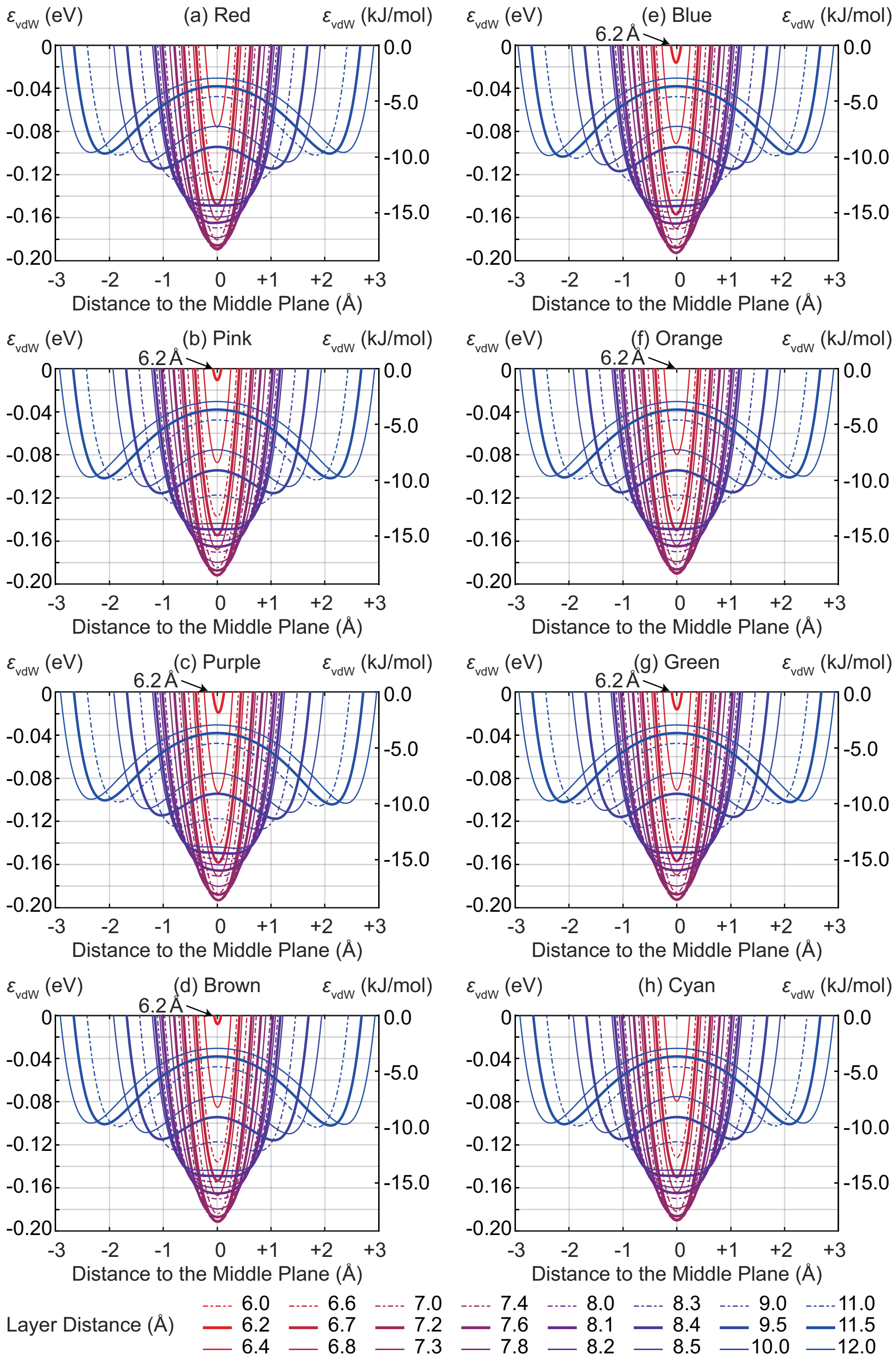

Figure 4.13: Smooth fitting of the computed vdW potential energies $\varepsilon_{\mathrm{vdW}}$ for selected layer distances along the different lines in Fig. (4.12). The interval of the initial potential is 0.1 Å, and the interval of the fitting is 0.025 Å. Different types of lines are used for distinguishing.

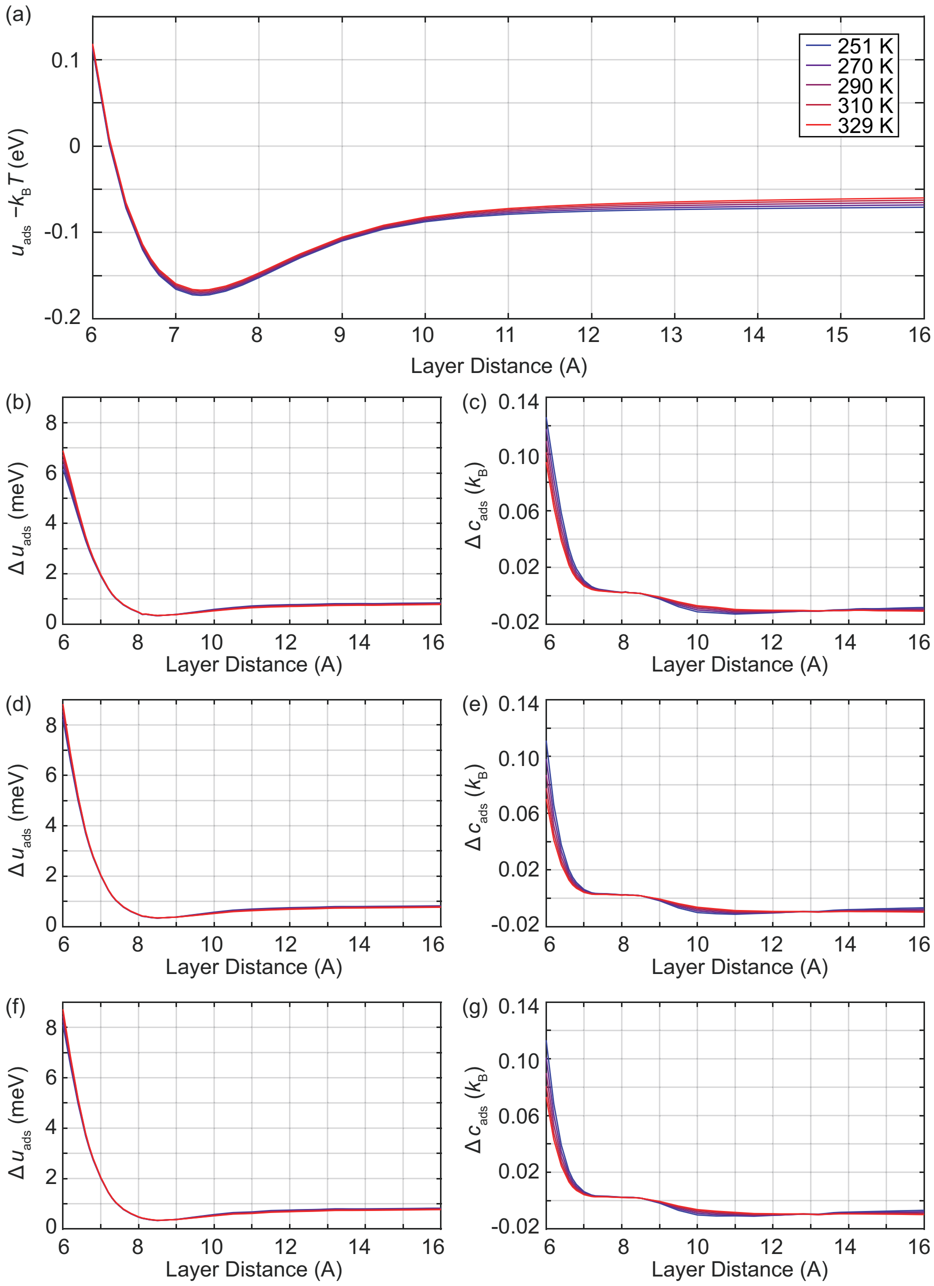

Figure 4.14: Thermodynamic analysis of the structures in Fig. (4.12). (a) The results of the structure in Fig. (4.3) or Fig. (4.12a). The u_{ads} is the adsorbed phase internal energy while the $k_{\mathrm{B}}T$ corresponds to the $x-y$ kinetic energy. (b)(c) Results correspond to Fig. (4.12b). (d)(e) Results correspond to Fig. (4.12c). (f)(g) Results correspond to Fig. (4.12d). (b),(d) and (f) show the internal energies subtracting the energies of reference in (a). (c), (e) and (g) show the heat capacities subtracting the results in Fig. (4.8c). The legends of all figures are the same as shown in (a).

According to the results in Fig. (4.14), the largest difference in the adsorption energies and heat capacities is less than 10%. Also, according to Fig.(4.7), the largest changes occur for the energetically less favorable layer distances. The differences are negligible for layer distances larger than 7.0 Å. Therefore, using only the results in Fig.(4.4) for a 2D ideal gas model is proper.

4.2.5 Two Layers Versus Four Layers

In the previous discussions, the krypton molecule is put between two layers of carbon. However, the volume outside the pores is not a vacuum for real materials. Multiple layers are also considered for slit-pore models shown in Fig. (2.2). Therefore, two extra layers of carbon were introduced into computation as a comparison, and the new model is shown in Fig. (4.15a). The distances between the layers on the same side of the krypton are $D_\mathrm{b} = 3.325$ Å, which are the same as the model in Fig. (4.2). Similar to the calculation before, the vdW potential along the dash line is shown in Fig. (4.15b).

Compared with Fig. (4.4), the shapes of the potentials are almost similar. The major difference is that the potentials are deeper because of the vdW potential from the two extra layers. The vdW potentials in Fig. (4.15b) are close to the sum of potentials of two double layers with the layer distances of D and $D + 2D_\mathrm{b}$, while $2D_\mathrm{b}$ is a large distance. Take $D = 6.2$ Å layer distance as an example, the $D+2D_\mathrm{b}$ is nearly 12.9 Å. The potential of 12.9 Å layer distance is weak in the middle part between the two inner layers, where the 6.2 Å layer distance has the strongest potential. Similarly, for layer distances ranging from 6.2 Å to around 8.0 Å, the deepest parts of the potentials are the parts near the middle plane, while the contributions from the outer layers to the total potentials are weaker and weaker with the layer distance increase. For large layer distance, however, the deepest parts of the potential are around 3.4 Å away from one inner layer. The changes in the potential bottoms are then approximately always adding the potential 6.8 Å away from one outer layer.

Based on the results in Fig. (4.15b), the z direction internal energies and heat capacities are also calculated with Eq. (4.2) and corresponding derivatives, and the results are shown in Fig. (4.15c) and Fig. (4.15d). The results are similar compared with Fig. (4.8). The most significant difference is for large layer distances, where the internal energies slightly turn smaller.

Therefore, it can be concluded that compared with two layers, the multiple layers slit-pore model has differences in the vdW potential, which comes from the potential

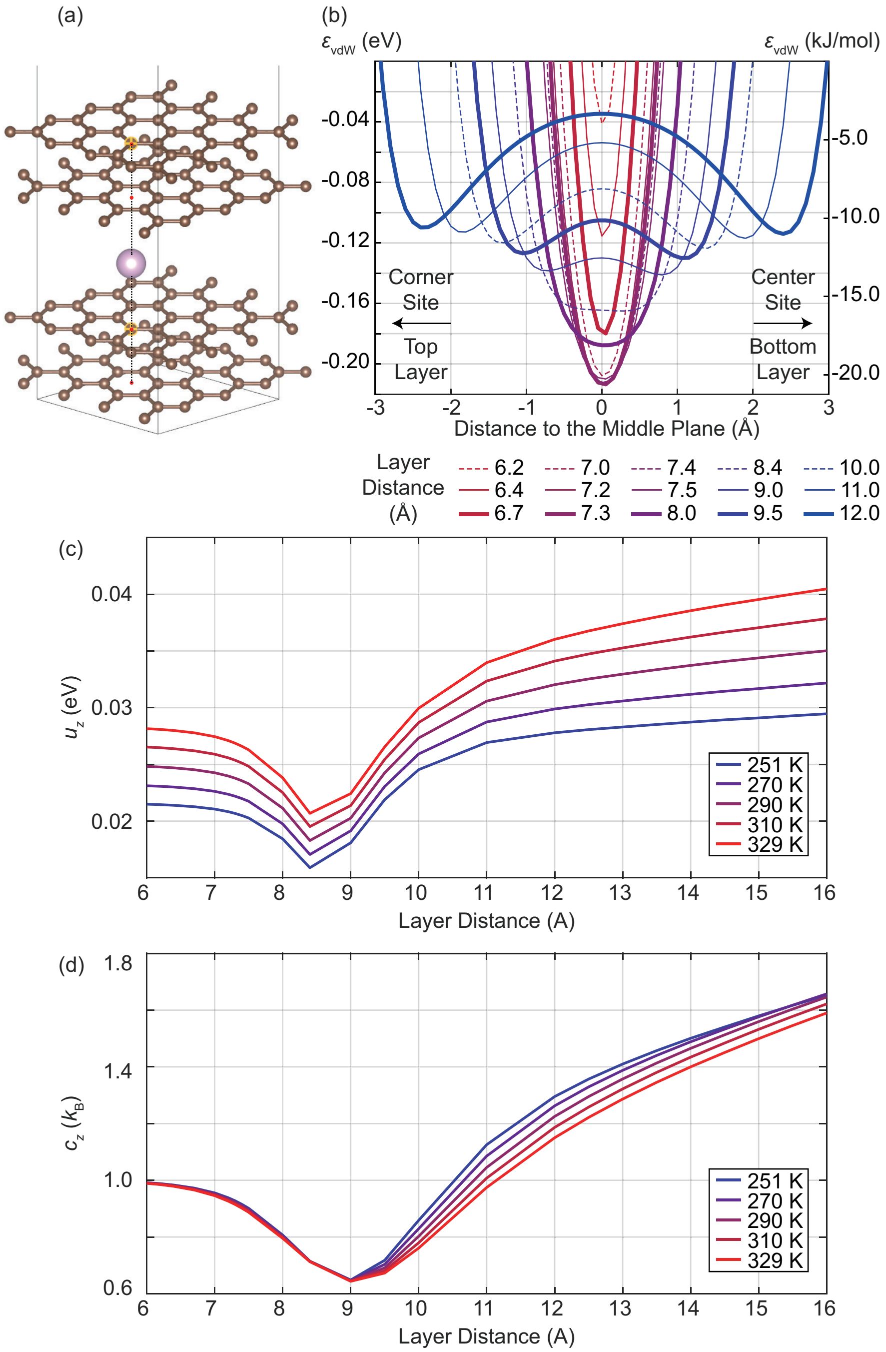

Figure 4.15: Computation model and results of a krypton atom with two layers of carbon on both the top and the bottom sides. (a) The structure of the model. (b) The computed potential energies $\varepsilon_{\mathrm{vdW}}$ for selected layer distances along the different lines in Fig. (a) Different types of lines are used for distinguishing. (c) The corresponding internal energies of the partition functions given by Eq. (4.2). The temperature step is 1 K. (d) The heat capacities given from the derivatives of the results in (c).

from outer layers. These differences in potentials are the same as the differences in internal energies. However, for the temperature dependence of the internal energies and the heat capacities, the differences between two and multiple layers are insignificant.

4.3 Thermal Vibration

Previous sections assume that the shapes of potentials do not change with temperature. However, the displacements caused by thermal vibration can change the location of the adsorbent, and the vdW potentials are then altered. For the 2D ideal gas model, the ε_{00} in the single particle partition function Eq. (2.47) is also temperature dependent. The adsorbed phase internal energy is then:

$$u_{\mathrm{ads}} = \varepsilon_{00} - T\,\frac{\partial \varepsilon_{00}}{\partial T} + \frac{k_{\mathrm{B}}T^2}{q_z}\frac{\partial q_z}{\partial T} + k_{\mathrm{B}}T. \tag{4.10}$$

Compared with the energy in Eq. (2.52), the second term $T\partial\varepsilon_{00}/\partial T$ emerges. When considering the heat capacity, it turns into:

$$c_{\mathrm{ads}} = -T\,\frac{\partial^2 \varepsilon_{00}}{\partial T^2} + \frac{\partial}{\partial T}\left(\frac{k_{\mathrm{B}}T^2}{q_z}\frac{\partial q_z}{\partial T}\right) + k_{\mathrm{B}}. \tag{4.11}$$

The extra term $\partial^2\varepsilon_{00}/\partial T^2$ has to be considered if the potentials are temperature dependent.

4.3.1 Simulation with TDEP Method

The stochastic Temperature Dependent Effective Potential (TDEP) method simulates the thermal vibration of the adsorbent. Developed by Olle Hellman and Nina Shulumba, this software package can calculate the force constants between atoms from the energy of displaced systems (Hellman, Abrikosov, and Simak, 2011; Hellman and Abrikosov, 2013; Hellman, Steneteg, et al., 2013). Multiple equal-probability thermally displaced configurations can then be generated from the force constants. Similar to the Born–Oppenheimer approximation, the thermal vibration of the adsorbent atoms is much faster than the translation of the adsorbate molecules. Therefore, the adsorbate molecules can only feel a time-averaged vdW potential field. According to the Monte Carlo calculation, this average potential field is simulated by averaging the potentials of multiple thermally displaced configurations.

Fig. (4.16) shows the process of thermally displacement simulation. The $3 \times 3 \times 2$ bulk graphite cell with 72 carbon atoms is initially picked. Then with the TDEP package, multiple thermally displaced configurations at different temperatures are generated. Next, two layers of carbon are extracted from the bulk cell and separated with layer distances of 6.4 Å, 6.7 Å, 7.3 Å, 8.4 Å, and 9.5 Å. One krypton molecule is put between these two layers, and a large vacuum space is added to avoid the influence of adjacent cells. The vdW potential is calculated along the dash line, and the final vdW potential is given by averaging 50 different configurations.

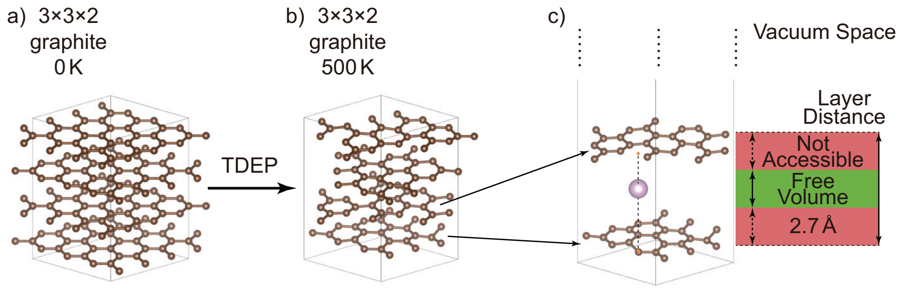

Figure 4.16: Illustration of the generation process of thermally displaced configurations. (a) The $3 \times 3 \times 2$ graphite cell without thermal displacement. (b) One simulated thermally displaced configuration of the cell at 500 K. (c) One system used for the vdW potential calculation. The double-layer structure is similar to Fig. (4.3), and the dash line is the same. However, the carbon atoms are thermally displaced in this system.

As the phonon describes the vibration, the accuracy of the TDEP thermally displacement simulation is checked by comparing the phonon dispersion relationship by TDEP and experiments (Wirtz and Rubio, 2004; Maultzsch et al., 2004; Mohr et al., 2007). The comparison is shown in Fig. (4.17). Compared with the experiments, the simulated phonon dispersion relationship is accurate enough, which means the simulation of the thermally displaced configurations is valid.

4.3.2 Monte Carlo Calculation

The Monte Carlo calculation results are shown in Fig. (4.18). For small layer distances like 6.4 Å, with the temperature increase, the vdW potentials turn weaker. However, the shapes of the potentials do not change too much. For the large layer distances like 9.5 Å, the shapes of potentials change little with temperature increase. Therefore, it can be approximated that the $\varepsilon_{\mathrm{vdW}} - \varepsilon_{00}$ in q_z expressed in Eq. (2.31) is temperature independent. In Eq. (4.10) and Eq. (4.11), only the ε_{00} parts need consideration.

The ε_{00} results are shown in Fig. (4.19). For small layer distances, with the temperature increase, the minimum of the vdW potential wells turns smaller in magnitude. For large layer distances, the minimum potential energies hardly change. The slopes

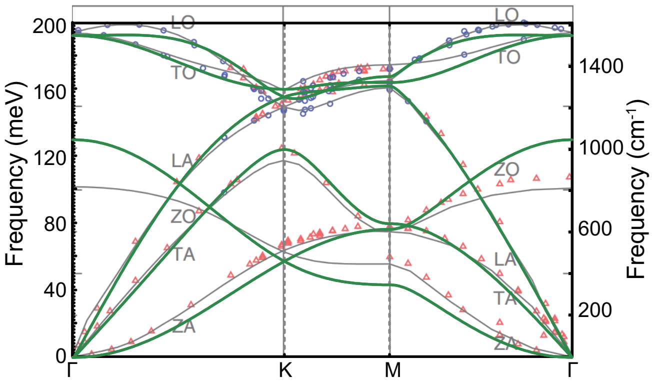

Figure 4.17: The green lines are the phonon dispersion relationship of graphite calculated by the sTDEP method. The background is reference data adopted from the cited paper (Mohr et al., 2007). The red triangles and blue circles are inelastic X-ray scattering experiment results. The solid lines are reference calculation results.

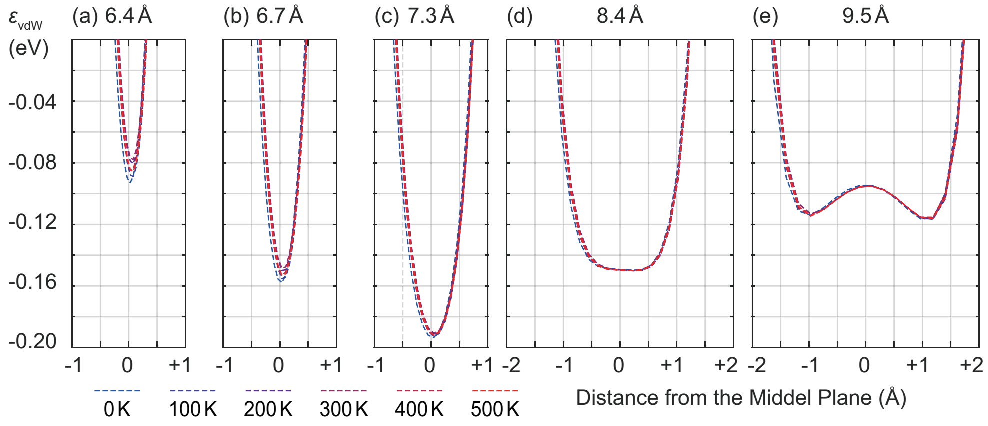

Figure 4.18: The MC calculation results of krypton adsorption potentials between two thermally displaced carbon layers.

of the linear fittings for layer distance from small to large are $0.168k_{\mathrm{B}}$, $0.104k_{\mathrm{B}}$, $0.030k_{\mathrm{B}}$, $-0.004k_{\mathrm{B}}$, and $0.020k_{\mathrm{B}}$. These changes are all much smaller than ε_{00}. Also, linear temperature dependences are canceled out by the first two terms in Eq. (4.10). Meanwhile, no distinct second-order temperature dependence is shown in Fig. (4.19). Thus, thermal vibration has no major impact on the adsorbed phase's internal energy and heat capacity.

Although Monte Carlo calculation shows that thermal vibration does not impact the heat capacity, some results still deserve discussion. In Fig. (4.18), for all the layer distances, with the temperature increase, the changes in adsorption potentials are

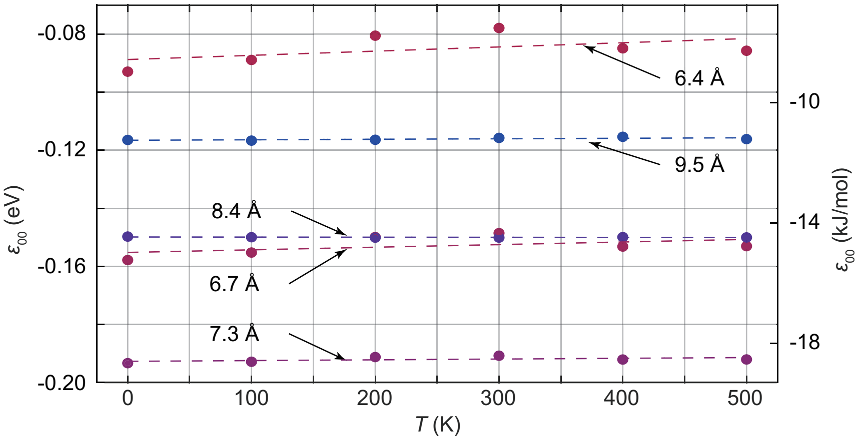

Figure 4.19: Bottoms of the vdW potentials ε_{00} by MC calculation for selected layer distances at different temperatures. The dash lines are linear fits.

less distinct on the center site (right side). It is because six carbon atoms equally contribute the potential on the center site, and it is less possible for them to have a homogeneous trend. For the potentials on the corner site (left side), however, they show observable weakening because the potential is highly affected by the vibration of the most adjacent carbon atom.

In Fig. (4.19), the temperature dependence of the ε_{00} is initially large with small layer distances. With the layer distances increase, the temperature dependence turns smaller and then becomes slightly larger. This trend can be illustrated with an LJ potential analysis. Assuming the vdW potential has an LJ form in Eq. (1.1), then the time-averaged adsorption energy $\overline{\varepsilon}_{\mathrm{LJ}}$ can be expressed as:

$$\overline{\varepsilon}_{\mathrm{LJ}}(R) = \left[\, \varepsilon_{\mathrm{LJ}}(R + \Delta R) + \varepsilon_{\mathrm{LJ}}(R - \Delta R)\right] /2, \tag{4.12}$$

where ΔR is an average deviation caused by the vibration of the adsorbent atom. By assuming ΔR is much smaller than R and doing second-order Taylor expansions of Eq. (4.12), the change in vdW potential caused by the thermal vibration is:

$$\Delta\overline{\varepsilon}_{\mathrm{LJ}}(R) = -4\varepsilon_0 \left[78\left(\frac{\sigma}{R}\right)^{12} - 21\left(\frac{\sigma}{R}\right)^{6}\right]\left(\frac{\Delta R}{R}\right)^{2}, \tag{4.13}$$

where $\Delta\overline{\varepsilon}_{\mathrm{LJ}} = \overline{\varepsilon}_{\mathrm{LJ}} - \varepsilon_{\mathrm{LJ}}$.

Compared with Eq. (1.1), the terms in the square bracket amplify the repulsive potential more than the attractive potential. When $R = \sigma$ and $R = 2^{1/6} \cdot \sigma$, $\Delta\overline{\varepsilon}_{\mathrm{LJ}}$ is $-228\,\varepsilon_0 \cdot (\Delta R/\sigma)^2$ and $-28.6\,\varepsilon_0 \cdot (\Delta R/\sigma)^2$, which are all repulsive. Only when

$R > 1.24\,\sigma$, $\Delta\bar{\varepsilon}_{\mathrm{LJ}}$ turns attractive. This $\Delta\bar{\varepsilon}_{\mathrm{LJ}}$ reaches extrema $2.97\,\varepsilon_0 \cdot (\Delta R/\sigma)^2$ when $R = 1.37\,\sigma$, which is small compared with the repulsive potential mentioned before.

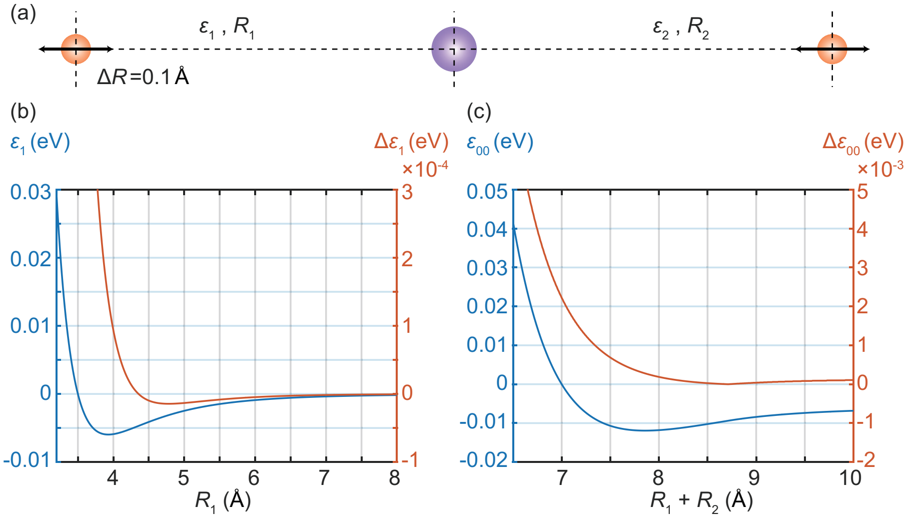

Figure 4.20: Calculation of the thermal displacement impact with LJ potential. (a) The model used for the LJ potential calculation. The orange atoms are carbon and the purple atom is krypton. (b) The blue line with the left axis shows the LJ potential from the left carbon atom. The orange line with the right axis shows the LJ potential change due to the ΔR displacement. (c) The blue line with the left axis shows the LJ potential minima versus the distance between the two carbon atoms. The orange line with the right axis shows the corresponding potential change due to the ΔR displacements.

The calculation above discusses the situation with only two atoms. To illustrate the slit-pore model results shown in Fig. (4.19), the model with a krypton molecule between two carbon atoms is calculated, as shown in Fig. (4.20a). The two carbon atoms are separated for distances from 6.0 Å to 10.0 Å. For the krypton interaction with one carbon atom, the potential given by Eq. (1.1) is shown with the blue line and left axis in Fig. (4.20b). The constants in Eq. (1.1) are: $\varepsilon_0 = 5.96\,\mathrm{meV}$ and $\sigma = 3.5$ Å (Maiga and Gatica, 2018). Meanwhile, The orange line and the right axis in Fig. (4.20b) describe the change in LJ potential shown in Eq. (4.13). The ΔR is set as 0.1 Å.

The total potential is the sum of two krypton-carbon LJ potentials. In Fig. (4.20c), the blue curve shows the potential minima ε_{00} for different layer distances. The lowest point of the blue curve is 11.92 meV, when the distance is 7.86 Å. At this point, the distances between the krypton and the two carbons are both $2^{1/6}\sigma = 3.93$Å. Similar to the results in Fig. (4.4), when the distance between the two carbons is smaller than 7.86 Å the location where the krypton can find the lowest potential energy is in the middle between the carbons. When the distance is much larger than 7.86 Å the location of the lowest potential is $2^{1/6}\sigma = 3.93$ Å to the carbon.

The impact of thermal vibration on the potential minima ε_{00} is shown in Fig. (4.20c) with the orange line. With the increase in carbon distance, the $\Delta\varepsilon_{00}$ initially decreases and reaches the minimum when the distance is 8.72 Å. Then the value increases again, but for a smaller magnitude. This is due to the change in the location of the potential minima away from the center between carbon atoms. The trend shown by this orange line corresponds to the Monte Carlo calculation results in Fig. (4.19), where the slopes of linear fits decrease first and then increase slightly with the layer distance increase.

4.3.3 Impact of vdW Potentials on Thermal Vibration

In the previous discussion in this section, the vdW potential is approximated to have no impact on thermal vibration. However, this assumption requires validation. According to the references, the phonon dispersion relationships of graphene and graphite are similar, including in the out-of-plane z direction. Apart from this indirect evidence, the calculation with LJ potential can further prove the applicability of this approximation.

Using the Einstein solid model and referring to the "ZO" mode frequency in Fig. (4.17), the carbon atoms can be initially regarded as a harmonic oscillator with $\hbar\omega = 100$ meV. The ground state probability function is a Gaussian function with a height of 9.56 Å^{-1} and a standard deviation of 0.022 Å. As $\hbar\omega$ is large energy compared with room temperature $k_\text{B}T$, the thermal averaged probability functions have no significant deviation from the ground state probability function.

The model with one carbon atom and one krypton molecule is then analyzed. However, the ΔR is no longer used to describe the carbon displacement. On the contrary, the probability function given by the Schrödinger equation describes the thermal displacement of the carbon atom. With the krypton molecule taken into consideration, the vdW potential is also included in the Schrödinger equation.

Compared with the original harmonic oscillator results, The probability and vdW potential changes are shown in Fig. (4.21), where the distances between the carbon atom and the krypton molecule are selected as 3.0 Å, 3.5 Å, 3.93 Å, and 4.0 Å. These atom distances represent the situation with a strong repulsive potential, zero potential, maximum adsorption potential, and a weaker adsorption potential. For $R = 3.0$ Å, in Fig. (4.21a), the change in probability function is on the same order of magnitude as the initial ground state probability function. For all the temperatures, the two atoms significantly move further due to the high repulsive potential shown in Fig. (4.21b). Without considering the impact of vdW potential on thermal vibration, the energy increase around 93.6 meV, which is comparable to the $\hbar\omega$ and much larger than $k_\mathrm{B}T$. However, considering the impact of vdW potential, the interaction energy turns more than 6 meV smaller. For $R = 3.5$ Å, the LJ potential should be 0 if the carbon atom is regarded as a static point. However, the thermal vibration increases the vdW potential without considering the impact of vdW potential, as shown in Fig. (4.20b). With the vdW potential impact, the interaction energy decreases for 0.06 meV. However, the change in probability function shown in Fig. (4.21c) is an order of magnitude smaller than in (4.21a). For $R = 3.93$ Å, in Fig. (4.20b), the vdW interaction reaches the minimum. The probability function narrows to the center, and the vdW energy decreases slightly. However, the change in probability function is three orders of magnitude lower than Fig. (4.21a). For $R = 4.0$ Å, the atoms tend to move closer to each other, but this change in probability function is also tiny. The decrease in vdW potential is around 10^{-3} meV, which is only around 0.017% change.

In summary, vdW interaction leads the vibration to lower energy. However, this impact is significant only when the atoms are very close, and the repulsive potential is substantial. However, these distances are energetically less favorable. Thus it is appropriate to assume the vdW potential does not impact the thermal vibration and use the bulk graphite thermal displacements for the slit-pore model analysis. Another phenomenon in Fig. (4.21b), (4.21d), (4.21f) and (4.21h) is that the vdW potential has no significant second-order temperature dependence, which validates the previous conclusion that thermal vibration has no major impact on the internal energy and heat capacity of the adsorbed phase.

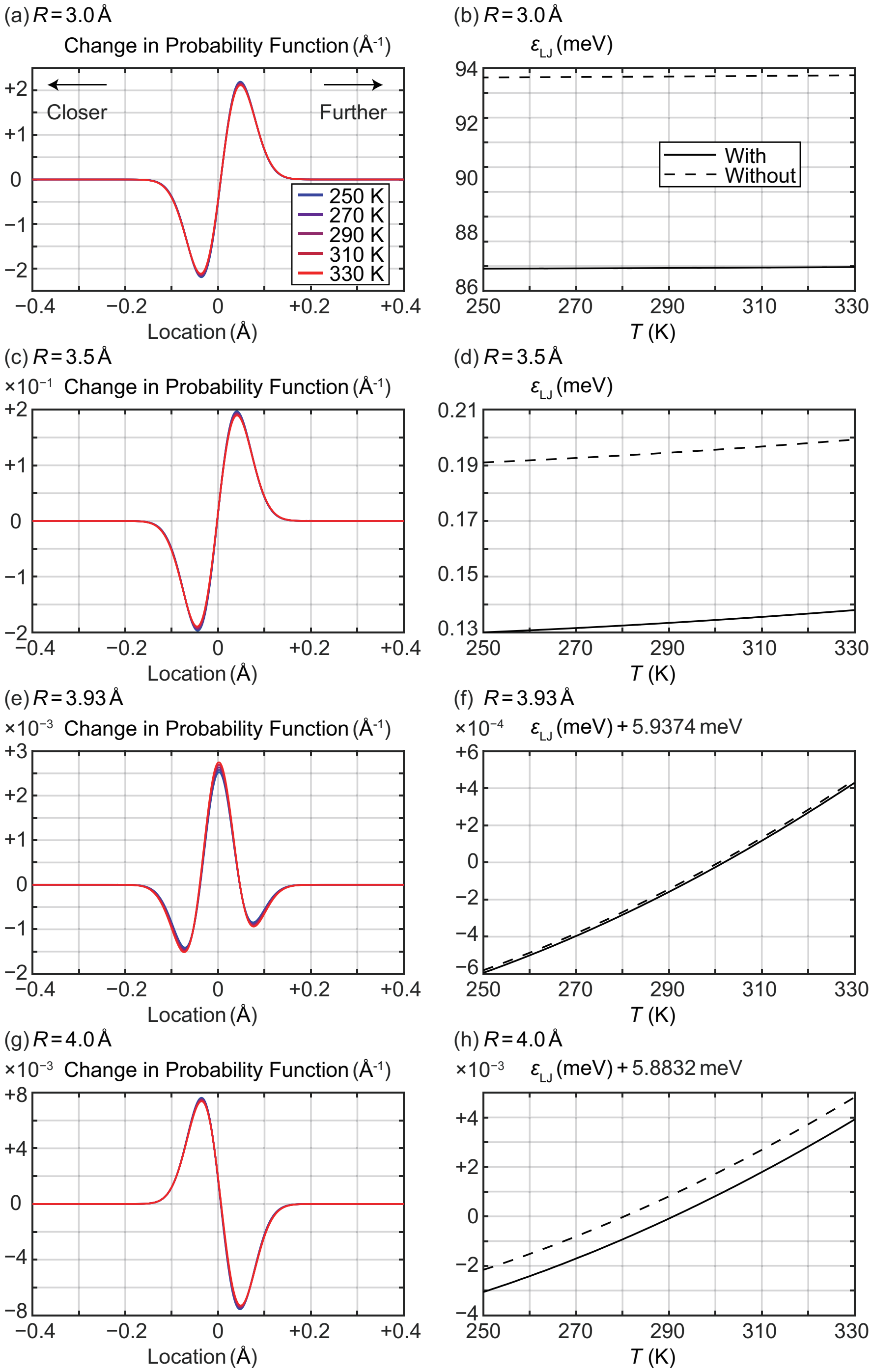

Figure 4.21: The impact of vdW potential on thermal vibration. Left: The changes in probability functions caused by the vdW potential compared with the original harmonic oscillator model. Right: The vdW potentials of a krypton atom and a thermally vibrating carbon atom. The dash lines represent the vibration not affected by the vdW potential. The solid lines represent the vibration under the impact of the vdW potential.

Chapter 5

DISCUSSION ON THE TEMPERATURE DEPENDENCE OF ADSORPTION ENERGY

The third chapter of this work investigates the temperature dependence of krypton adsorption energy and the heat capacity of the adsorbed phase. Experimental observations have shown that the adsorption energy of krypton exhibits a significant temperature dependence, while the adsorbed phase has a large heat capacity. This chapter explains the observed temperature dependence using theoretical, experimental, and computational results from the second, third, and fourth chapters.

5.1 Boltzmann Effects

In Chapter 2, the multi-site adsorption theory is discussed. Pores with different sizes can be regarded as different sites, and the α_i can be calculated from the NLDFT surface area density in Fig. (3.3). Meanwhile, their partition functions, internal energies, and heat capacities are shown in Fig. (4.8). These results are taken into equations from Eq. (2.53) to Eq. (2.57), and selected results are shown in the following figures.

Fig. (5.1a) and (5.1b) show the densities of Henry's constant for two materials, which are the continuous function form of the $K_{\mathrm{H},i}$ in Eq. (2.54). The integrals of these functions are the total K_{H} at different temperatures. These results show that Henry's constants decrease quickly with temperature. By substituting Henry's constants into Eq. (2.12) or directly using Eq. (2.57), the isosteric adsorption energies are given in Fig. (5.2).

In Fig. (5.2), the isosteric adsorption energy of MSC-30 changes from -0.101 eV to -0.087 eV from 250 K to 330 K, and the slope is $2.03k_{\mathrm{B}}$. For CNS-201, the change in adsorption energy is from -0.090 eV to -0.086 eV, and the slope is $0.62k_{\mathrm{B}}$. Both results clearly show that with increasing temperature, the magnitude of adsorption energy decreases almost linearly. The experimental results analyzed by Henry's law and the Langmuir model are also shown as references. The slopes of these results are compared in Table (5.1).

The reason for these changes in adsorption energy are suggested by Fig. (5.3). For CNS-201, referring to the results in Fig. (4.8c), the first peak of the surface area distribution around 10.6 Å corresponds to an adsorption energy changing rate around $0.4k_\mathrm{B}$, which is smaller than the $0.62k_\mathrm{B}$ in Fig. (5.2). The second peak around 12.1 Å has an around $0.7k_\mathrm{B}$ adsorption energy changing rate, contributing to the increase in energy change. Additionally, with increasing temperature, the gas distribution shifts slightly from the first peak to the second peak, while the two peaks with lower surface area distributions at around 15.5 Å and 17.9 Å also attract more gas. These larger pores have higher heat capacities and internal energies.

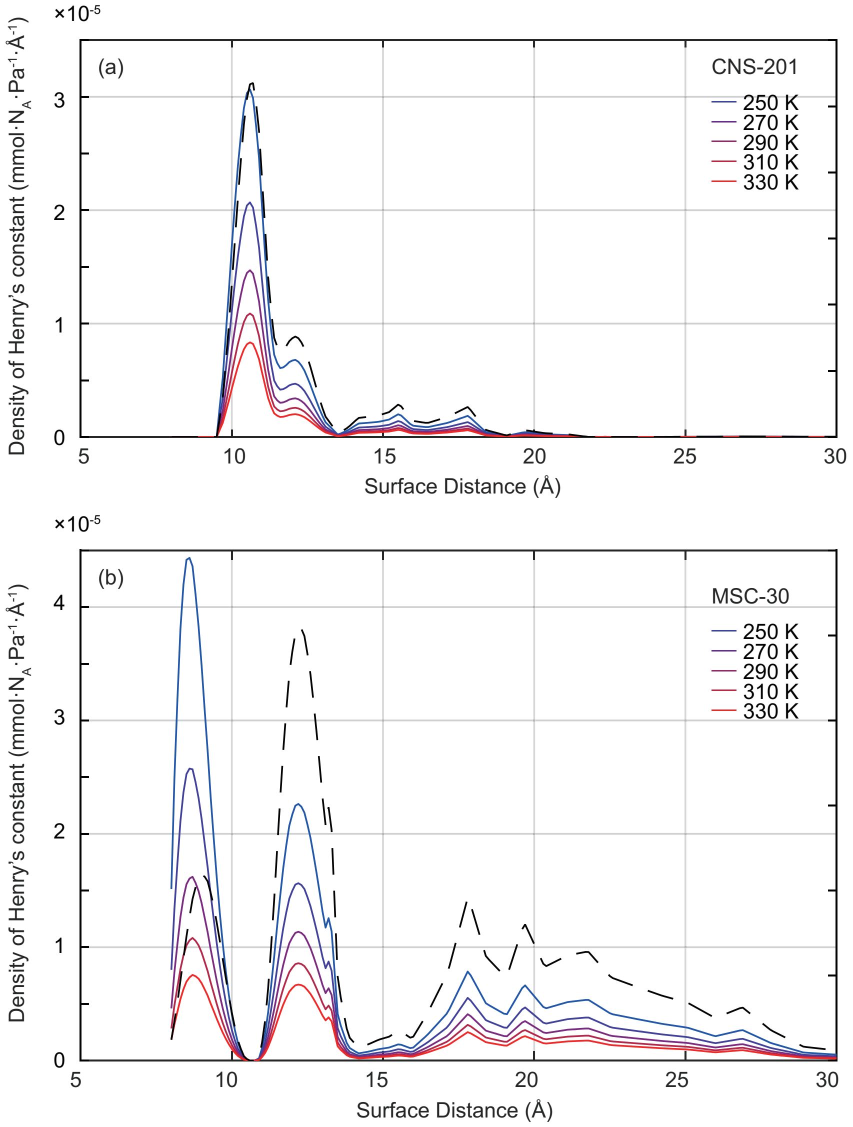

Figure 5.1: The density of Henry's constant at different temperatures, which is a continuous function form of the right part in Eq. (2.54). The black dash lines are the surface area distribution functions shown in Fig. (3.3a). (a) Results of CNS-201. (b) Results of MSC-30.

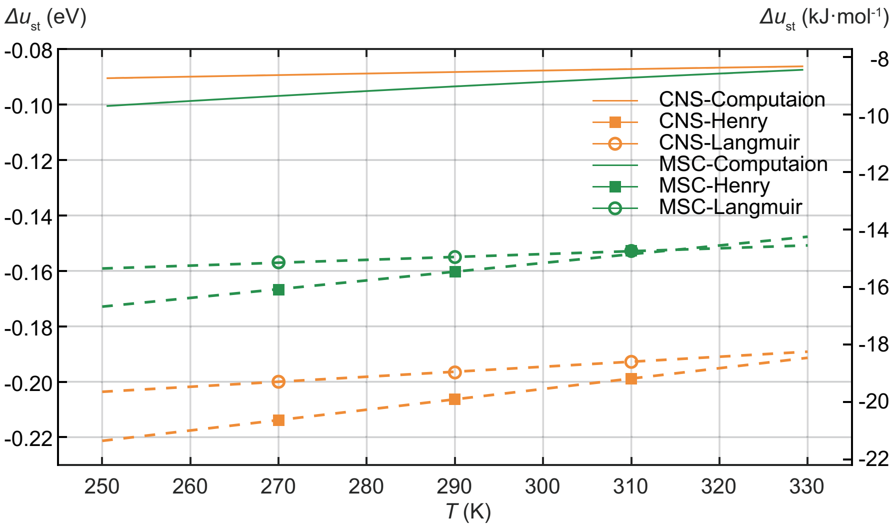

Figure 5.2: The solid lines are calculated isosteric adsorption energies of krypton on CNS-201 (orange) and MSC-30 (green). The dash lines are the experimental fits shown in Fig. (3.6) and (3.9) given by Henry's law and Langmuir model.

Table 5.1: The internal energies changing rate with temperature given by different methods.

	Henry's Law	Langmuir Model	2D Ideal Gas Model
CNS-201	$4.35k_B$	$2.10k_B$	$0.62k_B$
MSC-30	$3.65k_B$	$1.21k_B$	$2.03k_B$

The transfer of the gas from the lower energy peak to higher energy peaks also leads to an extra temperature dependence of the internal energies. For MSC-30, the transfer of the gas molecules has larger effects. Despite their lower total population, the energetically favorable sites smaller than 10.7 Å adsorb more gas than the sites around 12.2 Å. With increasing temperature, there is a decrease in the number of gas molecules in these energetically favorable sites, while pores with larger widths attract more gas. According to Fig. (4.8c), even the maximum adsorption energy changing rate can only reach $1.0k_B$ for a single pore width. But because of the gas transfer, MSC-30 can have a much larger slope of $2.03k_B$ in Fig. (5.2).

Considering the results in Fig. (4.14a), it is possible to infer that increasing temperature leads to a reduction in the favorability of the sites with lower energies, while the sites with higher energies become more accessible. A consequence of this phenomenon is that the overall average energy of the gas phase decreases in magnitude, leading to a decrease in the magnitude of the isosteric adsorption energy. This effect can be referred to as the "Boltzmann effect."

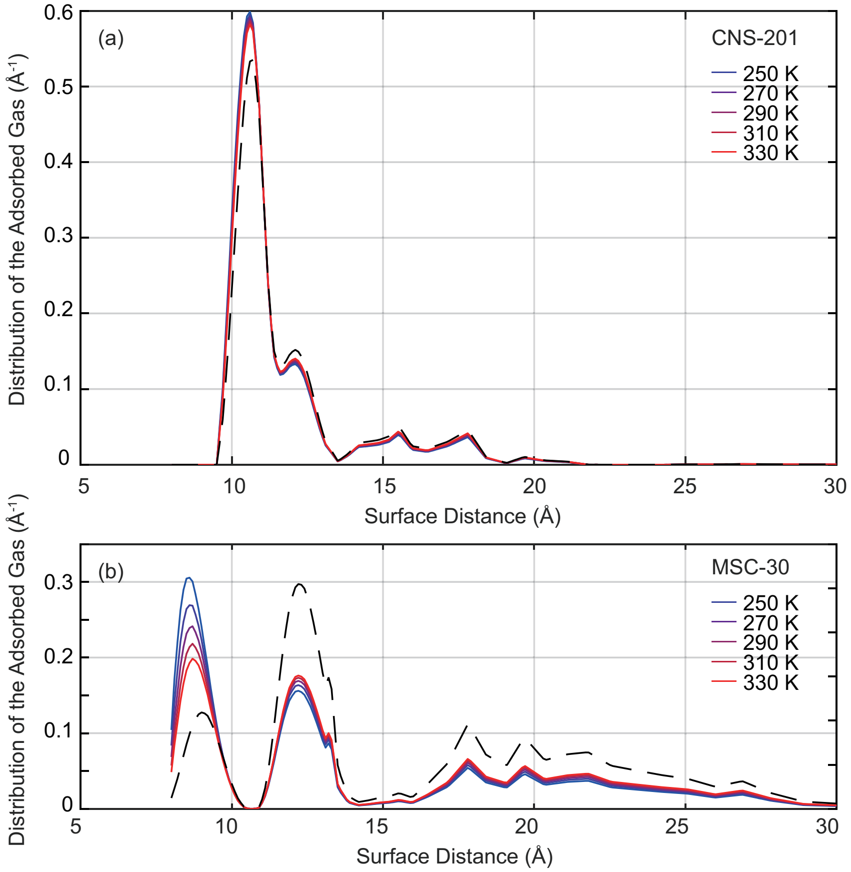

Figure 5.3: The distribution of the adsorbed gas, which corresponds to the n_i in Eq. (2.53) over the total adsorption amount n. These distributions can also be given by $n_i/n = K_{\mathrm{H},i}/K_{\mathrm{H}}$. The black dash lines are the surface area distribution functions shown in Fig. (3.3a).

For the i^{th} sites with $q_{\mathrm{ads},i}$, α_i, $q_{z,i}$ and $\varepsilon_{00,i}$ as given in the multi-site adsorption section, for a same number of adsorbate molecule n_0, the adsorbed phase Helmholtz free energy $F_{\mathrm{ads},i0}$, chemical potential, and internal energy $u_{\mathrm{ads},i0}$ of the i^{th} site are:

$$\begin{aligned} F_{\mathrm{ads},i0} &= -k_{\mathrm{B}}T \ln Q_{\mathrm{ads},i0} = -k_{\mathrm{B}}T \ln \frac{q_{\mathrm{ads},i}^{n_0}}{n_0!}, \\ &= n_0 k_{\mathrm{B}}T \ln n_0 - n_0 k_{\mathrm{B}}T \ln q_{z,i} - n_0 k_{\mathrm{B}}T \ln\left(\frac{\alpha_i A}{\Lambda^2}\right) + n_0\varepsilon_{00,i}; \end{aligned} \tag{5.1}$$

$$\mu_{\mathrm{ads},i0} = \left(\frac{\partial F_{\mathrm{ads},i}}{\partial n_0}\right)_T = k_{\mathrm{B}}T \ln n_0 - k_{\mathrm{B}}T \ln\left(\frac{\alpha_i A q_{z,i}}{\Lambda^2}\right) + \varepsilon_{00,i}; \tag{5.2}$$

$$u_{\mathrm{ads},i} = \frac{k_\mathrm{B}T^2}{n_i Q_{\mathrm{ads},i}} \frac{\partial Q_{\mathrm{ads},i}}{\partial T} = \varepsilon_{00,i} + \frac{k_\mathrm{B}T^2}{q_{z,i}} \frac{\partial q_{z,i}}{\partial T} + k_\mathrm{B}T. \tag{5.3}$$

Then the average adsorption energy is:

$$\begin{aligned} u_\mathrm{ads} &= \frac{\sum u_{\mathrm{ads},i} \exp(-\mu_{\mathrm{ads},i0}/k_\mathrm{B}T)}{\sum \exp(-\mu_{\mathrm{ads},i0}/k_\mathrm{B}T)} = \frac{\sum \alpha_i q_{z,i} \varepsilon_{00,i} \exp\left(-\varepsilon_{00,i}/k_\mathrm{B}T\right)}{\sum \alpha_i q_{z,i} \exp\left(-\varepsilon_{00,i}/k_\mathrm{B}T\right)} \\ &+ k_\mathrm{B}T^2 \frac{\sum \alpha_i \exp\left(-\varepsilon_{00,i}/k_\mathrm{B}T\right)\left(\partial q_{z,i}/\partial T\right)}{\sum \alpha_i q_{z,i} \exp\left(-\varepsilon_{00,i}/k_\mathrm{B}T\right)} + k_\mathrm{B}T, \end{aligned} \tag{5.4}$$

which is the same as Eq. (2.57).

To verify the impact of the non-ideal gas and multi-layers of carbon, the results in Fig. (4.14) and (4.15) are also used as a reference, and the results are shown in Fig. (5.4). For all three non-ideal models, the internal energy changes are almost the same, and therefore only one set of lines is used. The energies slightly increase for the non-ideal gas model, while for the 4 layers model, the energies decrease for less than 0.02 eV. For both the two different models, the slopes are almost identical to the 2 layer 2D ideal gas model. Therefore, the model with 2 surface layers is sufficient to study the temperature dependence of adsorption energy. However, more layers in bulk should be included to study the exact value of adsorption energy.

5.2 Other Possible Effects

In Fig. (5.2), all the computational energies are significantly smaller than the experimental result for both materials. The changes in internal energies in Table (5.1) also indicate that the computational results are lower than those with Henry's law, particularly for CNS-201. There are several possible reasons for these discrepancies.

First, the computational method ignores gas-gas interactions. The experimental zero-coverage adsorption energy is given by fitting the higher coverage data to zero-coverage, and higher coverage data contains the gas-gas interaction. The gas-gas interaction can be significant if the initial gas adsorption occurs in a process similar to the nucleation, where the other gas atoms also attract the newly adsorbed gas atoms. Then the gas-gas vdW potential can enhance the adsorption by the surface and provide more energy states for Boltzmann distribution. However, the LJ potential constant between krypton molecules $\varepsilon_{0,\mathrm{Kr}}$ is only 14.7 meV, which is about a half of the $k_\mathrm{B}T$ at room temperature (Maiga and Gatica, 2018). By taking the LJ potentials ranging from 3.0 Å to 16.0 Å into Boltzmann distribution, the averaged attraction

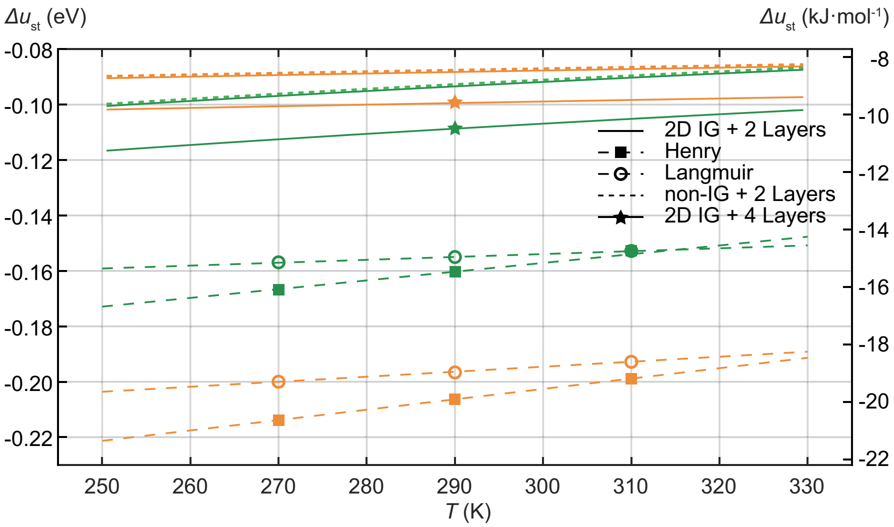

Figure 5.4: The dot lines above the solid lines are the isosteric adsorption energies for the non-ideal gas model. The solid lines with stars are the energies of 4 layers of carbon. Other reference results are from Fig. (5.2). "IG" means ideal gas in the figure legends.

potential between two krypton atoms is only 2.3 meV at 300 K. This number is much smaller than the krypton adsorption energies in the slit pores, and the formation of the 2D crystal is almost impossible. Therefore, the impact of gas-gas interaction is not critical at room temperature.

Second, the NLDFT method is limited in detecting energetically favorable pores smaller than 8.0 Å, as it mainly focuses on large pore detection at lower temperatures. However, by adding a small number of small pores to the two materials, the temperature dependence of adsorption energy can be different. The surface area distributions of added pores are shown in Fig. (5.5a) with dash lines. These distributions are Gaussian functions with standard deviations of 0.2 Å. The mean values of these two Gaussian functions are 7.3 Å for CNS-201 and 7.0 Å for MSC-30. The total added surface areas are both 100 m^2·g^{-1}, which is about 10.4% and 4.2% of the original NLDFT surface areas of CNS-201 and MSC-30. The adsorption energies of the new surface area distributions are shown in Fig. (5.5b). From 250 K to 330 K, the adsorption energies change from -0.147 eV to -0.120 eV for CNS-201 and from -0.120 eV to -0.098 eV for MSC-30. The slopes of these new fittings are 3.91k_{B} and 3.19k_{B}, which are close to Henry's law analysis in Table (5.1). Fig. (5.6) shows the gas distribution with the smaller size pores. Compared with the results in Fig. (5.3), these small pores are extremely favorable for the gas. Meanwhile, with increasing temperature, the gas molecules accumulated in these small pores transfer to larger pores.

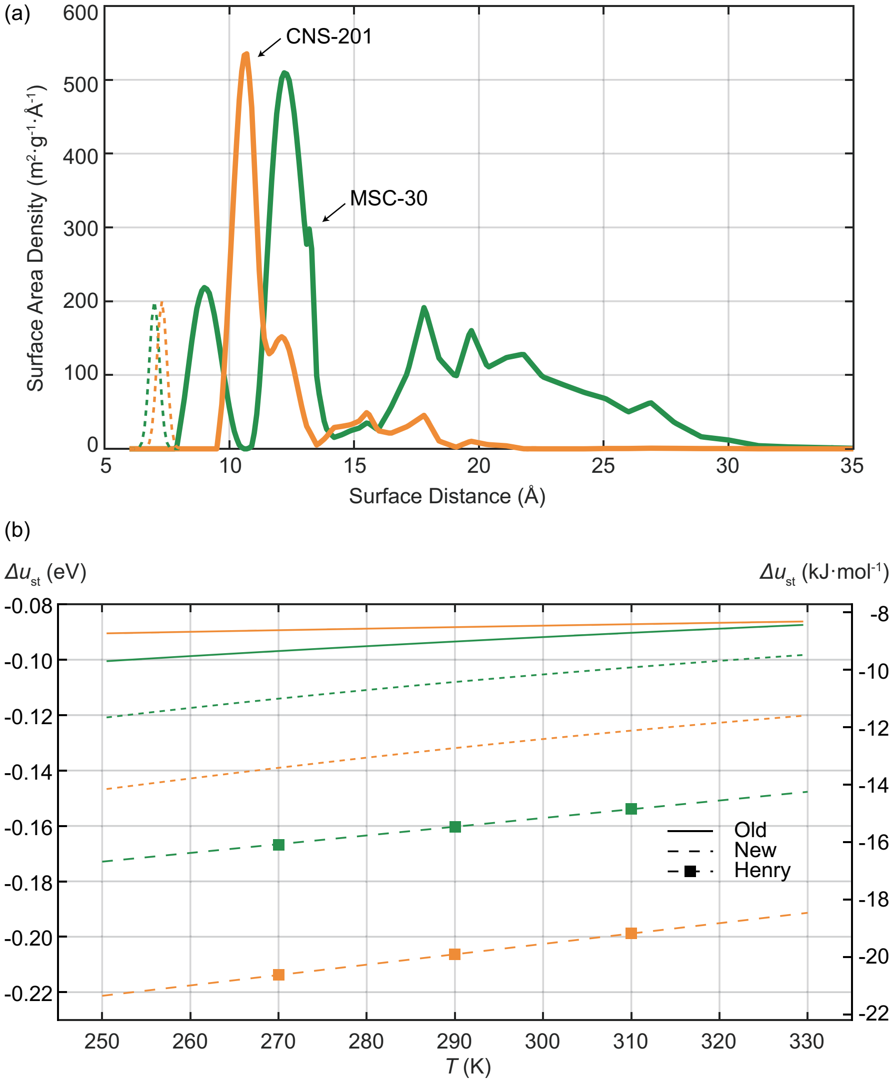

Figure 5.5: The impact of small-size pores on adsorption energies. (a) The dash lines are surface area distributions of added pores with small layer distances. The solid lines are the surface area distribution shown in Fig. (3.3). (b) Isosteric adsorption energies with the new modified surface area distribution are shown with the dash lines. Other results are the same as Fig. (5.2) as references.

Third, the slit-pore model does not consider the effects at the boundaries between pores of different sizes. Although different pores are at equilibrium, the process where gas molecules transfer between pores is ignored. If the slit pores are tilted at the boundary between the pores, the non-ideal surface dynamic can provide extra heat capacity in the $x - y$ directions.

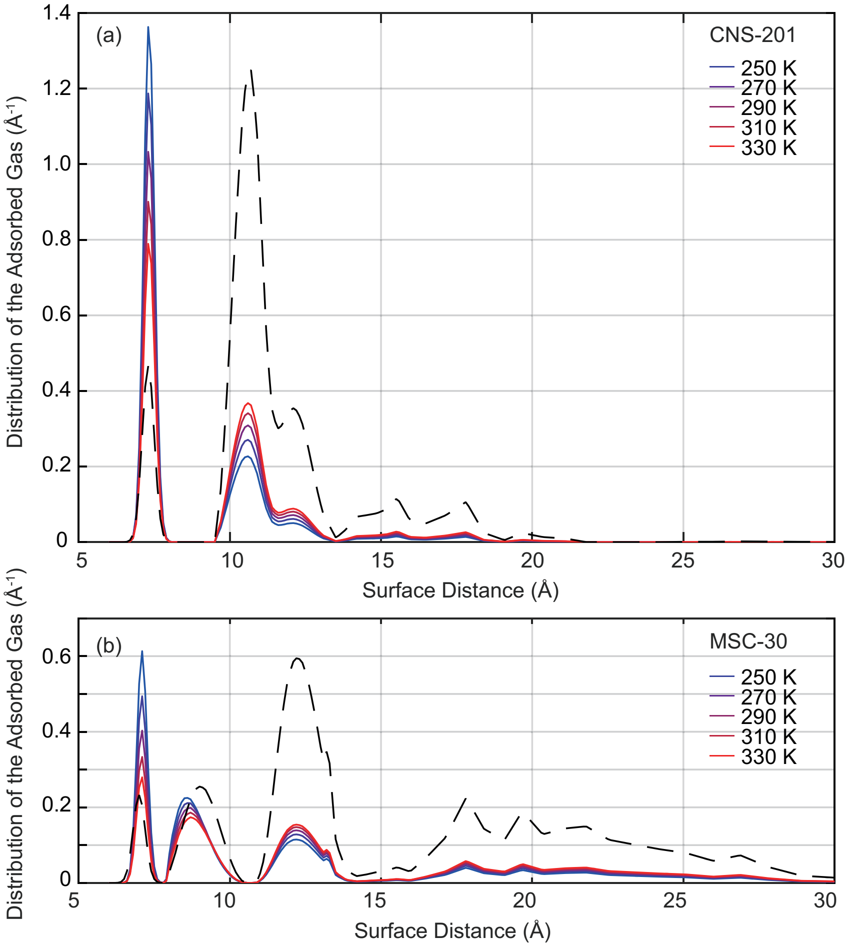

Figure 5.6: The distribution of the adsorbed gas with the new modified surface area distribution for (a) CNS-201 and (b) MSC-30. Similar to Fig. (5.3), the black dash lines are the surface area distribution functions shown in Fig. (5.5a) as reference.

Finally, active carbon materials are amorphous and contain elements other than carbon, such as oxygen and nitrogen, which can introduce extra errors to the adsorption energies.

5.3 Future Outlook

In the future, several potential projects could build upon this study. Current work can be expanded to investigate more adsorbate materials, especially materials with known crystal structures, including zeolite, MOF, zeolite-template carbons, etc. These structures would provide more accurate information on element types and pore and surface area distributions, enabling more precise calculations of the temperature dependence of adsorption energy. By comparing computational results with experimental data, the accuracy of the methods discussed in this work could be further verified. Meanwhile, different adsorbents, including carbon dioxide, methane, nitrogen, etc., can be studied. Compared with krypton, most of these gases are anisotropic. Therefore, their rotations and vibrations should also be considered apart from the translation. Further computational studies can reveal how the vdW potential hinders these degrees of freedom. For example, the carbon dioxide molecule, which has the shape of a rod, may prefer to be parallel to the surface for small layer distances and perpendicular to the surface for large layer distances. The changes in these internal degrees of freedom can lead to extra shifts in the temperature dependence of the adsorption energies.

Furthermore, based on the slit-pore results in this work, a new model for pore size measurement could be developed. The NLDFT method uses mean-field theory and is based only on one adsorption isotherm at one temperature. However, the model discussed in this thesis is based on multiple isotherms and more accurate DFT-calculated potentials. Meanwhile, the NLDFT method focuses on low temperatures and large pores. But this work analyzed smaller pores with high-temperature results. To develop the new model, several improvements could be made based on the possible effects discussed in the last subsection. For example, the gas-gas interactions are not negligible for more adsorption and lower temperatures. To add these interactions in the slit-pore model, methods including grand canonical Monte Carlo are possible choices (Maiga and Gatica, 2018).

Finally, an ambitious idea is to abandon the slit-pore model to measure pore size. Referring to the experimental and computational results in Fig. (5.2) and Fig. (4.15b), the largest ε_{00} of the slit-pore model is smaller than Δu_{st} of CNS-201. Also, according to the TEM figures, CNS-201 has pores with structures of tubes and spheres (M. R. Murialdo, 2017). Therefore, the slit-pore model is not the best choice to characterize CNS-201.

Going back to Eq. (2.29), with the single particle partition function, the single particle internal energy is:

$$\begin{aligned} u_{\mathrm{ads}} &= k_{\mathrm{B}} T^2 \cdot \frac{\partial \ln q_{\mathrm{ads}}}{\partial T}, \\ &= k_{\mathrm{B}} T^2 \cdot \left[\frac{\partial \iiint \exp\left(-\varepsilon_{\mathrm{vdW}}/k_{\mathrm{B}}T\right) \mathrm{d}x\mathrm{d}y\mathrm{d}z}{\partial T \cdot \iiint \exp\left(-\varepsilon_{\mathrm{vdW}}/k_{\mathrm{B}}T\right) \mathrm{d}x\mathrm{d}y\mathrm{d}z} - \frac{3}{\Lambda}\frac{\partial \Lambda}{\partial T} \right], \\ &= \frac{\iiint \varepsilon_{\mathrm{vdW}} \cdot \exp\left(-\varepsilon_{\mathrm{vdW}}/k_{\mathrm{B}}T\right) \mathrm{d}x\mathrm{d}y\mathrm{d}z}{\iiint \exp\left(-\varepsilon_{\mathrm{vdW}}/k_{\mathrm{B}}T\right) \mathrm{d}x\mathrm{d}y\mathrm{d}z} + 1.5 k_{\mathrm{B}} T, \end{aligned} \tag{5.5}$$

where the first term is the Boltzmann average of the vdW potential over the whole space. It can be rewritten as:

$$u_{\mathrm{ads}} = \frac{\int \varepsilon_{\mathrm{vdW}} \cdot f(\varepsilon_{\mathrm{vdW}}) \exp\left(-\varepsilon_{\mathrm{vdW}}/k_{\mathrm{B}}T\right) \mathrm{d}\varepsilon_{\mathrm{vdW}}}{\int f(\varepsilon_{\mathrm{vdW}}) \exp\left(-\varepsilon_{\mathrm{vdW}}/k_{\mathrm{B}}T\right) \mathrm{d}\varepsilon_{\mathrm{vdW}}} + 1.5k_{\mathrm{B}}T, \tag{5.6}$$

where $f(\varepsilon_{\mathrm{vdW}})$ is the distribution function of the vdW potential.

In Eq. (5.5), . Considering the ideal gas internal energy is $1.5k_{\mathrm{B}}T$, the adsorption energy is then the Boltzmann averaged vdW potential:

$$\begin{aligned}\Delta u_{\mathrm{st}} &= \frac{\iiint \varepsilon_{\mathrm{vdW}} \cdot \exp\left(-\varepsilon_{\mathrm{vdW}}/k_{\mathrm{B}}T\right) \mathrm{d}x\mathrm{d}y\mathrm{d}z}{\iiint \exp\left(-\varepsilon_{\mathrm{vdW}}/k_{\mathrm{B}}T\right) \mathrm{d}x\mathrm{d}y\mathrm{d}z}, \\ &= \frac{\int \varepsilon_{\mathrm{vdW}} \cdot f(\varepsilon_{\mathrm{vdW}}) \exp\left(-\varepsilon_{\mathrm{vdW}}/k_{\mathrm{B}}T\right) \mathrm{d}\varepsilon_{\mathrm{vdW}}}{\int f(\varepsilon_{\mathrm{vdW}}) \exp\left(-\varepsilon_{\mathrm{vdW}}/k_{\mathrm{B}}T\right) \mathrm{d}\varepsilon_{\mathrm{vdW}}}.\end{aligned} \tag{5.7}$$

While this Δu_{st} can be given from experiments at various temperatures, an intuitive ideal is finding the $f(\varepsilon_{\mathrm{vdW}})$. If $f(\varepsilon_{\mathrm{vdW}})$ is solved, the next step is to generate a periodic structure that fits this potential distribution. This was tried for MSC-30 in 2017 (Sarkisov, Centineo, and Brandani, 2017).

CONCLUSION

This thesis comprehensively investigated the temperature dependence of physical adsorption energy, combining theoretical, computational, and experimental approaches. A thermodynamic analysis of the 2D ideal gas and the slit-pore models highlighted the role of vdW potentials in the adsorption energy and isotherm fitting methods, including Henry's law and the Langmuir model. Experimental data of krypton adsorption on CNS-201 and MSC-30 porous carbon materials revealed a significant weakening in the isosteric adsorption energy with temperatures from 250 K to 330 K. By using the zero-coverage Henry's constants, the changing rates of adsorption energy per atom are $4.35\,k_\mathrm{B}$ for CNS-201 and $3.65\,k_\mathrm{B}$ for MSC-30. By including higher coverage results with the Langmuir model, the changing rates of adsorption energy per atom are $2.10\,k_\mathrm{B}$ for CNS-201 and $1.21\,k_\mathrm{B}$ for MSC-30.

The DFT-based computational study with the slit-pore model showed the vdW potentials of different-sized pores. Then it showed how the structures of the pores significantly influence the surface dynamics and the internal energies of the adsorbates at different temperatures. Gas molecules adsorbed in pores of different sizes have different heat capacities larger than the gas phase, leading to a temperature dependence of adsorption energy. Monte Carlo calculation indicated that displacements of adsorbent atoms caused by thermal vibration slightly weaken the vdW potentials, but have a negligible effect on the temperature dependence of the adsorption energy.

The distribution of pore sizes plays a crucial role in the temperature dependence of the overall adsorption energy. With increasing temperature, the pores with higher energy states become more accessible due to the Boltzmann distribution, weakening the statistically averaged internal energy. Adsorption energy changing rates of $0.62\,k_\mathrm{B}$ for CNS-201 and $2.03\,k_\mathrm{B}$ for MSC-30 are given by combining the computational vdW potentials and experimentally measured pore sizes.

Appendix A

ADSORBED PHASE PRESSURE AND VOLUME

Chapter 2 discussed the Clausius-Clapeyron equation Eq. (2.1), which assumes the pressure and temperature of the two phases are the same in equilibrium. In the 2D ideal gas model, the pressure in the z direction has no physical meaning, as D is a constant for a slit-pore. This pressure in the x and y directions is defined as the adsorbed phase pressure P_{ads}. However, according to the ideal gas equation:

$$P = \frac{nk_{\text{B}}T}{V} = \frac{k_{\text{B}}T}{v}, \tag{A.1}$$

the adsorbed phase pressure P_{ads} is larger than the gas phase pressure P_{gas} due to higher adsorbate molecule densities: $\rho_{\text{ads}} = 1/v_{\text{ads}}$.

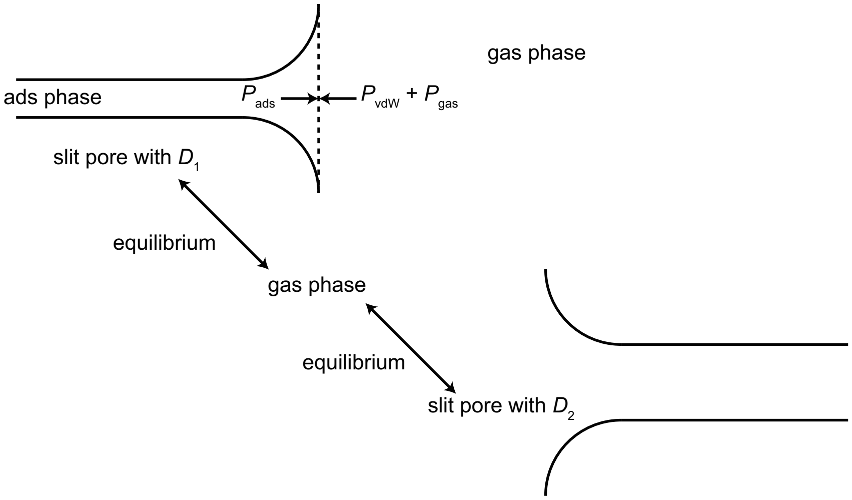

Figure A.1: Illustration of edge effects and pressure balance of the 2D ideal gas multi-site model. The slit pores with D_1 and D_2 are not directly connected but are both in equilibrium with the gas phase. The adsorbate molecules cannot directly transit between the pores, but go through an intermediate gas state.

The edge effect must be considered to maintain a pressure balance, illustrated in Fig. (A.1). For the plane shown with the dash line, the adsorbate molecules feel the adsorbed phase's pressure P_{ads} and the gas phase's pressure P_{gas}. As P_{ads} is larger than P_{gas} in the dilute, room temperature conditions, the net effect of these two pressures is pushing adsorbate molecules away from the adsorbed phase.

Meanwhile, at the edge of the slit-pore, adsorbate molecules also feel the $x - y$ direction vdW force. This force can become a pressure, attracting the adsorbate to the adsorbed phase. The three pressures in Fig. (A.1) balance and maintain the adsorption equilibrium.

In thermodynamics, the work done by the edge vdW force does not introduce new terms in the vdW potential. However, the $P_{\mathrm{ads}}V_{\mathrm{ads}}$ was ignored in most of the previous discussions. This approximation gives a simple and self-consistent theory, but the error led by this approximation also deserves discussion.

To include the PV energy, a rigorous expression of the chemical potential $\mu_{\mathrm{gas,G}}$ is acquired from the Gibbs energy. While in Chapter 2, the μ_{gas} is from the Helmholtz energy. The ideal gas chemical potential is:

$$\begin{aligned} \mu_{\mathrm{gas,G}} = \left(\frac{\partial G_{\mathrm{gas}}}{\partial n}\right)_T &= \left(\frac{\partial P_{\mathrm{gas}\cdot} \cdot V_{\mathrm{gas}}}{\partial n}\right)_T + \left(\frac{\partial F_{\mathrm{gas}}}{\partial n}\right)_T, \\ &= k_{\mathrm{B}}T + k_{\mathrm{B}}T \ln\left(\frac{P\Lambda^3}{k_{\mathrm{B}}T}\right), \end{aligned} \tag{A.2}$$

where G_{gas} is the Gibbs energy of the gas phase. This $\mu_{\mathrm{gas,G}}$ is a function of P and T. Meanwhile, the adsorbed phase chemical potential is:

$$\begin{aligned} \mu_{\mathrm{ads,G}} = \left(\frac{\partial G_{\mathrm{ads}}}{\partial n}\right)_T &= \left(\frac{\partial P_{\mathrm{ads}\cdot} \cdot V_{\mathrm{ads}}}{\partial n}\right)_T + \left(\frac{\partial F_{\mathrm{ads}}}{\partial n}\right)_T, \\ &= P_{\mathrm{ads}\cdot} \cdot v_{\mathrm{ads}} + \mu_{\mathrm{ads}}. \end{aligned} \tag{A.3}$$

Compared with the chemical potential acquired from Helmholtz energy μ_{ads}, the rigorous expression $\mu_{\mathrm{gas,G}}$ includes $P_{\mathrm{ads}\cdot} \cdot v_{\mathrm{ads}}$. For the 2D ideal gas, $P_{\mathrm{ads}\cdot} \cdot v_{\mathrm{ads}} = k_{\mathrm{B}}T$ is also applicable. Subsituting Eq. (2.50) into Eq. (A.3):

$$\mu_{\mathrm{ads,G}} = k_{\mathrm{B}}T + k_{\mathrm{B}}T \ln\left(\frac{n\Lambda^2}{Aq_z}\right) + \varepsilon_{00}. \tag{A.4}$$

In Eq. (A.4), the surface area A and the potential minimal ε_{00} are both constants. Then $\mu_{\mathrm{ads,G}}$ is a function of n and T. In the isosteric condition, n is a constant. Then $\mu_{\mathrm{ads,G}}$ is only a function of T. The P_{ads} can also be expressed by:

$$P_{\mathrm{ads}} = \frac{k_{\mathrm{B}}T}{v_{\mathrm{ads}}} = \frac{nk_{\mathrm{B}}T}{V_{\mathrm{ads}}} = \frac{nk_{\mathrm{B}}T}{AD}, \tag{A.5}$$

which is also a function of T.

In the isosteric condition, for the Clausius-Clapeyron equation, the Gibbs-Duhem equation turns from Eq. (2.4) into:

$$\begin{aligned} \mathrm{d}\mu_{\mathrm{gas,G}} &= -s_{\mathrm{gas}}\mathrm{d}T + v_{\mathrm{gas}}\mathrm{d}P_{\mathrm{gas}}\ ; \\ \mathrm{d}\mu_{\mathrm{ads,G}} &= -s_{\mathrm{ads}}\mathrm{d}T + v_{\mathrm{ads}}\mathrm{d}P_{\mathrm{ads}}\ . \end{aligned} \tag{A.6}$$

As mentioned, P_{ads} is a function of T, then Eq. (A.6) turns into:

$$\begin{aligned} \mathrm{d}\mu_{\text{gas,G}} &= -s_{\text{gas}}\mathrm{d}T + v_{\text{gas}}\mathrm{d}P_{\text{gas}} \ ; \\ \mathrm{d}\mu_{\text{ads,G}} &= -s_{\text{ads}}\mathrm{d}T + k_{\text{B}}\mathrm{d}T \ . \end{aligned} \tag{A.7}$$

Taking into Eq. (2.2), there is:

$$v_{\text{gas}}\mathrm{d}P_{\text{gas}} = (s_{\text{gas}} - s_{\text{ads}})\mathrm{d}T + k_{\text{B}}\mathrm{d}T, \tag{A.8}$$

According to Eq. (2.7), where the Gibbs energy is the same in equilibrium, the entropy turns into the enthalpy:

$$k_{\text{B}}T\frac{\mathrm{d}P_{\text{gas}}}{P_{\text{gas}}} = (h_{\text{gas}} - h_{\text{ads}} + k_{\text{B}}T)\frac{\mathrm{d}T}{T}, \tag{A.9}$$

Then the isosteric enthalpy is:

$$\Delta h_{\text{st}} = h_{\text{ads}} - h_{\text{gas}} = -\frac{k_{\text{B}}T^2}{P_{\text{gas}}}\left(\frac{\partial P_{\text{gas}}}{\partial T}\right)_n + k_{\text{B}}T. \tag{A.10}$$

Compared with Eq. (2.8), it is shown that the Clausius-Clapeyron equation is still applicable for the equilibrium between the 3D ideal gas phase and the 2D ideal gas adsorbed phase. However, the ignoring of v_{ads} leads to an error of $k_{\text{B}}T$ in the enthalpy, which is the ideal gas Pv energy. For the Δu_{st}, as h is now $u + k_{\text{B}}T$ for both phases,

$$\Delta u_{\text{st}} = \Delta h_{\text{st}} = -\frac{k_{\text{B}}T^2}{P_{\text{gas}}}\left(\frac{\partial P_{\text{gas}}}{\partial T}\right)_n + k_{\text{B}}T, \tag{A.11}$$

which is the same as Eq. (2.10). That shows that for the 2D ideal gas model, the Pv energy is still $k_{\text{B}}T$ and will not affect the isosteric adsorption energy.

For the other models, the models in Table (2.1) for example, the pressure and volume need definitions before applying the Clausius-Clapeyron equation. The isosteric condition can be used if the grand potential is used for the PV energy.

The approximation of ignoring the adsorbed phase volume also leads to errors in the excess adsorption n_{e} and absolute adsorption n_{a}. Their relationship is: $n_{\text{a}} = n_{\text{e}} + \rho_{\text{gas}} \cdot V_{\text{ads}}$, where ρ_{gas} is the gas phase molecule density. Absolute adsorption is used for theory, while experiments give excess adsorption.

If V_{ads} is not ignored, for the ideal gas, the molecule density is:

$$\rho_{\text{gas}} = P/k_{\text{B}}T, \tag{A.12}$$

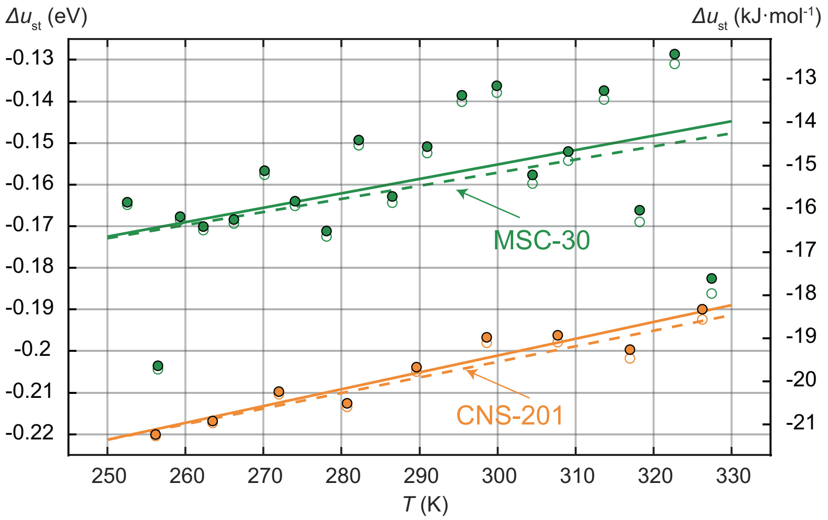

Figure A.2: Isosteric adsorption energies Δu_{st} at zero adsorption of krypton adsorption on CNS-201 (orange) and MSC-30 (green) given by Henry's law. The dash lines and unfilled circles are the results of excess adsorption. The solid lines and filled circles are the results of absolute adsorption.

then the relationship between excess and absolute adsorptions is:

$$n_{\mathrm{a}} = n_{\mathrm{e}} + PV_{\mathrm{ads}}/k_{\mathrm{B}}T. \tag{A.13}$$

The corresponding Henry's constants are:

$$K_{\mathrm{Ha}} = K_{\mathrm{He}} + V_{\mathrm{ads}}/k_{\mathrm{B}}T. \tag{A.14}$$

Using the NLDFT accumulated pore volumes for CNS-201 and MSC-30 and substituting Eq. (A.14) into Eq. (2.12), the adsorption energies are shown in Fig. (A.2). As the figure refers, the two results have no big difference.

Appendix B

FINITE LAYER APPROXIMATION

B.1 Comparison to Infinite Layers

In the future outlook section in Chapter 5, it is mentioned that: "the strongest ε_{00} of the slit-pore model is smaller than Δu_{st} of CNS-201." This was shown in Fig. (4.4). In Chapter 5, It was also checked that even with 4 layers on each side of the krypton atom, the strongest ε_{00} is still smaller Δu_{st}. This part will discuss 100 layers on each side to simulate infinite layers.

Assuming the vdW potential has an LJ form:

$$\varepsilon_{\text{LJ}}(R) = -4\varepsilon_0 \left[\left(\frac{\sigma}{R}\right)^{12} - \left(\frac{\sigma}{R}\right)^{6} \right], \tag{B.1}$$

then for an infinite surface with a homogeneous atom density ρ_{2D}, the total potential is:

$$\varepsilon(z) = -8\pi\varepsilon_0\rho_{\text{2D}} \left[\int_0^{+\infty} \frac{\sigma^{12} r \mathrm{d}r}{\left(r^2+z^2\right)^6} - \int_0^{+\infty} \frac{\sigma^{6} r \mathrm{d}r}{\left(r^2+z^2\right)^3} \right], \tag{B.2}$$

where z is the distance between the gas molecule and the surface, while r is the cylindrical coordinate radial distance. By calculating the integrals, Eq. (B.2) becomes:

$$\varepsilon_{\text{2D}}(z) = -4\pi\varepsilon_0\rho_{\text{2D}} \left(\frac{\sigma^{12}}{5z^{10}} - \frac{\sigma^6}{2z^4} \right). \tag{B.3}$$

For infinite number of layers with layer distance of D_{b}, the total potential is:

$$\begin{aligned} \varepsilon_{\text{tot,2D}}(z) = &- \frac{4\pi\varepsilon_0\rho_{\text{2D}}\sigma^{12}}{5} \left[\frac{1}{z^{10}} + \frac{1}{(z+D_{\text{b}})^{10}} + \frac{1}{(z+2D_{\text{b}})^{10}} + \dots \right] \\ &+ \frac{4\pi\varepsilon_0\rho_{\text{2D}}\sigma^{6}}{2} \left[\frac{1}{z^{4}} + \frac{1}{(z+D_{\text{b}})^{4}} + \frac{1}{(z+2D_{\text{b}})^{4}} + \dots \right]. \end{aligned} \tag{B.4}$$

For the krypton-graphite system we discussed, $D_{\text{b}} = 3.325\,\text{Å}$, $\rho_{\text{2D}} = 0.3816\,\text{Å}^{-2}$. The other constants are $\varepsilon_0 = -5.96\,\text{meV}$ and $\sigma = 3.5\,\text{Å}$, as mentioned in Chapter 4 (Maiga and Gatica, 2018).

The comparison of $\varepsilon_{\text{tot,2D}}$ with different number of layers considered is shown in Fig. (B.1). For the 1 layer case, the vdW potential is $\varepsilon_{2\text{D}}(z)$. The minimal energy locates at $z = \sigma = 3.5\,\text{Å}$, and the value is $6\pi\varepsilon_0\rho_{2\text{D}}\sigma^2/5 = -0.106\,\text{eV}$. The calculation of 2 layers and 100 layers is also shown. For these results, the minimal energies locate at 3.4800 Å and 3.4775 Å, and the values are $-0.118\,\text{eV}$ and $-0.122\,\text{eV}$. Typically, with the resolution of Fig. (B.1), the results of 4 layers up to 100 layers are almost identical.

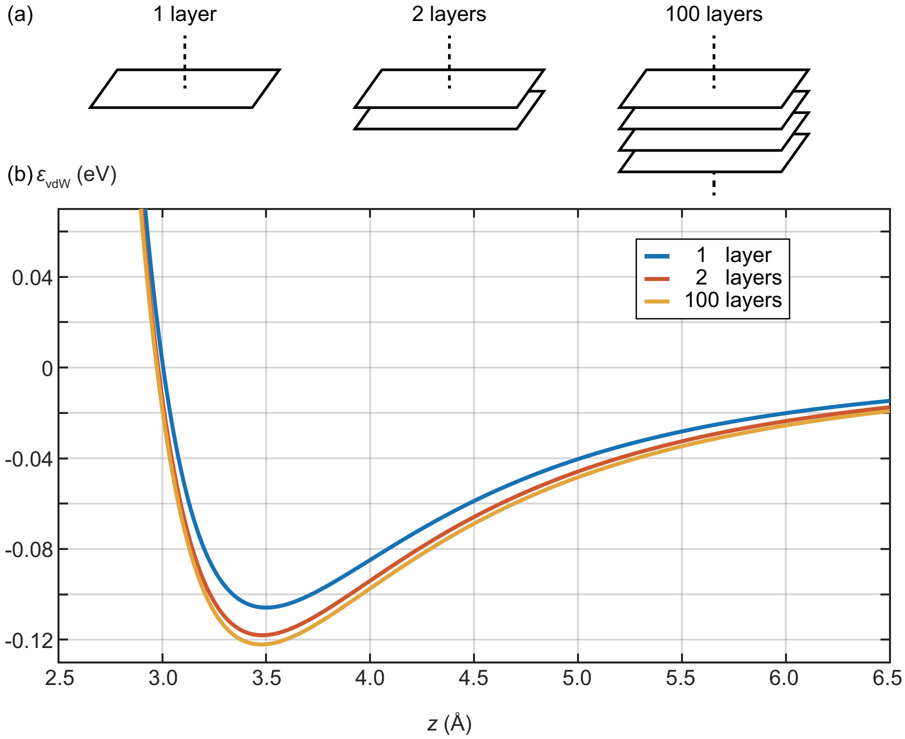

Figure B.1: The comparison of vdW potential with different numbers of layers considered. (a) The illustration of different configurations. The layers are assumed infinitely large. (b) The vdW potential of different configurations.

In Fig. (B.1), the first layer contributes the most vdW potential for the multi-layer configurations. The contributions from the other layers are much smaller. At the 3.5Å, the first layer, the first two layers, and the first four layers contribute 86.8%, 96.7%, and 99.4% of the potential. Therefore, it can be concluded that for the multi-layer configurations, having 2 layers on one side is already a good approximation. Having 4 layers on one side is almost the same as having infinite layers, as the further layers' contributions are negligible.

B.2 Comparison to Continuum Adsorbent

Meanwhile, the continuum approximation is another method of simulating the infinite-size adsorbent, as Fig. (B.2a) shows. The adsorbent atoms are evenly distributed in 3D, and the layers turn into a bulk material with an atom density of $\rho_{3D} = \rho_{2D}/D_b$. The total vdW potential is:

$$\varepsilon_{\text{tot,3D}}(z) = \int_z^\infty \frac{\rho_{3D}}{\rho_{2D}} \cdot \varepsilon_{2D}(z_0)\mathrm{d}z_0 = -4\pi\varepsilon_0\rho_{3D}\left(\frac{\sigma^{12}}{45z^9} - \frac{\sigma^6}{6z^3}\right). \tag{B.5}$$

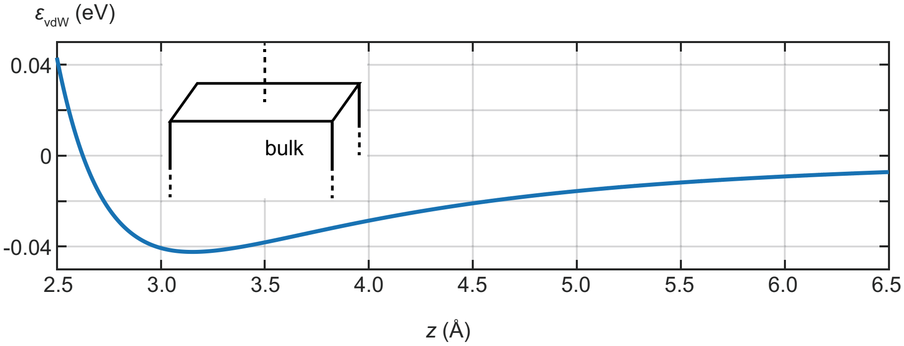

Figure B.2: The illustration and vdW potential of the continuum approximation. (a) The illustration of turning non-continuous into continuous bulk. (b) The vdW potential of the bulk adsorbent.

The vdW potential can be calculated with the constants used before, and the results are shown in Fig. (B.2b). The minimal energy locates at $z = 0.4^{-1/6}\sigma \approx 3.0050$ Å, and the value is $0.702\pi\varepsilon_0\rho_{3D}\sigma^3 = -0.065$ eV. Compared with Fig. (B.1), the bulk vdW potential significantly underestimated the magnitude of vdW potential.

For the continuum approximation, it is equivalent to decrease ρ_{2D} and D_b proportionally in Eq. (B.4). This will decrease the contribution from the first layer. As mentioned in the last section, the vdW potential comes mainly from the first layer. Therefore, the continuum approximation will lead to a weakening in the total vdW potential.

Compared with the experiment data, this continuum approximation potential is too weak. Therefore, using finite layer approximation is a better choice.

BIBLIOGRAPHY

Ambrosetti, Alberto et al. (May 2014). “Long-range correlation energy calculated from coupled atomic response functions”. In: *The Journal of Chemical Physics* 140 (18), 18A508. ISSN: 0021-9606. DOI: `10.1063/1.4865104`. URL: `http://aip.scitation.org/doi/10.1063/1.4865104`.

Campbell, Charles T. and Jason R. V. Sellers (2012). “The entropies of adsorbed molecules”. In: *Journal of the American Chemical Society* 134.43, pp. 18109–18115.

Campbell, Charles T., Lynza H. Sprowl, and Liney Arnadottir (2016). “Equilibrium constants and rate constants for adsorbates: Two-dimensional (2D) ideal gas, 2D ideal lattice gas, and ideal hindered translator models”. In: *The Journal of Physical Chemistry C* 120.19, pp. 10283–10297.

Chen, Xuesong et al. (1997). “Theoretical and experimental studies of methane adsorption on microporous carbons”. In: *Carbon* 35.9, pp. 1251–1258.

Echenique, Pablo and Jose Luis Alonso (2007). “A mathematical and computational review of Hartree–Fock SCF methods in quantum chemistry”. In: *Molecular Physics* 105.23-24, pp. 3057–3098.

Fang, Hanjun et al. (2012). “Prediction of CO 2 adsorption properties in zeolites using force fields derived from periodic dispersion-corrected DFT calculations”. In: *Journal of Physical Chemistry C* 116 (19), pp. 10692–10701. ISSN: 19327447. DOI: `10.1021/jp302433b`.

Farrusseng, David et al. (2009). “Heats of adsorption for seven gases in three metal - Organic frameworks: Systematic comparison of experiment and simulation”. In: *Langmuir* 25 (13), pp. 7383–7388. ISSN: 07437463. DOI: `10.1021/la900283t`.

Gilbert, Thomas L (1975). “Hohenberg-Kohn theorem for nonlocal external potentials”. In: *Physical Review B* 12.6, p. 2111.

Gould, Tim et al. (2016). “A fractionally ionic approach to polarizability and van der Waals many-body dispersion calculations”. In: *Journal of Chemical Theory and Computation* 12.12, pp. 5920–5930.

Grimme, Stefan (2006). “Semiempirical GGA-type density functional constructed with a long-range dispersion correction”. In: *Journal of Computational Chemistry* 27.15, pp. 1787–1799.

– (2011). “Density functional theory with London dispersion corrections”. In: *Wiley Interdisciplinary Reviews: Computational Molecular Science* 1 (2), pp. 211–228. ISSN: 17590876. DOI: `10.1002/wcms.30`.

Grimme, Stefan et al. (2010). “A consistent and accurate ab initio parametrization of density functional dispersion correction (DFT-D) for the 94 elements H-Pu”. In: *The Journal of chemical physics* 132.15, p. 154104.

Haber, Fritz and Robert Le Rossignol (1913). “Uber die technische Darstellung von Ammoniak aus den Elementen”. In: *Zeitschrift fur Elektrochemie und angewandte physikalische Chemie* 19.2, pp. 53–72.

Hartree, Douglas Rayner and William Hartree (1935). “Self-consistent field, with exchange, for beryllium”. In: *Proceedings of the Royal Society of London. Series A-Mathematical and Physical Sciences* 150.869, pp. 9–33.

Hellman, Olle and Igor A Abrikosov (Oct. 2013). “Temperature-dependent effective third-order interatomic force constants from first principles”. In: *Physical Review B* 88 (14), p. 144301. DOI: `10.1103/PhysRevB.88.144301`. URL: `https://link.aps.org/doi/10.1103/PhysRevB.88.144301`.

Hellman, Olle, Igor A Abrikosov, and Sergei I Simak (Nov. 2011). “Lattice dynamics of anharmonic solids from first principles”. In: *Phys. Rev. B* 84 (18), p. 180301. DOI: `10.1103/PhysRevB.84.180301`. URL: `https://link.aps.org/doi/10.1103/PhysRevB.84.180301`.

Hellman, Olle, Peter Steneteg, et al. (2013). “Temperature dependent effective potential method for accurate free energy calculations of solids”. In: *Physical Review B* 87.10, p. 104111.

Helmy, Ahmed K., Eladio A. Ferreiro, and Silvia G. de Bussetti (1996). “Energy, enthalpy, and isosteric heat of adsorption of phosphate on hydrous Al oxide”. In: *Journal of Colloid and Interface Science* 183 (1), pp. 131–134. ISSN: 00219797. DOI: `10.1006/jcis.1996.0526`.

Hill, Terrell L. (1994). *Thermodynamics of small systems*. Courier Corporation.

Hohenberg, Pierre and Walter Kohn (1964). “Inhomogeneous electron gas”. In: *Physical Review* 136.3B, B864.

Huang, Yun Yang (1972). “The temperature dependence of isosteric heat of adsorption on the heterogeneous surface”. In: *Journal of Catalysis* 25 (1), pp. 131–138. ISSN: 10902694. DOI: `10.1016/0021-9517(72)90210-2`.

Hyla, Alexander S. et al. (2019). “Significant temperature dependence of the isosteric heats of adsorption of gases in zeolites demonstrated by experiments and molecular simulations”. In: *Journal of Physical Chemistry C* 123 (33), pp. 20405–20412. ISSN: 19327455. DOI: `10.1021/acs.jpcc.9b05758`.

Jagiello, Jacek (Aug. 1994). “Stable numerical solution of the adsorption integral equation using splines”. In: *Langmuir* 10 (8), pp. 2778–2785. ISSN: 0743-7463. DOI: `10.1021/la00020a045`. URL: `https://pubs.acs.org/doi/abs/10.1021/la00020a045`.

Jagiello, Jacek and Jeffrey Kenvin (2019). “Consistency of carbon nanopore characteristics derived from adsorption of simple gases and 2D-NLDFT models. Advantages of using adsorption isotherms of oxygen (O2) at 77 K”. In: *Journal of colloid and interface science* 542, pp. 151–158.

Jorda-Beneyto, Maria et al. (2007). “Hydrogen storage on chemically activated carbons and carbon nanomaterials at high pressures”. In: *Carbon* 45.2, pp. 293–303.

Keesom, Willem Hendrik (1915). “The second viral coefficient for rigid spherical molecules, whose mutual attraction is equivalent to that of a quadruplet placed at their centre”. In: *Koninklijke Nederlandsche Akademie van Wetenschappen Proceedings* 18, pp. 636–646.

Kim, Won June et al. (2016). “Failure of density functional dispersion correction in metallic systems and its possible solution using a modified many-body dispersion correction”. In: *The Journal of Physical Chemistry Letters* 7.16, pp. 3278–3283.

Kittel, Charles (2004). *Introduction to Solid State Physics, 8th Edition*, pp. 53–60. ISBN: 978-0-471-41526-8.

Klimes, Jiri and Angelos Michaelides (2012). “Perspective: Advances and challenges in treating van der Waals dispersion forces in density functional theory”. In: *The Journal of chemical physics* 137.12, p. 120901.

Kohn, Walter and Lu Jeu Sham (1965). “Self-consistent equations including exchange and correlation effects”. In: *Physical review* 140.4A, A1133.

Kresse, Georg and Jurgen Furthmuller (1996a). “Efficiency of ab-initio total energy calculations for metals and semiconductors using a plane-wave basis set”. In: *Computational Materials Science* 6 (1), pp. 15–50. ISSN: 09270256. DOI: `10.1016/0927-0256(96)00008-0`.

– (1996b). “Efficient iterative schemes for ab initio total-energy calculations using a plane-wave basis set”. In: *Physical Review B - Condensed Matter and Materials Physics* 54 (16), pp. 11169–11186. ISSN: 1550235X. DOI: `10.1103/PhysRevB.54.11169`.

Kresse, Georg and Jurgen Hafner (1993). “Ab initio molecular dynamics for liquid metals”. In: *Physical Review B* 47 (1), pp. 558–561. ISSN: 01631829. DOI: `10.1103/PhysRevB.47.558`.

– (1994). “Norm-conserving and ultrasoft pseudopotentials for first-row and transition elements”. In: *Journal of Physics: Condensed Matter* 6 (40), pp. 8245–8257. ISSN: 09538984. DOI: `10.1088/0953-8984/6/40/015`.

Kresse, Georg and Daniel Joubert (Jan. 1999). “From ultrasoft pseudopotentials to the projector augmented-wave method”. In: *Physical Review B* 59 (3), pp. 1758–1775. ISSN: 0163-1829. DOI: `10.1103/PhysRevB.59.1758`. URL: `https://link.aps.org/doi/10.1103/PhysRevB.59.1758`.

Kupgan, Grit, Thilanga P. Liyana-Arachchi, and Coray M. Colina (2017). “NLDFT pore size distribution in amorphous microporous materials”. In: *Langmuir* 33.42, pp. 11138–11145.

Langmuir, Irving (1916). “The constitution and fundamental properties of solids and liquids. Part I. Solids.” In: *Journal of the American Chemical Society* 38.11, pp. 2221–2295.

Lastoskie, Christian, Keith E. Gubbins, and Nicholas Quirke (1993). “Pore size distribution analysis of microporous carbons: a density functional theory approach”. In: *The Journal of Physical Chemistry* 97.18, pp. 4786–4796.

Lefebvre, Dominique and F Handan Tezel (2017). “A review of energy storage technologies with a focus on adsorption thermal energy storage processes for heating applications”. In: *Renewable and Sustainable Energy Reviews* 67, pp. 116–125.

Leite, Fabio L et al. (2012). “Theoretical models for surface forces and adhesion and their measurement using atomic force microscopy”. In: *International Journal of Molecular Sciences* 13.10, pp. 12773–12856.

Lennard-Jones, John E. (1931). “Cohesion”. In: *Proceedings of the Physical Society* 43.5, p. 461.

London, Fritz (1937). “The general theory of molecular forces”. In: *Transactions of the Faraday Society* 33, 8b–26.

Maiga, Sidi M. and Silvina M. Gatica (2018). “Monolayer adsorption of noble gases on graphene”. In: *Chemical Physics* 501, pp. 46–52. ISSN: 03010104. DOI: `10.1016/j.chemphys.2017.11.020`. URL: `https://doi.org/10.1016/j.chemphys.2017.11.020`.

Maultzsch, Janina et al. (2004). “Phonon Dispersion in Graphite”. In: *Physical Review Letters* 92 (7), pp. 1–4. ISSN: 10797114. DOI: `10.1103/PhysRevLett.92.075501`.

Menon, Vinayan C. and Sridhar Komarneni (1998). “Porous adsorbents for vehicular natural gas storage: a review”. In: *Journal of Porous Materials* 5, pp. 43–58.

Mohr, Marcel et al. (2007). “Phonon dispersion of graphite by inelastic x-ray scattering”. In: *Physical Review B - Condensed Matter and Materials Physics* 76 (3), pp. 1–7. ISSN: 10980121. DOI: `10.1103/PhysRevB.76.035439`.

Murialdo, Maxwell et al. (2015). “Krypton Adsorption on Zeolite-Templated Carbon and Anomalous Surface Thermodynamics”. In: *Langmuir* 31 (29), pp. 7991–7998. ISSN: 15205827. DOI: `10.1021/acs.langmuir.5b01497`.

Murialdo, Maxwell Robert (2017). “Anomalous Thermodynamics of Nonideal Gas Physisorption on Nanostructured Carbons”. PhD thesis. California Institute of Technology.

Nicholson, David and Neville George Parsonage (1982). *Computer simulation and the statistical mechanics of adsorption*. Academic Press, p. 1. ISBN: 9780125180603.

Olivier, James P. (1995). “Modeling physical adsorption on porous and nonporous solids using density functional theory”. In: *Journal of porous materials* 2, pp. 9–17.

Olivier, James P. (Oct. 1998). “Improving the models used for calculating the size distribution of micropore volume of activated carbons from adsorption data”. In: *Carbon* 36 (10), pp. 1469–1472. ISSN: 00086223. DOI: `10.1016/S0008-6223(98)00139-0`. URL: `https://linkinghub.elsevier.com/retrieve/pii/S0008622398001390`.

Olney, Terry N. et al. (1997). “Absolute scale determination for photoabsorption spectra and the calculation of molecular properties using dipole sum-rules”. In: *Chemical Physics* 223.1, pp. 59–98.

Panella, Barbara, Michael Hirscher, and Siegmar Roth (2005). “Hydrogen adsorption in different carbon nanostructures”. In: *Carbon* 43.10, pp. 2209–2214.

Poirier, Eric, Richard Chahine, and Tapan K. Bose (2001). “Hydrogen adsorption in carbon nanostructures”. In: *International Journal of Hydrogen Energy* 26.8, pp. 831–835.

Rubes, Miroslav et al. (2018). “Temperature dependence of carbon monoxide adsorption on a high-silica H-FER zeolite”. In: *Journal of Physical Chemistry C* 122 (45), pp. 26088–26095. ISSN: 19327455. DOI: `10.1021/acs.jpcc.8b08935`.

Ruthven, Douglas M. (2006). “Fundamentals of adsorption equilibrium and kinetics in microporous solids”. In: *Adsorption and Diffusion*. Springer, pp. 1–43.

Sandler, Stanley I. (2017). *Chemical, biochemical, and engineering thermodynamics*. ISBN: 978-1-119-32128-6.

Sarkisov, Lev, Alessio Centineo, and Stefano Brandani (2017). “Molecular simulation and experiments of water adsorption in a high surface area activated carbon: Hysteresis, scanning curves and spatial organization of water clusters”. In: *Carbon* 118, pp. 127–138.

Shen, Dongmin et al. (2000). “Comparison of experimental techniques for measuring isosteric heat of adsorption”. In: *Adsorption* 6 (4), pp. 275–286. ISSN: 09295607. DOI: `10.1023/A:1026551213604`.

Sholl, David S. and Janice A. Steckel (2009). *Density functional theory: a practical introduction*. John Wiley & Sons, pp. 10–23.

Son, Karen N. et al. (2018). “Measurement and prediction of the heat of adsorption and equilibrium concentration of CO2 on zeolite 13X”. In: *Journal of Chemical and Engineering Data* 63 (5), pp. 1663–1674. ISSN: 15205134. DOI: `10.1021/acs.jced.8b00019`.

Sprowl, Lynza H., Charles T. Campbell, and Liney Arnadottir (2016). “Hindered translator and hindered rotor models for adsorbates: Partition functions and entropies”. In: *The Journal of Physical Chemistry C* 120.18, pp. 9719–9731.

Stadie, Nicholas (2013). “Synthesis and thermodynamic studies of physisorptive energy storage materials”. In: *Thesis* 2013, p. 193. URL: `http://thesis.library.caltech.edu/7198/`.

Stohr, Martin, Troy Van Voorhis, and Alexandre Tkatchenko (2019). “Theory and practice of modeling van der Waals interactions in electronic-structure calculations”. In: *Chemical Society Reviews* 48 (15), pp. 4118–4154. ISSN: 14604744. DOI: `10.1039/c9cs00060g`.

Swenson, Hans and Nicholas Stadie (2019). “Langmuir’s theory of adsorption: A centennial review”. In: *Langmuir* 35.16, pp. 5409–5426.

Tkatchenko, Alexandre, Robert A. Distasio, et al. (2012). “Accurate and efficient method for many-body van der Waals interactions”. In: *Physical Review Letters* 108 (23), pp. 1–5. ISSN: 00319007. DOI: `10.1103/PhysRevLett.108.236402`.

Tkatchenko, Alexandre and Matthias Scheffler (2009). “Accurate molecular van der Waals interactions from ground-state electron density and free-atom reference data”. In: *Physical Review Letters* 102.7, p. 073005.

Toth, Jozsef (2002). *Adsorption*. CRC Press, p. 1.

Wirtz, Ludger and Angel Rubio (2004). “The phonon dispersion of graphite revisited”. In: *Solid State Communications* 131 (3-4), pp. 141–152. ISSN: 00381098. DOI: `10.1016/j.ssc.2004.04.042`.

Yu, Xiaohan et al. (2021). “Efficient models for predicting temperature-dependent henry’s constants and adsorption selectivities for diverse collections of molecules in metal–organic frameworks”. In: *Journal of Physical Chemistry C* 125 (32), pp. 18046–18057. ISSN: 19327455. DOI: `10.1021/acs.jpcc.1c05266`.